Precise Measurement of the 7Be(p,gamma)8B S-factor

Erik C. Mohrmann

A dissertation submitted in partial fulfillment
of the requirements for the degree of

Doctor of Philosophy

University of Washington

2008

Program Authorized to Offer Degree: Physics

University of Washington
Graduate School

This is to certify that I have examined this copy of a doctoral dissertation by

Erik C. Mohrmann

and have found that it is complete and satisfactory in all respects,
and that any and all revisions required by the final
examining committee have been made.

Chair of the Supervisory Committee:

_____

Kurt A. Snover

Reading Committee:

_____

Kurt A. Snover

_____

Gerald Miller

_____

R.G. Hamish Robertson

Date: _____

In presenting this dissertation in partial fulfillment of the requirements for the doctoral degree at the University of Washington, I agree that the Library shall make its copies freely available for inspection. I further agree that extensive copying of this dissertation is allowable only for scholarly purposes, consistent with "fair use" as prescribed in the U.S. Copyright Law. Requests for copying or reproduction of this dissertation may be referred to Proquest Information and Learning, 300 North Zeeb Road, Ann Arbor, MI 48106-1346, 1-800-521-0600, to whom the author has granted "the right to reproduce and sell (a) copies of the manuscript in microform and/or (b) printed copies of the manuscript made from microform."

Signature_____

Date_____

University of Washington

Abstract

Precise Measurement of the 7Be(p,gamma)8B S-factor

Erik C. Mohrmann

Chair of the Supervisory Committee:
Professor Kurt A. Snover
Physics

A presentation of a precision measurement of the ^{7}Be(p,γ)^{8}B cross section from $\bar{E}_{\mathrm{c.m.}}$ = 116 to 2460 keV. This measurement leads to $S_{17}(0) = 22.1 \pm 0.6(\mathrm{expt}) \pm 0.6(\mathrm{theor})$ eV b based on data from $\bar{E}_{\mathrm{c.m.}}$ = 116 to 362 keV, where the central value is based on the cluster model theory of Descouvemont. The theoretical error estimate is based on the fit of 12 different theories to our low energy data. We compare our results to other $S_{17}(0)$ values extracted from both direct (^{7}Be(p,γ)^{8}B) and indirect (Coulomb dissociation and heavy-ion reaction) measurements. We recommend a "best" value, $S_{17}(0) = 21.4 \pm 0.5(\mathrm{expt}) \pm 0.6(\mathrm{theor})$ eV b, based on the mean of all modern direct measurements below the 1^{+} resonance.

TABLE OF CONTENTS

LIST OF FIGURES

LIST OF TABLES

ACKNOWLEDGEMENTS

As with any work of this magnitude, this dissertation and the related research would not have been possible without support by a vast number of people. First and foremost are Arnd Junghans and Kurt Snover, whose guidance and carefulness were much appreciated and with whom I survived in a nine week (over 1500 hours!) marathon accelerator run. Thanks to Patrick Peplowski, Jean Marc Casandjian, Tom Steiger, and all those at TRIUMF for being excellent collaborators.

Thanks goes out to everyone else at CENPA who lended aid time and again, whenever asked and sometimes without the need. To Greg Harper, Doug Will, John Amsbaugh, Dick Seymour, Tim Van Wechel and Allen Meyers. To Jim Elms, Hank Simons, and David Hyde – you all were a dream to have watching my back. I remember more of what you did for me than you might suspect.

To Eric Swanson and Eric Adelberger, thank you for being on call for our think tank sessions and offering support. To the accelerator crews with whom I shared many a night shift, and to everyone else at CENPA who made the lab what it was.

Also to those whose assistance wasn't directly related to the experiment, but was no less important. To Pieter Mumm, Charles Duba, and Zack Hubert for pressuring me when I needed pressure and helping me relieve it when that was what I needed.

And of course, to my parents, who did a better job as parents than they'll admit, and for whom I'm endlessly thankful.

In memory of Erik Leder.

Chapter 1
INTRODUCTION

1.1 General Motivation

Our understanding of stars is dependent upon numerical models with a large number of input parameters. Because we have significantly more data about the sun, solar models are the indicator for how well we understand stellar structure and processes. As the models improve they allow comparison with precision observations, such as spectroscopic measurements, neutrino fluxes, and helioseismological modes.

Neutrino studies of the sun have yielded important information about neutrino physics and about the sun itself. The solar neutrino problem caused significant renewed interest in precision solar modeling, leading to new work in many fields including magneto-hydrodynamics, chemical opacities in stellar environments, and nuclear physics cross sections.

The work of Asplund et. al.[8] reported lower than expected abundances of heavy elements in the sun than previously believed. Their spectroscopic measurement of chemical abundances gives a view of the sun that is in conflict with current solar models. Current solar models match helioseismic data to incredible precision, leaving the measurements of these different properties in conflict.

In regard to these applications a precision measurement of the ^{7}Be(p,γ)^{8}B reaction is of renewed interest.

1.1.1 The Solar Neutrino Problem

The existence of the neutrino was first posited in 1930 by Wolfgang Pauli in order to explain the continuous energy spectrum seen in beta decays. Because neutrinos interact with matter only through the weak interactions the observation of neutrinos would wait many years until the development of an intense source of neutrinos, the nuclear reactor.

In the 1940s and fifties laboratory measurements of nuclear reaction rates led to the inference that the sun produced energy via the PP chain instead of the CNO cycle as Hans Bethe had first proposed. It was believed that essentially all of the neutrinos coming from the sun were products of the $p + p \longrightarrow {}^2H + e^+ + \nu_e$ reaction.

In 1958 Holmgren and Johnston reported the first measurement of $^3He(\alpha,\gamma)^7Be$ [38]. To the surprise of the physics community, this cross-section was a thousand times larger than had been expected. The ramifications of this moved through the physics and astrophysics communities very quickly. The higher cross-section for $^3He(\alpha,\gamma)^7Be$ meant there might be an appreciable amount of ^7Be in the sun, which might in turn undergo proton capture to make ^8B. It was important to know the reaction rate of $^7Be(p,\gamma)^8B$ since the ^7Be is not stable, and decays via electron capture to ^7Li. At this time it was already known that ^8B would undergo positron decay, giving off a high energy neutrino which might be seen in a detector on Earth.

With this news Ray Davis Jr. and his collaborators moved forward with plans to make a large detector containing ^{37}Cl [18], while at the same time Ralph W. Kavanagh was beginning the first measurement of $^7Be(p,\gamma)^8B$, reporting his first result in 1960 [43]. In 1964, and with more precision in 1968, the now famous Homestake solar neutrino experiment of Ray Davis Jr. observed fewer neutrinos than were expected by a factor of two [18, 19].

With this discrepancy it was important to improve the measurements, models,

and experiments involved in predicting and measuring the flux of neutrinos from the sun, including the ^{7}Be(p,γ)^{8}B reaction.

1.2 S-factors and Cross sections

The cross section is the fundamental physics measure of the probability of a particular subatomic reaction. The actual measured reaction yield is a function of the cross-section and environmental details such as the number of incident particles in the beam, the number of particles in the target, and the solid angle of the detector (see Section 3.1).

Using the cross section to discuss reactions at astrophysical energies can be inconvenient for several reasons. Cross-sections tend to be small, and change rapidly with energy because the relevant energies are below the Coulomb barriers of the nuclei involved. Dividing the cross section by the Coulomb repulsion between two nuclei creates a representation called the S-factor. This removes the energy dependence of the cross section, neglecting resonances and constributions from states with non-zero angular momentum. These exceptions make the S-factor the most useful at low energies.

In mathematical terms the S-factor is defined as:

$$S(E_{\text{c.m.}}) = \sigma(E_{\text{c.m.}})E_{\text{c.m.}}e^{(E_G/E_{\text{c.m.}})^{1/2}}. \tag{1.1}$$

For the ^{7}Be(p,γ)^{8}B reaction the Gamow energy $E_G = (2\pi\alpha Z_1 Z_2)^2\mu c^2/2 = 13799.3$ keV, where α is the fine structure constant, c is the speed of light, Z_1 and Z_2 are the charges of the two nuclei involved, and μ is the reduced mass.

1.3 The ^{7}Be system

^{7}Be is unstable and decays to ^{7}Li by electron capture. The terrestrial half-life for this decay is $t_{1/2} = 53.12 \pm 0.07$ days [15]. This decay proceeds to the ground state of ^{7}Li the majority of the time, but has a branching ratio, BR, of $10.52 \pm 0.06\%$ to the 478 keV excited state of ^{7}Li which then immediately relaxes to the ground state by emitting a 478 keV γ-ray [15].

The ^{7}Be(p,γ)^{8}B reaction has a Q value of 0.138 MeV. The unstable ground state of ^{8}B decays via emission of a positron and a neutrino to the broad 3 MeV first excited state of ^{8}Be with a $t_{1/2} = 770$ ms, and an endpoint energy of 14 MeV. That excited state then immediately breaks apart into two α particles. The large, 14 MeV endpoint, energy of this decay is what makes the emitted neutrino of special interest to neutrino physics.

1.4 History of ^{7}Be(p,γ)^{8}B measurements

Kavanagh did not try to measure the low energy prompt γ-rays from the proton capture because they would be obscured by the natural radioactivity from the ^{7}Be target. Since the reaction product, ^{8}B, is also radioactive it is possible to look for its delayed decay products as it decays to the wide first excited state of ^{8}Be.

In Kavanagh's first experiment he detected the decay positrons in a plastic scintillator and made a relative cross-section measurement at proton energies of 800 and 1400 keV. He then determined the absolute cross section by normalizing to the ^{7}Li(d,p)^{8}B cross section, measured with a separate thin target to be 176 ± 15 mb [43] at the peak of the 770 keV resonance. The level structure of ^{8}B's mirror nucleus, ^{8}Li, indicated that ^{8}B should have one excited state which would contribute to the cross section measurements Kavanagh made in the 1 MeV vicinity. Using his measurement and an estimation of this unmeasured M1 resonance, Kavanagh reported S_{17}(25 eV)

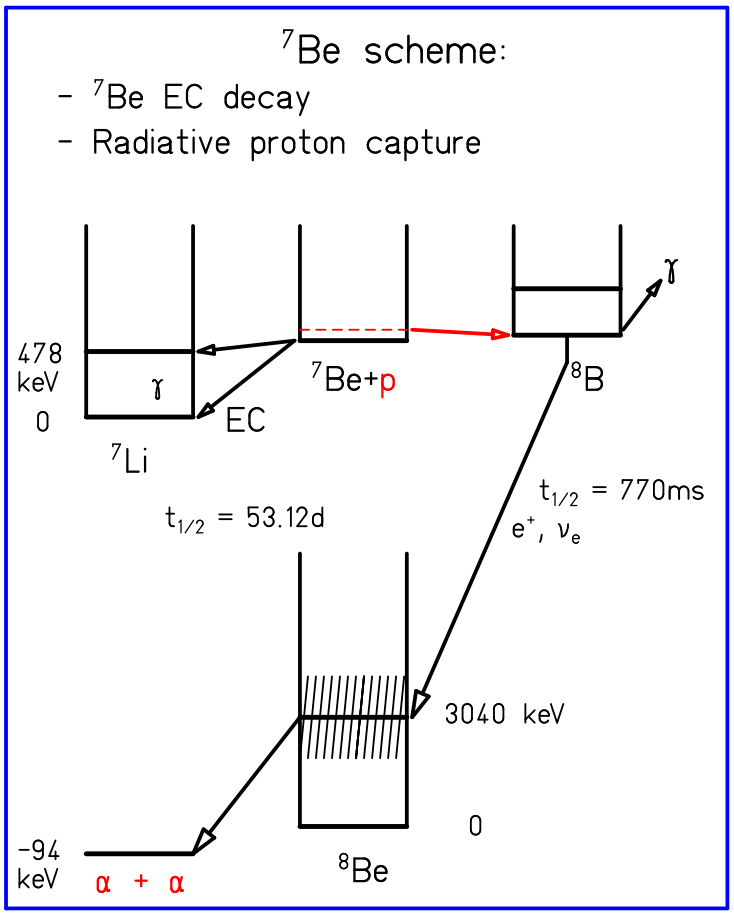

Figure 1.1: The level diagram and decay schemes for the ^{7}Be + p system. The red dashed line indicates the Q-value of the ^{7}Be(p,γ)^{8}B reaction [1]

= 20 ± 20 eV barn.

With the surprising results of the Homestake experiment the ^{7}Be(p,γ)^{8}B reaction rate came under renewed scrutiny and interest. The second measurement of ^{7}Be(p,γ)^{8}B was made by Peter D. Parker in 1966 [51], with several differences from Kavanagh's technique.

Parker placed the target on the end of a flipping arm, irradiated the ^{7}Be target and then, taking advantage of the 770 ms half-life of ^{8}B, moved the target in front of a thin silicon detector and detected the alpha particles from the β-delayed break up of the ^{8}Be. This technique removed the target from the vicinity of the accelerator beam, eliminating background from scattered beam that would overwhelm the low rate of alpha particles in the Si-detector.

Measuring at eight different proton energies, between 483 and 1932 keV, Parker measured the M1 resonance near 630 keV for the first time as well as determining $S_{17}(0)$, for which he reported 43 ± 4 eV b. Once again, this measurement was a relative measurement, normalized to the ^{7}Li(d,p)^{8}B cross-section, for which Parker measured 211 ± 15 mb, 20% higher than Kavanagh's value.

The disagreement between the values of Parker and Kavanagh was alarming enough that further measurements were required. In this light Parker reanalyzed his data [52] with an improved value for the ^{7}Li(d,p)^{8}B cross section obtained by averaging his measurement with Kavanagh's and adjusted his value of $S_{17}(0)$ downward to 35 ± 4 eV b. Even with this adjustment the mean experimental values for $S_{17}(0)$ were disparate.

Vaughn et. al. [64] measured the ^{7}B(p,γ)^{8}B reaction using a similar technique to Parker, but implemented beam rastering by passing the beam between parallel plates with triangular-shaped voltage waveforms on them. This swept the beam spot across the target, reducing the uncertainties due to nonuniformity of the ^{7}Be density over

Table 1.1: $S_{17}(0)$ values as analyzed by Vaughn [64]. Errors are relative and do not include uncertainty in the ^{7}Li(d,p)^{8}B cross section or in the theoretical extrapolation to zero energy.

Experiment:	Kavanagh	Parker	Vaughn
$S_{17}(0)$ [ev b]	22.2 ± 6.3	34.8 ± 6.3	26.3 ± 1.2

the target spot. The measurement was made at twenty proton energies from 0.953 to 3.281 keV. They utilized the average of Parker and Kavanagh's ^{7}Li(d,p)^{8}B cross sections in the same way as Parker's reanalysis [52]. Reanalyzing the work of Parker and Kavanagh, Vaughn et. al. found that the three experiments, when analyzed under the same method, using the same ^{7}Li(d,p)^{8}B cross section, and fit with the theoretical curve of Tombrello [62], gives an $S_{17}(0) = 29.6 \pm 4.0$ eV barns.

Vaughn et. al. also performed an analysis of their data which they believed to be physically motivated and more accurate, but which made the analysis incompatible with the earlier results of Kavanagh and Parker. They added an s-wave resonance above the 3^+ state, motivated by their own measurements and those of Kavanagh et. al. [44]. This analysis yielded $S_{17}(0) = 22.6 \pm 4.3$ eV b, where this error includes the uncertainty in the ^{7}Li(d,p)^{8}B cross section.

1.5 Modern Experiments

The status of the experimental determination of $S_{17}(0)$ remained unchanged until improvements in solar models and neutrino experiments necessitated a more accurate measurement.

The first of the "modern" experiments was that of Filippone et al. [26, 27], published in 1983. Filippone's effort included several innovations that increased the

overall precision of the experiment. Filippone's experiment made use of a large area detector mounted very close to the target so that it subtended a very large solid angle. The high detection efficiency of this set up allowed measurements at lower absolute event rates, and therefore lower bombardment energies, closer to the low energies at which the reaction takes in the sun. Mounting the detector close to the ^{7}Be target required the use of a thin detector so that the 478 keV γ rays from the radioactive target would not overwhelm the detector with Compton electrons. The vacuum system used oil free pumps, and employed cold traps to cause volatiles to plate out on surfaces other than the ^{7}Be target. This limited proton energy loss during bombardment to $\leq$ 3 keV, to allow a more accurate determination of the reaction energy.

Filippone determined $S_{17}(0)$ using two methods, one of which depended on the ^{7}Li(d,p)^{8}B cross section and one which did not, using target activity measurements to determine the amount of ^{7}Be present. When the average of two recent measurements of the ^{7}Li(d,p)^{8}B cross section [22, 28] was used the two methods agreed closely, giving 22.1 $\pm$ 2.8 eV barns (^{7}Li(d,p)^{8}B normalization) and 20.6 $\pm$ 3.0 eV barns (^{7}Be activity normalization)[26]. Filippone also used a least squares fit to Tombrello's model to allow comparison with previous experiments. This yielded $S_{17}(0)$ = 21.7 $\pm$ 2.5 eV barns[27].

Filippone also reanalyzed the data of previous experiments by renormalizing to his working value of 157$\pm$10 mb for the ^{7}Li(d,p)^{8}B cross section. This value was an average of the cross sections available at the time, with slight alteration. Filippone excluded the values of Parker[51] because they were nearly three standard deviations away from the other data. He also doubled the error bars on Schilling et. al.[55] claiming that they were unphysically small (see Fig 6 of [28]).

For a summary of this reanalysis see Table I of reference [26], and Figure 9 of

reference [27]. This analysis gave a recommended $S_{17}(0) = 23.8 \pm 2.3$ eV barns. At the end of [27] Filippone argues that continued studies of nuclear reactions are needed to help with the resolution of the solar neutrino problem.

This measurement was followed by many direct measurements, including this work, as well as indirect measurements, which tried to determine the S-factor by measuring other reactions and using physical symmetries to calculate $S_{17}(0)$. These are discussed further in Sections 5.3 and 5.4, respectively.

1.5.1 Current State of the Field

It should be noted that as the experimental determination of the ^{7}Be(p,γ)^{8}B reaction rate was being improved the solar neutrino field was also progressing. Detectors sensitive to mostly or exclusively ^{8}B neutrinos such as Kamiokande, Super-Kamiokande, and the Sudbury Neutrino Observatory, as well as complementary experiments such as Kamland, SAGE, GALLEX, and others, have refined the understanding of the sun's solar neutrino spectrum to the point where measurements of ^{7}Be(p,γ)^{8}B fulfill a different role now than when they were first begun in 1960.

The large number of data points and differing energy thresholds of the many solar neutrino experiments allow fits to neutrino data, alone, that constrain many of the parameters relevant to the solar neutrino problem. With publications by Super-Kamiokande [29] and SNO [3] neutrino oscillations are now the accepted explanation for the solar neutrino problem. The nature of the solar neutrino problem has been solved, but the details are still open for exploration. Precision measurements of $S_{17}(0)$ can constrain solar model parameters, and aid in the search or elimination of sterile neutrinos. It is in this endeavor that precision measurements of the ^{7}Be(p,γ)^{8}B astrophysical S-factor remain relevant to the solar neutrino problem.

Precision nuclear physics cross sections are also important in removing uncer-

tainties in solar models in the continued attempt to rectify the discrepancy between solar models which correctly predict spectroscopic observables using the current best known opacities and chemical abundances, and models which reproduce helioseismology data.

Chapter 2
EXPERIMENTAL APPARATUS

Precision measurement depends critically upon the experimental apparatus, including the target, accelerator, target chamber, and electronics. Each of these features is described in detail below.

2.1 Target Fabrication

An intensive effort to design and test ^{7}Be targets was carried out to minimize many uncertainties [68, 67]. Targets were fabricated on a backing of as low-Z material as the distillation chemistry would allow, and every effort was made to make targets of high ^{7}Be purity that constrained the target material to an area of small diameter.

The ^{7}Be target material was made at the TR13 cyclotron at TRIUMF. A Li metal target was bombarded by 13 MeV protons to create ^{7}Be via the ^{7}Li(p,n)^{7}Be reaction. The target was allowed to "cool" for a few days while short lived isotopes produced in the irradiation decayed. Even so, the targets remained hot. The three targets which we used to make data measurements, labeled BE1, BE2 and BE3, in chronological order, were made from activations of 220, 420, and 630 mCi of ^{7}Be, respectively.

When ready for removal the Li target was taken out and dissolved in ultra-pure water where it flowed into a porous glass filter. After letting stand overnight the entire apparatus was washed thoroughly with water. Since ^{7}Be adsorbs onto glass it remained in the filter to be removed by HCl. It was then dried and converted into BeO.

The ^{7}Be was made into a metallic target using a combination reduction-evaporation

and a vacuum-distillation. In the first step the BeO was heated in a Zr foil lined crucible. The Zr reduced the ^{7}Be, leaving it in its metallic state on a Mo piece which served as the lid of the vacuum distillation apparatus. In the second stage the ^{7}Be was distilled from this surface onto the Mo target backing. This process yielded targets of very high purity, ranging from 40-63% by atom number. The three targets used in our cross section measurements had initial activities of 106 mCi, 112 mCi, and 340 mCI, again in chronological order.

2.1.1 Target Backing

The targets included several features important to the uniform beam flux technique used in this experiment, see Section 3.1 below. The backings were 1.3 cm x 1.5 cm Mo plates with a raised post in the middle. The post was 1.5 mm high and 4mm in diameter. A washer was manufactured to tight specifications and then press-fit around the post. The two pieces where then machined flat together. After the ^{7}Be was deposited on this backing the washer was broken off to ensure that ^{7}Be remained on the target only on the post in a small, centralized region.

The targets possessed several features relevant to mounting it onto the rotating arm in the chamber. A bracket at the bottom and a flange at the top allowed it to be mounted securely and reproduceably onto the rotating arm in the chamber. A threaded rod in the top of the target allowed it to be manipulated with a long rod during the remote target mounting procedure. Stainless steel tubes were brazed onto the back side of the target backing and connected to the arm to allow it to be water-cooled.

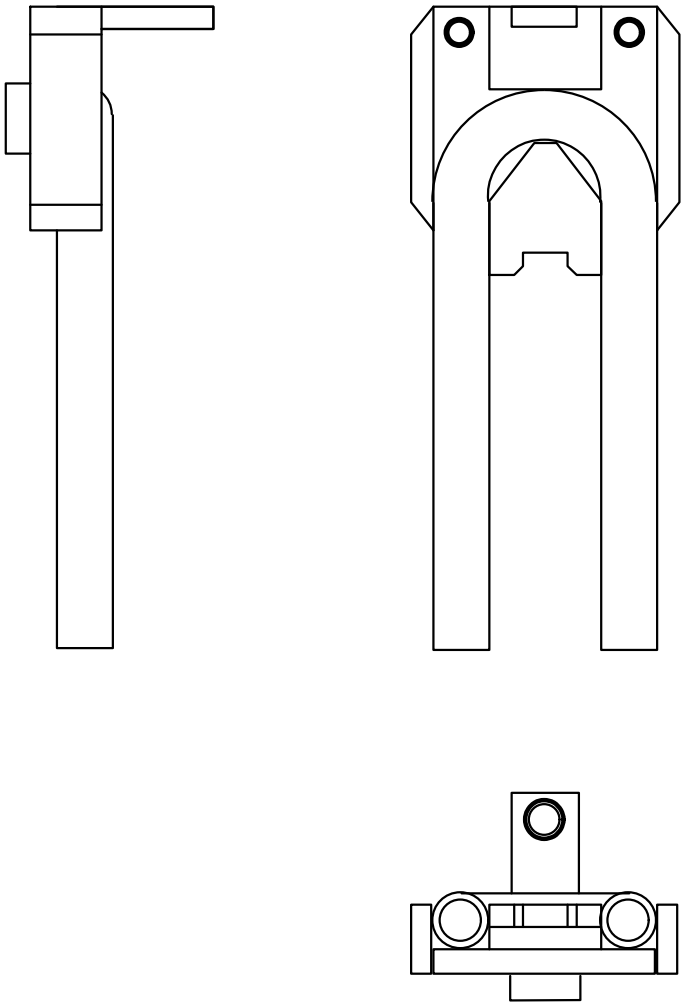

Figure 2.1: Schematic of a target backing.

2.2 Experimental Apparatus

The ^{7}Be(p,γ)^{8}B cross sections were measured at the University of Washington Center for Experimental Nuclear Physics and Astrophysics, using p, d, and α beams at energies of up to 3 MeV from the FN tandem Van de Graaff accelerator with a terminal ion source.

2.2.1 Accelerator Modifications

Several modifications, including the design and installation of the terminal ion source, were made to the accelerator for the experiment. Because the measurements were carried out at energies which are small compared to the maximum energy capabilities of the facility's accelerator it was not necessary to use the full capacity of the tandem Van de Graaff. Therefore a terminal ion source was designed and installed to produce much larger beam currents than were attainable using the full tandem and its traditional ion sources.

Transport of this high current and low energy beam through the accelerator was problematic. The measurement using the BE1 target utilized proton beams with energies as low as 220 keV. The low rigidity of these beams caused the spiral-inclined field tubes used in the accelerator to steer the beams in an unpredictable manner [35].

To improve this portions of the accelerating tube were shorted to make a steeper accelerating gradient at the beginning, with optics more favorable to the transport of the beam. Because measurements were made with energies ranging from 220 to 1371 keV, and with multiple particle beams, more than one such gradient was required. This necessitated entry into the accelerator several times over the course of an experiment. This technique allowed proton beams of 16 μA to be placed on target.

For the experiment utilizing the BE3 target an accelerator tube with a "flat" or "straight" accelerating field gradient was acquired and installed in place of the

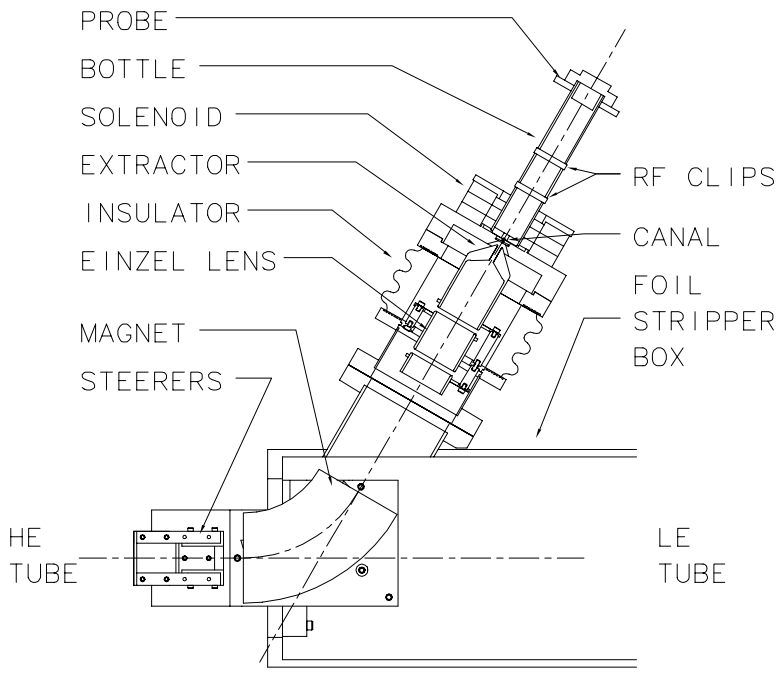

Figure 2.2: Schematic of the terminal ion source [30].

first high-energy spiral field tube section. This allowed us to attain even lower beam energies (as low as 150 keV) as well as higher beam currents, of up to 35 μA for protons.

2.2.2 Vacuum System

Safety and experimental goals led us to a non-standard vacuum system design. The use of a radioactive target required that the system not vent to atmosphere, and that it produce a minimal amount of contaminated parts. Our application made it desirable to have as few contaminants, particularly hydrocarbons, in the residual vacuum as possible. This was partially realized by avoiding the use of mechanical pumps.

For roughing we used three Huntington SP-151 sorption pumps filled with zeolite. The pumps were cooled in liquid nitrogen and then opened to the target chamber in sequence. Once they were finished pumping the liquid nitrogen was removed and the pumps rejuvenated by heating to drive off the adsorbed gases. The vent line went through a HEPA filter which was monitored at all times with a 3"x3" NaI detector for any buildup of activity.

High vacuum was achieved with a Cryo-torr 8 He cryopump. When necessary the cryopump was rejuvenated through a HEPA filter that was monitored by the same NaI detector system.

Large liquid nitrogen cold traps were used to improve the vacuum and prevent condensation of volatiles in the residual vacuum onto the target. A copper cold finger was placed 45 cm before the entrance of the beam tube into the target chamber. After entering the chamber the beam passed through a 31 cm long cylindrical cold trap with a copper sleeve that extended to within 1 mm of the target. This provided excellent shielding against condensible vapors as well as trapping ^{7}Be sputtered off of

the target during the course of the experiment. The cold trap had a removable lining to allow removal of the contamination after the experiment.

2.2.3 Target Chamber

The target chamber was designed to take advantage of innovations that have marked the development of measurements in ^{7}Be(p,γ)^{8}B. Silicon detectors were used to detect the αs from the decay of the ^{8}Be created in the target by the β-decay of ^{8}B. Scattered protons from the beam could make a large background in these detectors. To avoid this problem the target was mounted on a rotating arm and the Si-detectors were mounted away from the bombardment position, see Figure 2.3. In this manner the target could be irradiated in one position and then flipped in front of the detectors to count the β-delayed αs. Thin aluminum shields were mounted on the ends of the arm and at two places in the chamber to prevent particles in the beam from scattering into the Si-detectors.

While the α-particles were being counted an aperture plate on the other end of the arm allowed beam to pass into a faraday cup. This plate contained four apertures of nominal diameters 1, 2, 3, and 4 mm. The apertures were located 1.8 cm apart to prevent beam from passing through an adjacent aperture by accident. These apertures were sized by pressing precision-machined steel balls through holes which were slightly undersized. The roundness and diameter, and hence the area, of each aperture was measured to a precision of $\pm$0.2% with a SmartScope$^{\text{TM}}$, a precision microscope with a traveling stage.

An electron suppressor ring was mounted on the front of the Faraday cup and biased to -300 V. The entire chamber was isolated from local ground so that the only electrical connection was through the signal cables of the detectors, with the electrical ground located at the data collection station. The target arm was isolated from the

chamber and biased to +300 V.

The servo-motor used to rotate the arm was located outside of the target chamber for several considerations. Vacuum motors can introduce contaminents into the vacuum, which the chamber was designed specifically to avoid. In addition, the Si-detectors picked up electronic noise from the motors, and the problem became worse with proximity and without the shielding of the chamber wall between them. The motor rotated a shaft which was coupled to another shaft through an insulating bellows. This second shaft passed into the chamber through a ferrofluidic seal. Ferrofluidics have the advantage of being insulating and vacuum tight, even as a rotating seal. Water was flowed through this hollow shaft and into the arm to cool the aperture plate and the target, to counter beam heating.

A ^{148}Gd α-source was located near the Si-detector behind a moveable shutter. The source was used to monitor the detector gain between data runs by moving the target arm out of the way and rotating the shutter out of position.

A collimated Ge-detector with 50% efficiency was mounted on the lid of the chamber. The Ge-detector sat inside of a cylindrical Pb-collimator 6 cm thick which had a 2 cm diameter hole in its front face. When the target was on the arm and raised upwards in the vertical position it was located $\approx$27 cm from the detector and aligned with this hole. This collimator shielded the detector from 478 keV γ-rays from the decay of ^{7}Be that had been sputtered off of the target and was located on the cold trap or elsewhere in the chamber. Due to the high flux of γ-rays from the target an absorber was placed in front of the Ge-detector to attenuate the flux. The absorber consisted of 8 cm of Al and 5 cm of steel.

The chamber lid was designed to mount a portable Pb-shielded transfer device for the ^{7}Be targets. This device allowed the target to be transfered directly onto the arm using remote handling rods. If the arm was then rotated 180 degress, so that the

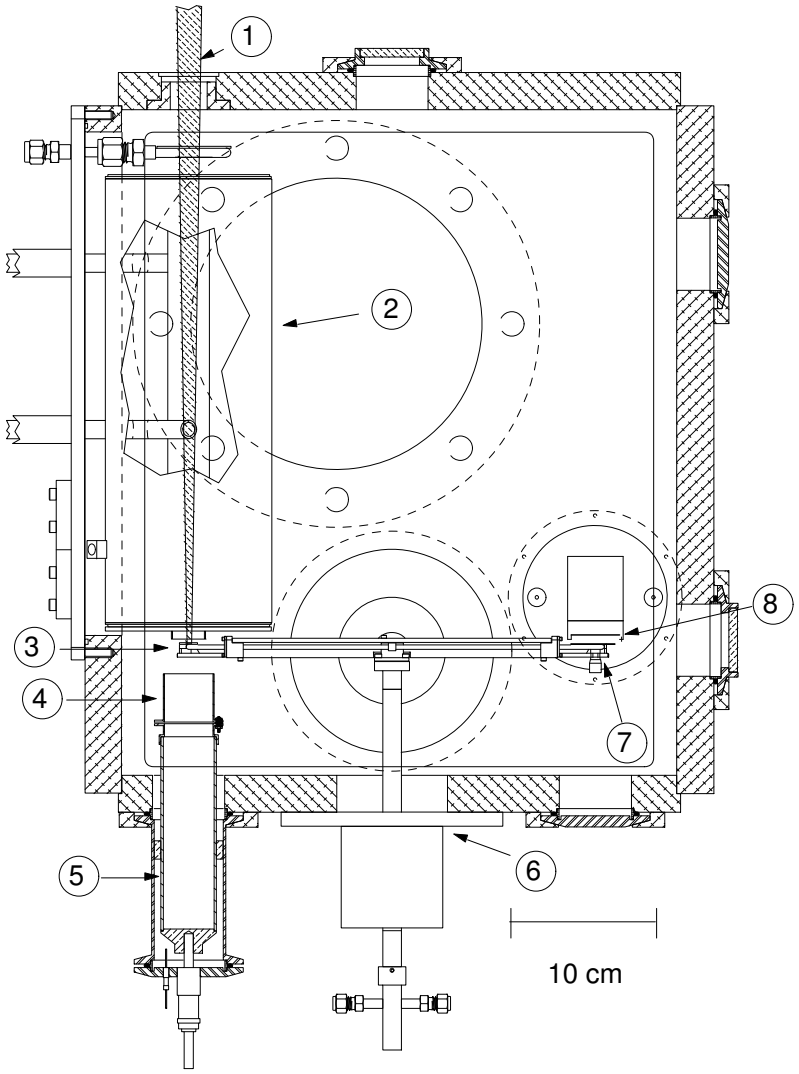

Figure 2.3: Top view of the target chamber with some features labeled. 1: a shaded taper representing the beam profile. 2: the large cylindrical LN_2 cold trap. 3: the target end of the rotating arm. 4: biased electron suppressor ring. 5: Faraday cup. 6: The ferrorfluidic seal where the rotating arm passes through the chamber wall. 7: aperture plate end of the rotating arm. 8: α-detector mount. Also shown are flanges on the sides and bottom of the chamber used for various purposes. The three flanges on the bottom were for pumping, the heavy-metal shield, and removal of the α-detector mount.

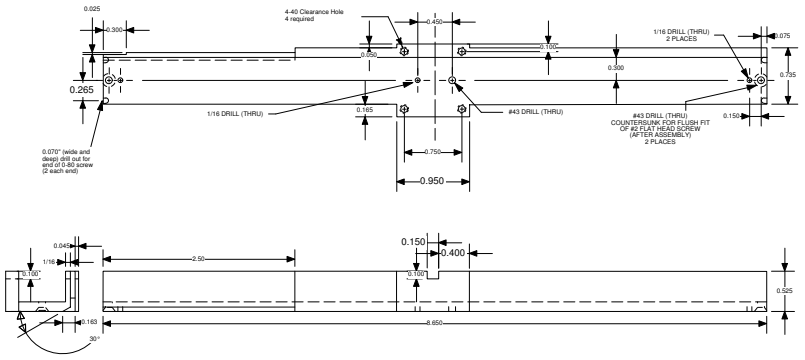

Figure 2.4: Schematic of the rotating arm.

target end was down, a heavy-met ([37]) shield could be raised around it, shielding the area from the γ-rays coming from the decay of ^{7}Be and allowing people to work in the area. A wall made of Pb bricks shielded the operator of the transfer device from γ-rays passing through the Al target chamber until the ^{7}Be target could be placed into the heavy-met shield.

A large, shielded NaI spectrometer was located on the side of the chamber closest to the irradiation position. The front of the detector's Pb collimator was $\sim$30 cm from the target irradiation position. The spectrometer was used for ^{7}Be(α,γ)^{11}C measurements of the target energy-loss profiles and ^{19}F(p,$\alpha\gamma$)^{16}O resonances measurements used in the accelerator-energy calibration.

The beam line utilized two magnetic quadrupole lenses, located 2 m and 6 m upstream of the target, to focus the beam sharply, two sets of deflection coils to vertically and horizontally steer the beam, and two more sets of deflection coils 1.1 m upstream of the target to raster the beam (see Section 3.1.1). Small horizontal and vertical pick-up coils were located inside of the rastering coils to monitor the magnetic field.

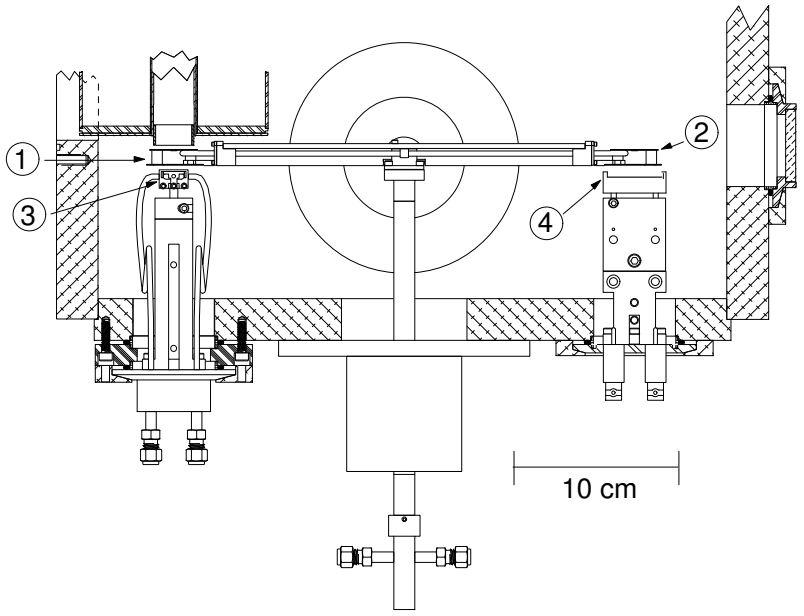

Figure 2.5: Backscattering apparatus. 1 and 2: catcher plates; 3: fixed target and water-cooled mount; 4: α-detector.

2.2.4 Backscattering Apparatus

Weissman et al. [65] pointed out that earlier ^{7}Be(p,γ)^{8}B experiments suffered unknown losses of ^{8}B due to backscattering out of the target, and similarly, ^{8}Li losses when ^{7}Li(d,p)^{8}Li was used as the absolute normalization for cross-section measurements. To guard against this we made modifications to our target chamber which allowed us to make the first (and to date only) measurements of ^{8}B backscattering loss. The modified portion of the chamber is shown in Figure 2.5.

The target was placed in a water-cooled, fixed mount which was installed in place of the Faraday cup. Large copper catcher plates where placed on both ends of the arm. Each plate had a 4 mm aperture at its center to allow the beam to pass through and strike the target. Backscattered ^{8}B were then caught on the catcher plate which

rotated to the far side of the chamber in front of a Si-detector located on the upstream side of the arm.

The arm and the target were both biased to +300 V. There was significant crosstalk of the secondary electrons created by beam striking the arm and/or target. While the individual currents on the two could not be accurately measured, but the total current could be measured reliably. Beam tuning was checked before and after the backscattering measurement using a Faraday cup.

2.3 Electronics and Instrumentation

2.3.1 Data Acquisition System

Computer Automated Measurement And Control (CAMAC) was used to read signals into a VAX/VMS SI-9900 Controller Data Acquisition computer (the DAQ) operating with the TUNL XSYS system. XSYS was used for online analysis as well as acquisition.

2.3.2 Silicon Detectors Electronics

The alpha detectors were totally depleted silicon diode detectors, held at operating bias by an Ortec 710 power supply. The detectors were hooked up to Ortec 142C pre-amps, which fed through an Ortec 571 amplifier into Northern TN-1213 ADCs, and then into the Data Acquisition (DAQ) computer.

2.3.3 Germanium Detector Electronics

An Ortec Germanium detector was used to monitor gamma radiation from the target to maintain a record of target activity. The 50% efficient Ge detector was held at bias by an Ortec 659 power supply. The output of the detector was shaped with an

Ortec 672 Spectroscopy Amplifier, and then fed into a Northern TN-1213 ADC for digitization for use in the DAQ.

2.3.4 NaI Spectrometer

A NaI spectrometer was used in the experiment for the detection of neutral particles, including γ rays and neutrons. At the core of the spectrometer was a 10"x15" NaI crystal scintillator. This was housed in a light tight casing, and surrounded on all sides by at least 2 inches of lead shielding, except a 6" diameter collimator opening at the front of the detector. In between the lead shielding and the NaI was a plastic scintillator which was used as a veto counter.

The gain of the detector was stabilized via two parallel systems. A blue LED pulser was piped into the back of the crystal through a fiber optic cable . The signal of this light pulser was monitored, and the overall high voltage of the detector adjusted to maintain a constant gain. This canceled out drift that might happen due to temperature changes or other causes. The light output of the LED pulsers was stabilized using a separate feedback circuit. An electronic pulser was also monitored in software and used to gain stabilize the detector electronics.

The PMT bases on the NaI spectrometer suffered from aging. The gains of the various photomultiplier tubes were not consistent, and changed with time, mostly due to temperature effects. We made new photomultiplier bases utilizing a printed circuit board. Several board layouts were tested to optimize the timing resolution and energy response of the detector. The final configuration of the PMT bases is shown in Figure 2.6.

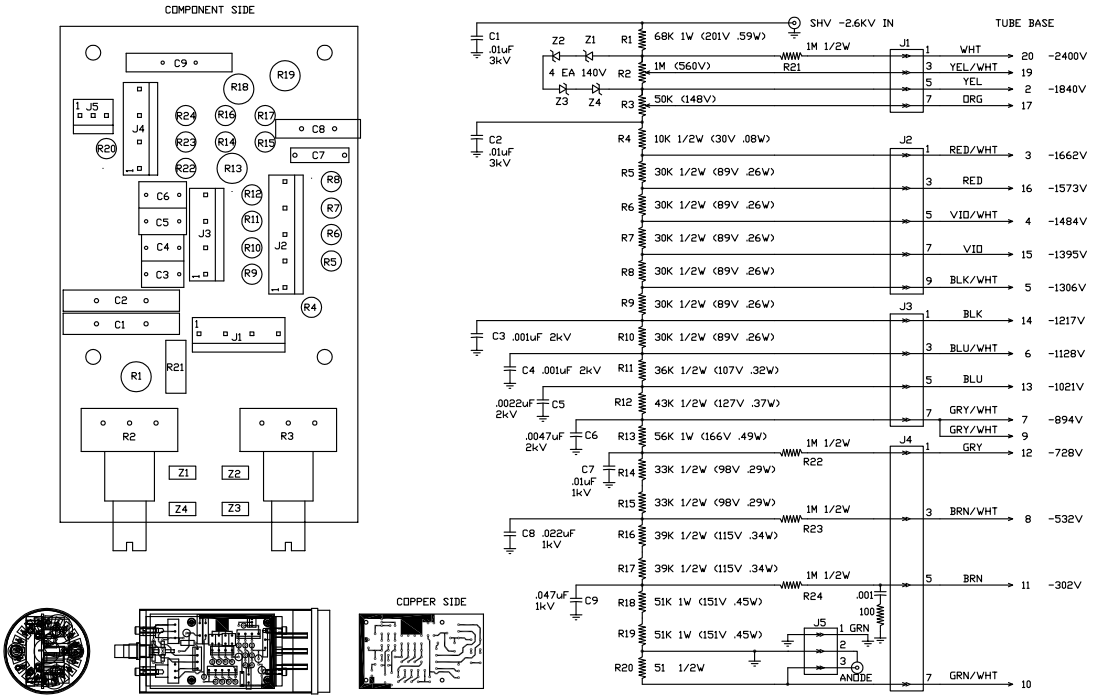

Figure 2.6: Schematic and circuit diagram for the photomultiplier tube bases of the NaI spectrometer [30].

Chapter 3

EXPERIMENTAL PROCEDURE

This experiment was designed as a precision measurement of the ^{7}Be(p,γ)^{8}B absolute cross section at low proton energies. It included precision determinations of systematic uncertainties in the measurement, most notably the effect of backscattering on the measured reaction cross section, as well as the accelerator energy calibration, the effect of beam and target non-uniformities, the target energy thickness, and the effects of sputtering on target activity.

In this chapter we describe the key elements of our precision cross section determination, including:

- Uniform beam flux technique, Section 3.1.
- Rotating target arm, Section 3.2.
- Solid angle, Section 3.3
- Energy loss determination, Section 3.4
- Accelerator energy calibration, Section 3.5
- Target activity determination, Section 3.6
- α Yield determination from ^{7}Be(p,γ)^{8}B α-spectra, Section 3.7
- Backscattering measurement, Section 3.8

3.1 Uniform Beam-flux Technique

Experiments are not able to measure directly a cross section or S-factor. Instead, experiments measure a reaction yield from which a cross section is determined. The yield Y is related to the cross section σ by:

$$Y = \frac{\sigma}{q} \int \frac{dN}{dA} \frac{dI}{dA} dA \ , \tag{3.1}$$

where dN/dA is the areal density, dI/dA is the beam current density, q is the charge of a beam particle, and the integral is over the target area.

The usual method of performing a nuclear physics experiment is to irradiate a large-area target with a beam whose size is much smaller than the target area. In the limit where the target areal density is constant this equation reduces to the expression:

$$Y = \frac{\sigma}{q} \frac{dN}{dA} I, \tag{3.2}$$

where I is the total beam current.

Because of target nonuniformity this approximation contributes an uncertainty that can dominate a precision measurement (see, for example, Ref. [26]). It is very difficult to characterize this uncertainty since it depends on the convolution of the target areal density dN/dA, and beam flux dI/dA. Often neither is measured or known.

In the early planning stages of this experiment we[2] proposed a way to simplify Eq. 3.1 by making a beam of uniform flux over an area larger than the target. In this limit Eq. (3.1) reduces to

$$Y = \frac{\sigma}{q} N \frac{dI}{dA}, \tag{3.3}$$

where N is the total number of target atoms. It is important to note that this result for Y is independent of $\frac{dN}{dA}$.

We used this method, which provided several advantages over the traditional technique. Of special relevance to this experiment, it is very difficult to make a target of uniform $\frac{dN}{dA}$ from radioactive materials. We were able to determine N precisely by measuring the ^{7}Be activity. dI/dA was determined by measuring the beam current transmitted through various sized apertures, and adjusted to be uniform to high precision, using the technique described below.

3.1.1 Beam Rastering

There are three key elements to Eq. 3.3. First we produced a nearly-uniform beam flux. Next we determined the flux precisely, and then we determined the uncertainty in our use of Eq. 3.3. Each of these steps is described below.

To achieve a highly uniform beam flux we first tuned the beam to pass as much current as possible through a 1 mm aperture. Typically more than 60% transmission was achieved. The beam was then uniformly rastered over an area approximately 7x7 mm^2 by using magnetic rastering coils driven by a triangular voltage wave form. The horizontal and vertical rastering coils were driven at the incommensurate frequencies of 19.03 Hz and 43.00 Hz, respectively. This choice of rastering frequencies minimized any "beat" irregularities of the beam passing through the aperture during the counting phase of the arm-rotation cycle or illuminating the target during the irradiation phase.

Magnetic pick-up coils inside the rastering deflectors allowed us to monitor the rastering pattern as well as correlate the drive voltage with the resultant magnetic field. By performing aperture scans, as described in Section 3.1.3 below, these quantities could be related to the size of the beam at the target and the uniformity of the beam over the target region.

3.1.2 Current Integration

The rotating arm was isolated from the chamber and biased to +300 V to minimizes losses of secondary electrons. The Faraday cup had an electron suppressor ring mounted in front of it and biased to -300 V. The beam current striking the target arm and the beam striking the Faraday cup were integrated separately. Just before rotating the arm the beam was swept off the arm by the magnetic rastering coil.

We recorded the following charges, integrated over many complete arm rotation cycles:

- Q_T - integrated beam striking the target during the bombardment phase
- Q_A - integrated beam striking the aperture during the counting phase
- Q_C - integrated beam passing through the aperture and striking the Faraday cup during the counting phase.

By design, we expected Q_C to be our standard measurement of the beam current, taken with a Faraday cup in a "good" geometry. We used the measure$(1/q)Q_C/A$ of the flux ϕ transmitted through the aperture, where A is the area of the aperture.

The target had an area in between that of the 3 mm and 4 mm apertures (see Section 3.1.3 and Fig 3.1). Because the flux was the same through the 3 mm and 4 mm apertures (see Fig. 3.2) we used this flux as a measure of the flux striking the target area. We assumed that this flux was the same as that which strikes the target end of the arm during the bombardment phase, due to the averaging and integration over many complete cycles of rotating the target arm.

This assumption was measured and quantified with the use of the second current integrator on the arm. Seeing that $Q_C/(Q_C+Q_A)$ is a measure of the fraction of the total beam that passes through the 3 mm aperture we can construct $Q_T\ Q_C/(Q_C+Q_A)$.

This scales the total beam striking the target assembly during the bombardment phase by the fraction of the beam within a 3 mm radius of the center to determine the beam striking the central 3 mm of the target. A series of test runs showed that the ratio of Q_C to Q_T $Q_C/(Q_C+Q_A)$ was 1.0002±0.0080, where the uncertainty was determined from the internal fluctuations of the data. This showed that current integration on the target end of the arm was as accurate as integration in the more idealized geometry of the Faraday cup, to the precision measured.

We also made diagnostic runs with the high yield ^{7}Li(d,p)^{8}Li reaction. These measurements allowed us to compare aperture flux measurements to reaction yields with varying magnitudes of beam rastering. There were smaller run to run fluctuations when normalizing to Q_T $Q_C/(Q_C+Q_A)$ instead of Q_C. Because of this we adopted the normalization of ϕ_p=(1/q)Q_T $(Q_C/A)/(Q_C+Q_A)$.

Additional checks were made of the overall beam integration accuracy. We varied the bias on the Faraday cup's supressor ring in the range of -300±45 V and found <0.5% change in the measured beam current. We also tested for neutral H in our beam which would produce ^{8}B yield but would not appear in our integrated charge. To make this test we tuned a proton beam at 490 and 355 keV onto a thick LiF target and measured the yield of the strong ^{19}F(p,$\alpha\gamma$)^{16}O resonances at the 340 and 484 keV with our NaI detector. We then used our magnetic deflectors to deflect the charged hydrogen beam away from the target and repeated the measurement. The largest rate measured in any of the beam deflected runs was 0.02% of the undeflected runs, and averaged $<2.5*10^{-5}$ of the undeflected rate. The counting rates for runs with the beam deflected were consistent with beam off backgrounds.

Combining the 0.8% uncertainty from the ratio of Q_T $Q_C/(Q_C+Q_A)$ with the ≤0.5% variability with bias voltage in quadrature, and neglecting the negligible contribution from neutral hydrogen, we assigned a ±0.9% overall systematic uncertainty

to the integrated beam flux.

3.1.3 Beam and Target Uniformity Measurements

Because our technique depended on having a nearly uniform flux over the target we made a substantial effort to measure and model both the beam and target properties.

Our first method of measuring the target density profile used ^{7}Li in the target. Rastering the beam in only one direction gave us a thin line which could then be stepped across the target using the other rastering coil. The yield/charge of these experiments was used to make a two dimensional target profile. Because ^{7}Li is the decay product of ^{7}Be we expected that they would have the same density distribution within the target. Over the course of these measurements we found that the ^{7}Li density profiles changed with time. In particular the target profiles changed under irradiation or if the targets were left exposed to air for extended periods of time. Because of this we abandoned the use of ^{7}Li for this diagnostic.

Instead the target profile was measured at TRIUMF by placing it on a moveable stage and passing it in front of a collimated Ge detector. A 51 mm thick heavy-met[37] block with a narrow slit in it allowed the Ge detector to view the γ-activity of the target and was used to create profiles such as that shown in Figure 3.1. Measurements were done with 0.125 and 0.250 mm slits, as well as with a closed slit. The target was scanned facing the detector in two orientations and edgewise. This side view was used for two purposes. It showed that no significant ^{7}Be activity was located anywhere except on the top of the target post, and it allowed us to see the response of the detector to a line source, which was used as a resolution function when analyzing the scans with the target facing the detector.

From these measurements we determined that the targets had a flat central region which fell off linearly, or nearly so, to zero at a larger radius. The BE1 and BE3

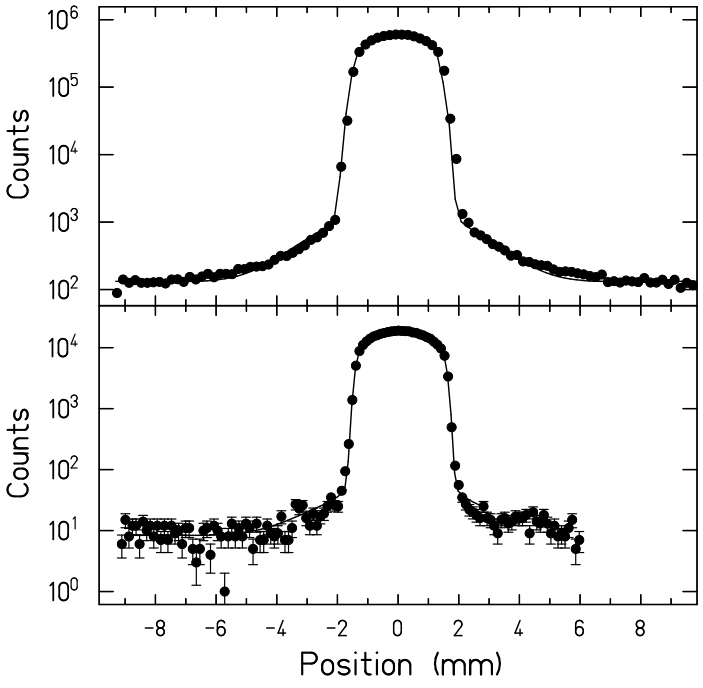

Figure 3.1: An activity scan of BE3. The top panel is the target before ^{7}Be(p,γ)^{8}B measurements and the bottom panel is after. The solid curves are calculated density distributions folded with the detector resolution and fit to the data.

targets both had a constant density distribution inside 1.5±0.01 mm and zero density beyond a radius of 1.8±0.01 mm.

Measurements were also made to determine the uniformity of the beam. The sequencer box (see Section 3.2) was utilized in such a way as to place each of the apertures on the aperture plate end of the arm into the beam for an equal time interval. We cycled through the series of apertures several times and then used the current measurements in the cup to determine the beam flux through each aperture.

By slightly increasing the physical size of the beam raster pattern, by increasing the driving voltage for the magnetic raster coils, and remeasuring we mapped out a curve of the flux through each aperture vs. beam raster size. The more intuitive representation of this is to show ratios of the yields through various sized apertures, see Figure 3.2. When all possible ratios of fluxes between the available apertures have converged to one then the beam flux is uniform at least over the area of the largest aperture, which was 4 mm in diameter.

We were also able to measure directly the quantity of interest, namely the full convolution shown from equation (3.1). Using a deuteron beam, E_d=770 keV, we took advantage of the high yield of the ^{7}Li(d,p)^{8}B reaction. Because the ^{7}Li in the target is the decay product of the ^{7}Be its physical distribution in the target should be similar. The yield of the ^{7}Li(d,p)^{8}B reaction was measured as a function of the driving voltage of the magnetic raster coils. Where the curve flattens out at its maximum value the beam is uniform over the entire target.

The correspondence between the point at which the aperture scan flattened out and the yield scan flattened out allowed us to use the aperture scan to determine what raster amplitude to use for our measurements with proton beams at each energy, where the (d,p) yield vs. raster curve could not be measured.

Measurements were also taken with a uniform 3mm radius LiF target utilizing

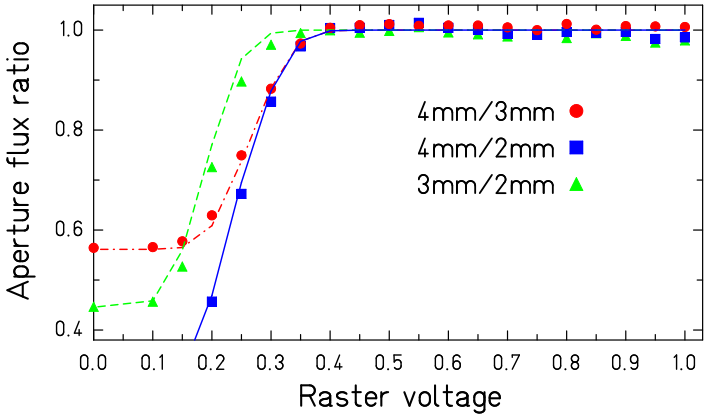

Figure 3.2: Ratios of the beam flux through various sized apertures of 770 keV deuterons vs. raster amplitude. The curves were calculated as discussed in Section 3.1.4

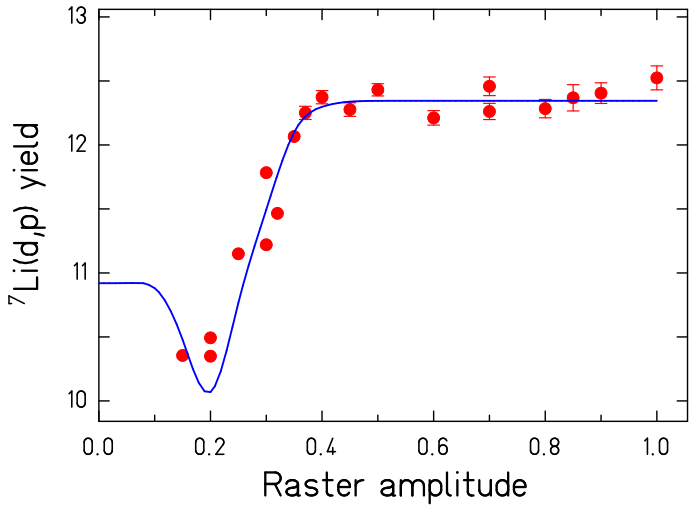

Figure 3.3: ^{7}Li(d,p)^{8}B yield at 770 keV, normalized to the beam flux through the 3 mm aperture, measured vs. the amplitude of the raster. This data is taken with the same beam tune as that used to measure the yield curve in Figure 3.2. Errors are statistical. The curve is the calculated yield with a fitted misalignment of 0.5 mm, as discussed below.

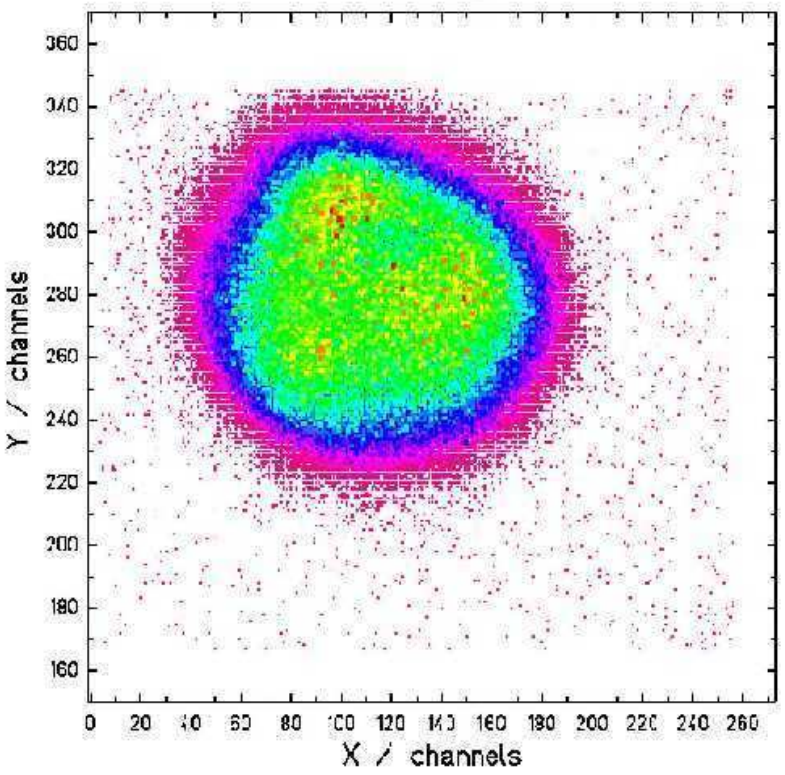

Figure 3.4: Yield of a measurement of ^{19}F(p,$\alpha\gamma$)^{16}O plotted as a function of the location in the target where each event happened.

the ^{19}F(p,$\alpha\gamma$)^{16}O reaction and the NaI spectrometer. During these measurements the yield was measured promptly while the target was in beam. We were able to digitized the signal from the pickup coils inside the magnetic raster coils and used it to determine the location of the beam for each event. Figure 3.4 shows a distribution of event locations in the target. This measurement provided additional evidence that the rastering pattern covered the whole target, and did not over-sample a particular location.

3.1.4 Beam and Target Uniformity Calculations

We made calculations to confirm our understanding of the yield and aperture scans discussed in Section 3.1.3. The unswept beam and the target displayed rotational symmetry, and the rastering pattern used to generate a uniform beam flux had a Cartesian geometry. The convolution of these objects yielded no symmetry, and thus the calculation could not be carried out in closed, i.e. analytic, form. Numerical calculations were carried out using the MATLAB software package.

We assumed that the beam intensity distribution was a two dimensional gaussian, with σ_x=σ_y, before rastering. With this assumption and the measured fractional beam transmission through the 1 mm aperture, the gaussian width of the beam could be calculated. Calculations based on transmission data through other apertures yielded similar beam widths, demonstrating that the beam intensity was close to the gaussian profile assumed.

Information on the fraction of the beam transmitted through the 3 mm aperture was measured at many different rastering drive voltages. A uniform square raster pattern was convoluted with the unrastered beam profile calculated in the previous step to represent the rastered intensity distribution. The size of the raster at each driving voltage was fit using Newton's method and the transmission information was tabulated. A relation between the physical size of the raster and the drive voltage was determined in this way, and it was found that the relation was linear across all relevant drive voltages. It was necessary to digitize the beam on a grid with 1000 bins per mm to achieve an accuracy of 0.1%.

With this information it was possible to proceed one step further and calculate a curve of yield vs. raster amplitude similar to that measured with the ^{7}Li(d,p)^{8}B reaction and described in the previous section. For the purpose of these calculations a two dimensional target distribution was generated based on the information from

the target scans discussed above in Section 3.1.3. The target density distribution was digitized on the same grid as that used for the beam, for ease of calculation.

Convoluting the beam profile with the target density distribution, using no free parameters, gave a yield vs. raster plot which was similar to that measured experimentally, but lacked some features, most notably the dip and rise at the lowest rastering amplitudes. We discovered that the two ends of the arm were not located in the exact same location when rotated into the irradiation position, i.e. there was a misalignment between the aperture end of the arm and the target end of the arm. Since the beam was tuned and centered on the aperture this meant it was slightly off-center on the target. This misalignment was measured to be 0.48±0.07 mm with an optical telescope.

When a possible misalignment was allowed in the calculations as a free parameter, excellent agreement was found between the calculated and measured yield vs. raster amplitude. The fitted misalignment of 0.5 mm was in excellent agreement with the measured value.

Removing the misalignment would have allowed taking data with a slightly smaller rastering voltage, and therefore a slightly larger beam flux. Because we always ran at raster amplitudes above the measured beam flux uniformity threshold (as seen in Figures 3.2 and 3.3) this misalignment caused no loss of precision.

3.2 Arm Rotation Cycle

The use of a rotating arm was important in allowing us to count the α-particles from the breakup of ^{8}Be away from the large background of the accelerator beam. The finite half-life of ^{8}B, $t_{1/2}(^8\mathrm{B}) = 770\pm3$ ms[15], allowed us to use this technique. It was necessary to account correctly for the fraction of the ^{8}B decays counted by the α-detector. The result is a counting efficiency $1/\beta(^8\mathrm{B})$, where β is defined by:

$$\beta(^8\mathrm{B}) = \frac{\lambda t_1[1 - e^{-\lambda(t_1+t_2+t_3+t_4)}]}{(1 - e^{\lambda t_1})[e^{-\lambda t_2} - e^{-\lambda(t_2+t_3)}]}, \tag{3.4}$$

where $\lambda = \ln(2)/\mathrm{t}_{1/2}(^8\mathrm{B})$.

Since readily available computer operating systems, such as Windows, are not capable of performing tasks at precisely defined real time intervals, we used a hard-wired sequencer box to control the timing and movement of the arm. The duration of each period was measured with a precision pulser operating at 148.803 MHz and the relative timing of channels was checked with a fast storage scope. The bombardment period with the target in the beam is labeled t_1 and was measured to be 1.50021±0.00023 s in duration; t_2 = 0.24003±0.00004 s was the time to rotate the target from the irradiation position to the counting position; $\mathrm{t}_3 = \mathrm{t}_1$ is the counting period with the target in front of the detector and the aperture in the beam, and t_4 = 0.26004±0.00004 s is the time to rotate the target back to the bombardment position. Although the motor was capable of flipping the arm much more quickly than the quarter-second allocated to this movement, this interval was chosen for several reasons. A slower rotation of the arm reduced stresses on the arm and target which helps avoid mechanical failure. It also allowed time for the arm to settle in its final position after possible arm vibrations had damped out. The motor induced noise in the α-detectors while it was operating, and this extra interval allowed us to be certain that this noise was excluded by a timing gate and did not intrude into the counting period.

The positioning of the arm was important for all portions of the rotation cycle. The target must be located precistely in the bombardment position to insure proper irradiation. Arm positioning was also critical when the target was in the measurement position. The target was held steady in a reproducable location such that the detector subtends a constant solid angle. Two methods were used to verify that the arm was in

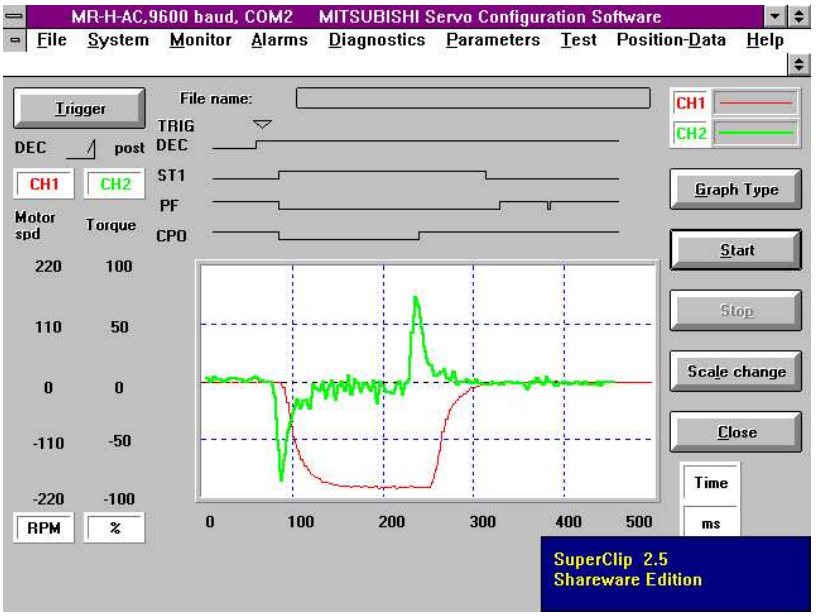

Figure 3.5: The display of the motor encoder control program. The PF signal above the graph is the in-position signal for the arm. Flutter in the signal after it first goes high was attributed to vibrations of the arm which quickly damp out. The graph shows velocity (red line) and acceleration (green line) of the motor arm.

position during the course of the experiment. The motor encoder had an "in position" signal triggered when the motor arrived at the designated position. As can be seen by examing the bit labeled PF in Figure 3.5, the resolution of this signal is fine enough to detect small oscillations in the arm after the rotation. The counting gate started long enough after arm movement that the "in-position" signal was steadily on.

To further monitor the arm movement we mounted a small mirror on the shaft of the motor. When the arm was in the counting position a laser reflected off of this mirror to a marked position on the wall $\approx$ 10 m away. A mispositioning of the arm by 1 encoder step ($1/16{,}384^{th}$ of a rotation) was obvious to the naked eye.

Because some fraction of the ^{8}B produced in a given cycle will remain in the target at the beginning of the next bombardment period it takes a few complete cycles to

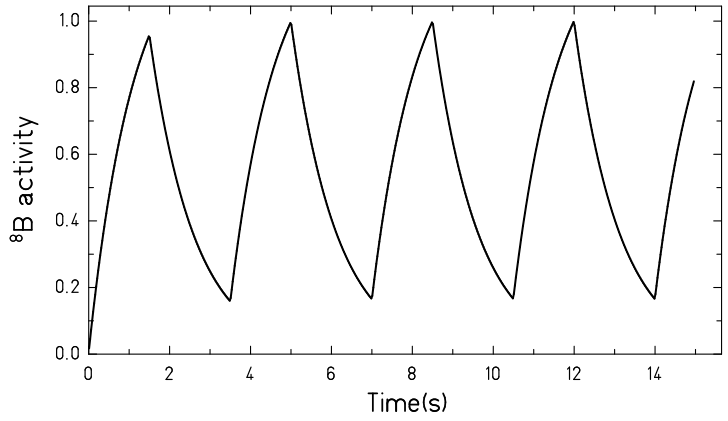

Figure 3.6: A plot showing the calculated build up of ^{8}B in the target as a fraction of maximal concentration. The activation and decay of ^{8}B in the target can be seen over each cycle, as well as the increase in the average amount of ^{8}B until equilibrium is reached.

reach a steady equilibrium state. For this reason it is important to count over many cycles to minimize the effect this can have on the measured yield (see Figure 3.6). After two cycles the ^{8}B activity is within 0.07 % of its equilibrium value. The effect of this becomes negligible ($\ll 0.1\%$) after 50 cycles ($\sim$ 3 minutes).

Data runs were always taken with a large integer number of cycles, giving an overall $\beta(^8\mathrm{B})$=2.923$\pm$0.006.

3.2.1 Alternate Flipping Cycles

During the ^{19}F(p,$\alpha\gamma$)^{16}O accelerator energy calibration measurements (see Section 3.5) and ^{7}Be$(\alpha,\gamma)^{11}$C resonance profile measurements to determine the energy thickness of our targets (see Section 3.4), a large NaI spectrometer (see Section 2.3.4) was used to measure prompt γ-ray yields while the target was in the beam. In this mode the prompt yield was measured while the target was being irradiated, so the timing effi-

ciency factor β is unity. Even so, for these measurements we rotated the arm to place the aperture end of the arm in the beam during part of the cycle. This allowed us to compare the integrated beam flux in the Faraday cup, to that measured on the target during irradiation (see Section 3.1.2).

To maximize the amount of time spent collecting data, the flipping cycle was changed from the nearly symmetric cycle used in the ^{7}Be(p,γ)^{8}B measurement to a ten second cycle in which 80% of the time was spent with the target in the beam (and therefore taking data), and 15% of the time was spent with the aperture in the beam. The remaining 5% of the time was allocated to flipping the arm, although the arm actually rotated much more quickly than that. As before, extra time was allocated to remove any concern about arm vibration or electronic noise from the servo motor.

The sequencer box was also utilized to make aperture scans as detailed in Section 3.1.3. The accuracy of the sequencer box timing was checked in each of these alternate cycles with a precision equivalent to that reported above, and did not contribute to the overall errors with any significance.

3.3 Solid Angle Determination

The α-particles from the decay of ^{8}B were detected with large-area uncollimated Si surface-barrier detectors positioned very close to the target, in order to maximize the measured yield. The properties of these detectors are listed in Table. 3.1. At close distance a small target-to-detector distance uncertainty corresponds to a large uncertainty in solid angle. For example, at the distance of $\sim$5 mm used in the BE1 measurements a distance uncertainty of 0.1 mm results in a 1.1% uncertainty in solid angle.

For the BE3 measurements we made data runs with two different detectors. The first series of measurements were made with the same detector used in the BE1

Table 3.1: Physical properties of Si-detectors.

Detector	Active Area	Thickness
Counting (S)	134 mm^2	20.4 μm
Counting (L)	416 mm^2	32.7 μm
Calib	407 mm^2	34.6 μm

experiment, which we labeled "L" for large. We also made cross-section measurements using a smaller detector, labeled "S." The L detector was ≈416 mm^2 and 33 μm thick, and the S detector was ≈139 mm^2 and 20 μm thick. Use of the thinner detector helped minimize the portion of the ^{8}B α-spectrum lying below the experimental threshold. The small (S) detector was located at 7 mm and the large (L) detector located at 14 mm. For these detectors a 0.1 mm distance uncertainty would result in 1.9% and 1.0% solid angle uncertainties, respectively.

Because of this sensitivity conventional geometric measurements were not satisfactory for determining the solid angle. In addition, the outside glued edge of the detectors was not well defined, making it impossible to know precisely the active area of the detectors. Therefore we used a second "calibration" Si-detector, placed in a "far" geometry to minimize the effects of geometrical uncertainties. By measuring the ratio of the solid angle in the two detectors we could then determine the solid angle of the near detector accurately using:

$$\Omega_{close} = \Omega_{far} N_{(close/far)}, \tag{3.5}$$

where Ω is the solid angle in the indicated detector and N is the ratio of the two solid angles measured in one of two methods described below.

Because the far detector is used as the reference for all solid angle measurements it

is important to determine its solid angle very accurately. The solid angle of this second detector was defined by a precision machined stainless steel 2 μm thick collimator. Using a very thin collimator allowed us to precisely determine the source-to-collimator distance. The area of the collimator was measured using a SmartScope^{TM} to be 248.8$\pm$0.4 mm^2. The SmartScope^{TM} is a precision traveling microscope and computer interface with a precision of better than .0025 mm. The SmartScope^{TM} also allowed us to measure the roundness of the collimator to assure our collimator had a uniform radius, and therefore a well determined area. To measure the source-to-collimator distance an outside caliper was made with a machine flat as one side of the caliper and a bar on the other side. The bar was held away from an electrical contact by a very weak spring. The caliper was used by inserting it into the region to be measured and opening it until the bar was depressed, thus creating an electrical contact and signaling an alarm. When the alarm went off we read the value from the caliper. This method allowed us to indicate contact, and therefore separation, in a reproducible way. Using this caliper we determined the collimator to be 47.42$\pm$0.09 mm away from the source mounted on the arm. The zero of the distance scale was double checked using a ^{148}Gd α-source.

In the BE1 experiment the solid angle ratio was measured using the high yield ^{7}Li(d,p)^{8}B reaction. Because ^{7}Li is the decay product of ^{7}Be we assumed, at the time, that these elements have the same density distribution within the target. If this were true measuring the solid angle for ^{7}Li in the same target as used for the ^{7}Be(p,γ)^{8}B cross-section measurements would avoid many problems. The solid angle measurement was made using a target in the same location and with the same areal size and distribution as the ^{7}Be target. During the BE1 experiment we discovered several issues that detracted from this method, as discussed below.

To make this measurement the BE1 target was mounted on the end of the rotating

arm, irradiated and then rotated in front of either the "near" detector used in the ^{7}Be(p,γ)^{8}B cross-section measurements, or the far detector. Replacing N in equation 3.5 with the appropriate quantity we see that:

$$\Omega_{close} = \Omega_{far} \frac{Y_{\alpha(close)}}{Y_{\alpha(far)}}, \tag{3.6}$$

where Y_α is the α-particle yield divided by the integrated beam flux on target. We calculated corrections to the yield for the fraction of the α-particle spectrum which lay below the experimental threshold. Because the shape of this spectrum depended upon opening angle it was different in the two detectors and the corrections did not cancel in the ratio. These calculations are discussed in more detail in Section 3.7. Because the solid angle of the far detector was used as a reference for all other measurements we used different sized collimators on the far detector in redundant measurements to provide checks of its solid angle.

The α-spectrum cutoff correction factors were a source of uncertainty that cannot be measured, and therefore had to be taken from modeling calculations. In addition, it is known that ^{7}Li diffuses easily, particularly into metals, such as the backing for the targets. If the ^{7}Li was redistributed or lost during irradiation the ^{7}Li(d,p)^{8}B calibration would not give the proper solid angle for the ^{7}Be(p,γ)^{8}B measurements. Therefore we abandoned this techique for the BE3 experiment.

For the BE3 experiment a fixed source mount was precision machined to hold a ^{148}Gd α-source in front of the detector. The source was fabricated at TRIUMF by depositing the ^{148}Gd on the same kind of target backing used to make the ^{7}Be targets. Several trials were needed to create a source with a good line shape and a small tail (see Figure 3.7). Using an α-decay source provided us with a line shape which required a much smaller, or in some cases completely negligible, correction for the fraction of the counts which lay below the low energy experimental threshold. After measurement in

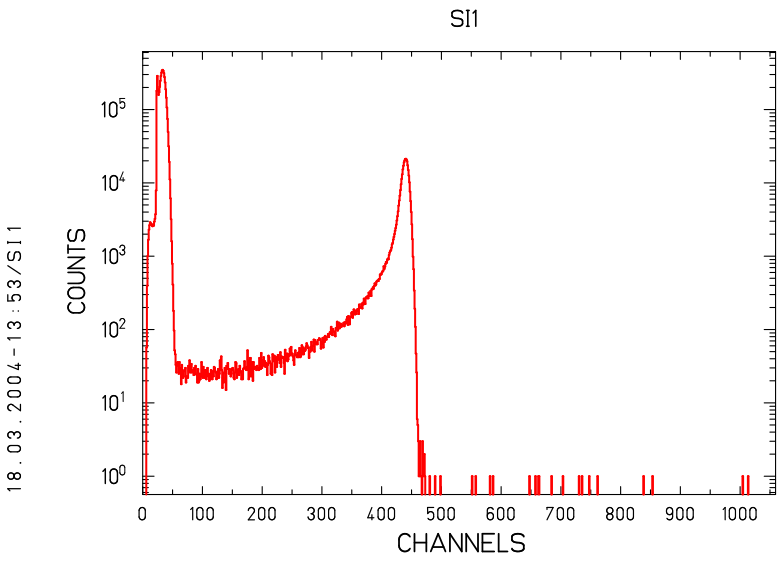

Figure 3.7: A spectrum from the ^{148}Gd source used in our solid angle determination.

the fixed mount the source was mounted on the arm and remeasured in the calibration detector to provide an additional cross-check. Finally, measurements were made with the source mounted on the arm and rotated to place the target in front of the close detector in the position used for taking ^{7}Be(p,γ)^{8}B data.

Using this technique, equation 3.5 now becomes:

$$\Omega_{close} = \Omega_{far} \frac{R_{close}}{R_{far}}, \tag{3.7}$$

where R is the counting rate of the ^{148}Gd source in the designated detector.

Our radioactive ^{7}Be targets couldn't be measured on the SmartScope^{TM} so we needed to make a different series of measurements. To do this the arm was taken out of the chamber and mounted on a precision jig where it could be examined with an optical telescope. The various targets and sources where then mounted on the arm and their positions measured to 0.03 mm. From this we applied corrections of

0.3±0.3% and 0.6±0.6% to the solid angles for the L and S detectors, respectively, to account for the 0.03±0.03 mm difference in the distance from the detector to the BE3 target and the TRIUMF ^{148}Gd source.

The close detector was mounted on a precision translation stage for the BE3 experiment which allowed measurements to be taken at multiple distances and checked against each other. In particular, it allowed us to use the small "S" detector at a smaller target-to-detector distance than the "L" detector, and to switch between the two detectors in an efficient and reproducible manner. This translation stage allowed us to make solid angle measurements at multiple distances to check for consistency. As an additional check these solid angle determinations were compared to geometrical measurements made in two ways, both of which took advantage of the translation stage.

In the first method we used our custom-made outside caliper to determine the distance at several positions of the translation stage. The distance was also measured by placing a machine flat of exact thickness between the arm and the detector mount and moving the stage in until the flat was held between the two. This calibrated the setting on the translation stage to the separation determined by the machined flat. In both methods a dial indicator was located on the back of the target arm to measure any deflection caused by the force on the front of the arm. These two methods agreed to 0.02 mm (1 σ).

Comparing the solid angle determined with the source to that measured by geometry showed some differences that were largest for small target-to-detector separations. In order to assure ourselves there was not an error in the measurement process we fit the data with:

$$\Omega = 2\pi(1 - (D - D_0)/\sqrt{(D - D_0)^2 + R^2}), \tag{3.8}$$

where D is the distance from the detector to the source, D_0 is an offset in the distance scale, and R is the radius of the detector. Because a small distance error could affect the solid angle significantly in these measurements and the aforementioned poorly known active area of the detector we allowed D_0 and R to vary as fit parameters. From these fits we saw that no combination of D_0 and R could characterize the data well.

Due to this we made additional measurements with many sources, including the ^{148}Gd source that was mounted on the arm, as well as commercially produced ^{148}Gd and ^{241}Am sources. The commercial sources had better line shapes than our sources, but did not have the advantage of being manufactured on the same backing as our ^{7}Be targets. There were enough complications that we eventually collimated the near detector with a steel shim with area of 81.07±0.19 mm for a series of measurements.

Because we did not have a scan of the α sources to tell us the source distribution we knew only that the activity was confined to the active regions of each. Calculations made for the ^{148}Gd source deposited on our target backing showed that the difference in solid angle for a point source at the center as compared to a source for which the activity spread uniformly over the possible region was comparable to the size of the deviations we measured. As such we believe the deviation from unity of the quantity $\Omega_{geometry(point)}/\Omega_{source}$ to be due to an unknown, but reasonable, source strength distribution.

The observed spread of these measurements led us to apply a ±1.5% systematic uncertainty to the solid angle for the BE3 experiment, as being representative of the effect of differing source distributions at the detector-to-target distance used in the measurement of the ^{7}Be(p,γ)^{8}B data.

Table 3.2: Solid angle information of the detectors used in the BE1 and BE3 experiments. Columns are: D_{far} - the distance from the target to the far detector, A_{far} - the collimated area of the far detector, Ω_{far} - the geometrically determined solid angle of the far detector, $\Omega_{far}/\Omega_{near}$ - the ratio of solid angles between the near and far detector, and Ω_{near} - the solid angle of the near detector computed from that ratio.

Experiment(detector)	D_{far}	A_{far}	
BE1	47.42±0.09 mm	248.8±0.4 mm^2	
BE3(L)	57.00±0.10 mm	246.0±0.3 mm^2	
BE3(S)	57.00±0.10 mm	246.0±0.3 mm^2	
Experiment(detector)	Ω_{far}	$\Omega_{far}/\Omega_{near}$	Ω_{near}
BE1	0.1078±0.0004 sr	35.44±0.38	3.82±0.04 sr
BE3(L)	0.0744±0.0003 sr	18.78±0.13	1.397±0.011 sr
BE3(S)	0.0744±0.0003 sr	24.17±0.39	1.798±0.030 sr

3.4 Energy Loss in the Target

Different techniques have been used in previous ^{7}Be(p,γ)^{8}B experiments to determine the energy thickness of the ^{7}Be target. The most common method was to measure the broadening of the 41 keV wide resonance in ^{7}Be(p,γ)^{8}B reaction at $E_p = 720$ keV. Other experimenters used the 12 keV wide resonance in ^{7}Li(p,γ)^{8}Be at $E_p = 441$ keV, or, in one case [33], calculated the energy thickness based on measured amounts of certain selected contaminants.

The use of the resonance in ^{7}Be(p,γ)^{8}B has the advantage of directly measuring the energy thickness of protons interacting with ^{7}Be in the target. The resulting resonance profile is a convolution of the resonance width, the accelerator energy resolution, and the energy thickness of the target. This method suffers insensitivity due to the large resonance width.

Using the ^{7}Li(p,γ)^{8}Be resonance improves upon this situation since this resonance width is narrower. However, the measured thickness is no longer that of ^{7}Be, but rather of ^{7}Li. It is often assumed that the ^{7}Li is due to the radioactive decay of ^{7}Be and therefore has the same distribution within the target as the ^{7}Be. Our measurements showed a lack of reproducibility of profiles measured in this fashion. The most significant effect is probably from Li diffusion, as mentioned in Section 3.3. Beam heating or other factors relevant to the environment of the target can also affect the diffusion. A further complication is the changing amount of ^{7}Li in a target. When the target is young the fractional increase in the amount of ^{7}Li in the target per hour can be quite large, and this can skew the shape of a resonance curve by artificially increasing the yield of points measured at a later time.

We avoided these problems by using the ^{7}Be$(\alpha,\gamma)^{11}$C reaction for the energy loss determination. This reaction has a strong resonance near $E_\alpha \approx 1380$ keV that is so narrow ($\Gamma << 1$ keV) that it may be approximated as a δ-function. This means that any measured resonance profile is simply the product of the actual target energy thickness and the experimental energy resolution. The only disadvantage to this technique is the necessity of converting the target profile for α-particles at $E_\alpha \sim 1380$ keV into a target profile for protons at various energies.

3.4.1 Measurement Technique and Analysis

For the BE1 experiment the ^{7}Be$(\alpha,\gamma)^{11}$C resonance profiles were measured in the middle and at the end of the ^{7}Be(p,γ)^{8}B measurements. We did not measure the resonance profile at the beginning due to fear that the alpha beam might cause significant sputtering of target material. It turned out that our (α,γ) experiments did not cause large sputtering losses. For the BE3 experiment we measured ^{7}Be$(\alpha,\gamma)^{11}$C resonance profiles before, in the middle of, and after our ^{7}Be(p,γ)^{8}B measurements.

The resonance yield was measured by detecting resonant γ-rays from the ^{7}Be$(\alpha,\gamma)^{11}$C reaction in the large NaI spectrometer (see Section 2.3.4). A 0.3 MeV-wide gate centered on the 8.4 MeV γ-ray full energy peak was used to determine the yield. Corrections were necessary for both beam-on and beam-off backgrounds.

Beam-off background was determined with the target left in the bombardment position close to the detector, to properly account for effects from the very high flux of 478 keV γ-rays coming from the decay of ^{7}Be. The number of counts within the gate was scaled by the length of measurement at each energy during the resonance measurements and subtracted from the raw yield.

Subtraction of the beam on background was more involved. In our first ^{7}Be$(\alpha,\gamma)^{11}$C measurements we observed a small beam-related background. Beam-on background measurements away from the resonance in ^{7}Be$(\alpha,\gamma)^{11}$C showed spectra consistent with γs from $^{9}Be(\alpha,n\gamma)^{12}C$. In particular, we saw 2.1 and 4.4 MeV γs from neutron capture on iodine in the NaI crystal.

Even small contaminant levels of ^{9}Be result in significant backgrounds due to the fact that the ^{9}Be(α,n γ)^{12}C cross-section is much larger than the ^{7}Be$(\alpha,\gamma)^{11}$C cross-section. In the BE1 experiment we did not have an in house measurement of ^{9}Be(α,n γ)^{12}C, so we used a simple scaling procedure.

First, the beam off background was subtracted from the data. We then chose a measurement energy well above the resonance energy for which the resonance yield was negligible. We then assumed that the yield in the counting gate at this energy was due to background. This beam-on background yield was then scaled by the following technique and subtracted from measurements at each energy.

A second gate was defined in each spectrum whose yield was due to the capture of neutrons in the NaI and which did not overlap with the full energy peak of the γ-rays from the ^{7}Be$(\alpha,\gamma)^{11}$C reaction. We then scaled the beam-on background yield

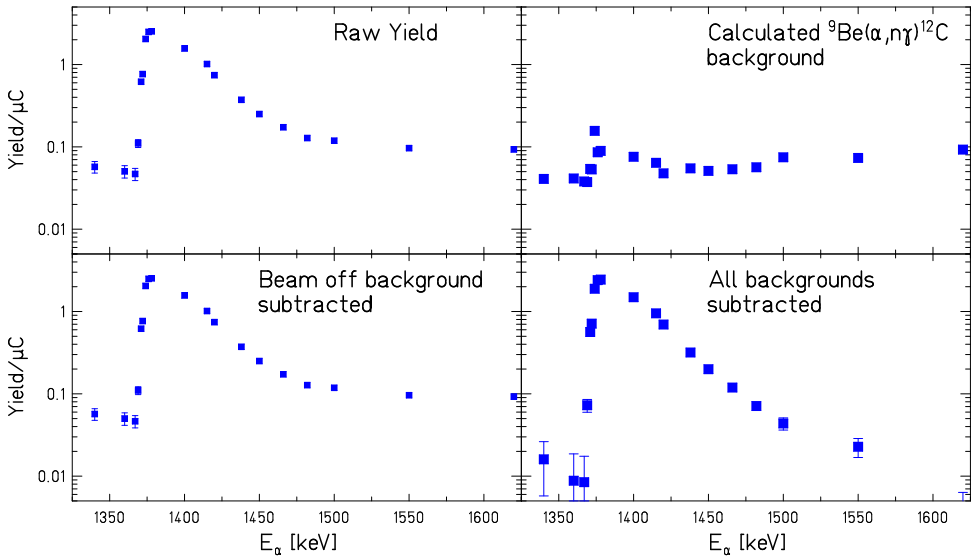

Figure 3.8: ^{7}Be$(\alpha,\gamma)^{11}$C resonance profiles for BE1. Top left: raw profile. Top right: Calculated ^{9}Be(α,n γ)^{12}C background vs. Energy (see Section 3.4.1). Bottom left: beam off background subtracted. Bottom right: All backgrounds subtracted. Note: Plotted against the nominal Eα which differs from the final calibration.

by the ratio of the yield in the neutron-capture gate from the measurement and the background data runs. Thus, the final yield is given by:

$$Y_{final} = Y_{raw} - Y_{beamoff} - \frac{Y_{bgnd}}{Y_{bgndref}} * Y_{ref}, \tag{3.9}$$

where Y_{final} is resonance yield, Y_{raw} is the measured yield, $Y_{beamoff}$ is the yield in the counting gate in the beam off measurement, Y_{bgnd} is the yield in the second gate, $Y_{bgndref}$ is the yield in this second gate in the reference spectrum, and Y_{ref} is the yield in the counting gate in the reference spectrum.

The beam on background subtraction method for the BE3 experiment was much simplified. We measured the energy dependence of the ^{9}Be(α,n γ)^{12}C background

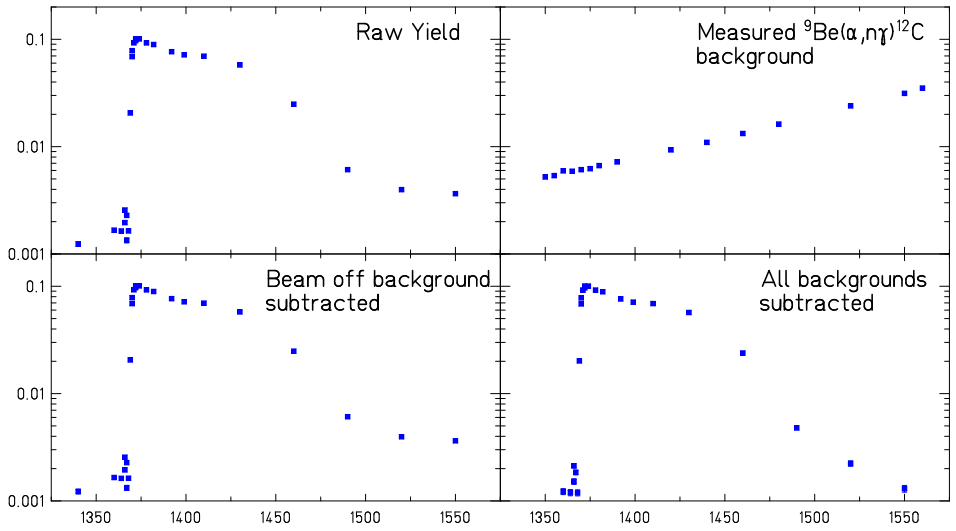

Figure 3.9: ^{7}Be$(\alpha,\gamma)^{11}$C resonance profiles for BE3. Top left: raw profile. Top right: Measured ^{9}Be(α,n γ)^{12}C background vs. Energy. Bottom left: beam off background subtracted. Bottom right: All backgrounds subtracted. Error bars are smaller than the data points. Note that the target used to measure the ^{9}Be(α,n γ)^{12}C background had significantly more ^{9}Be than the BE3 target. Note: Plotted against the nominal Eα which differs from the final calibration.

by using a ^{9}Be target in the same experimental set up used for our ^{7}Be$(\alpha,\gamma)^{11}$C measurement. As before, we chose a high energy data point where there was no evidence of neutrons from ^{9}Be(α,nγ)^{12}C, on each resonance curve to act as a reference point. Assuming that the yield of ^{7}Be$(\alpha,\gamma)^{11}$C had completely disappeared at that point, we associated the yield at that energy, after beam of background subtraction, with the beam on background. We then took the entire measured ^{9}Be(α,n γ)^{12}C yield vs. energy curve and scaled it by $\frac{Yield(referencepoint)}{Yield(backgroundcurve)}$ at the same energy. You can see the results in Figure 3.9.

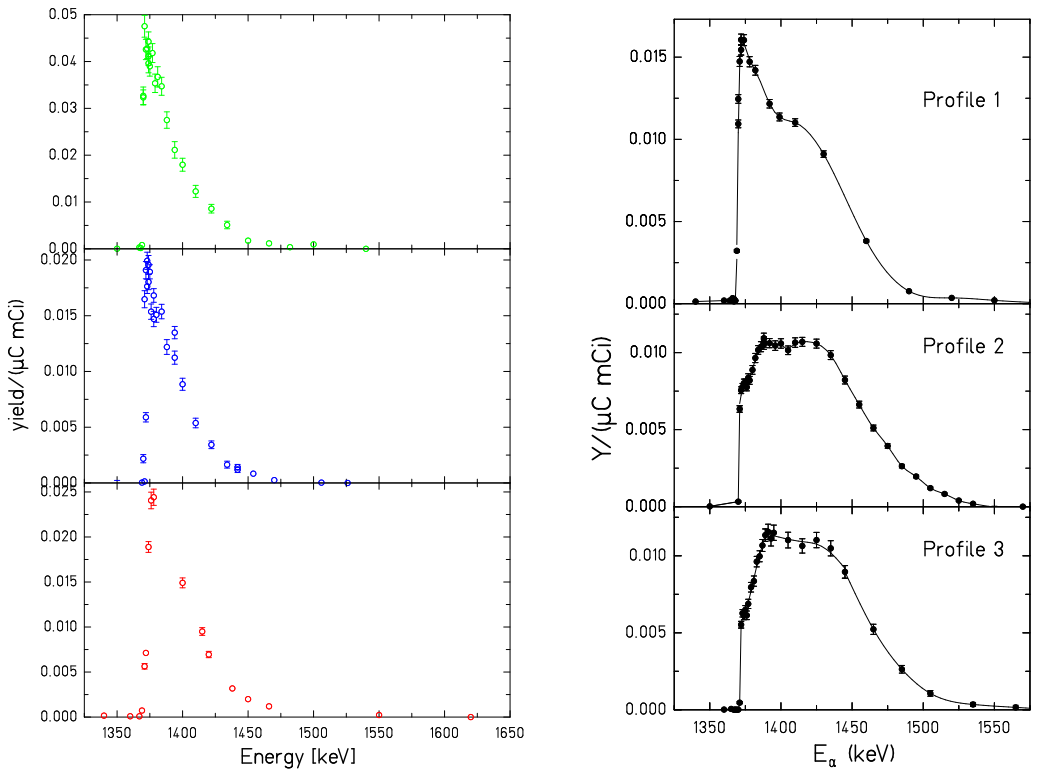

Figure 3.10: ^{7}Be$(\alpha,\gamma)^{11}$C resonance profiles. Left: BE1 Right: BE3 Note: Plotted against the nominal Eα which differs from the final calibration.

3.4.2 Results

We found the energy of the ^{7}Be$(\alpha,\gamma)^{11}$C resonance to be located at 1378 ± 3 keV, in good agreement with the previously determined value of 1376 ± 3 keV from Hardie, et. al. [34]. The energy loss (FWHM) of the α-beam in the BE1 target was 26 ± 2 keV, based upon the mean of the three measurements shown in the left panel of Figure 3.10. The small error was due in part to the excellent reproducibility of the three measurements. This reproducibility included the resonance energy, which had a $\Delta E_\alpha = 1 \pm 3$ keV, indicating negligible buildup of contaminants (most likely carbon)

on the surface, as well as a lack of target damage due to the bombardment.

The measurements of the BE3 target showed this same reproducibility in the energy of the resonance, indicating that again there was negligible buildup of contaminants on the surface of the target. This is particularly important, as the three profiles indicate very clearly that there was target damage which occurred between the measuring of profile 1 and 2, which were taken at the beginning and in the middle of the ^{7}Be(p,γ)^{8}B measurements, respectively (see the right panel of Figure 3.10). Luckily, the cause of the damage to the target was self evident. In between the measurement of these profiles the target was exposed to the full proton beam with a small raster amplitude.

For the BE3 experiment the measured profiles were converted into energy loss distributions for the proton beam using the ratios of the energy loss between alphas and protons in the target, dE_{α}/dx and dE_{p}/dx respectively. These energy loss functions depend upon target composition, and so it was important to know the contaminants present in the target.

The observed profile widths allowed us to determine the energy thickness of the targets. Measuring ^{7}Be activity, determines the amount of ^{7}Be present in the target, and therefore the energy thickness due to ^{7}Be. Use of these two measurements allowed us to determine the absolute energy loss of the alpha beam due to the contaminants. It was important to characterize the contaminants to convert to a proton energy loss function accurately.

Because of the way that the targets were fabricated, it is reasonable to expect contaminants with atomic masses up to and including that of Mo. Analysis of the ^{8}B backscattering measurements indicated that the contaminants were mostly Mo, or materials with a similar Z (see Section 3.8). Assuming that Mo is the only contaminant and using the resonance profiles along with the backscattering information

we determined a ^{7}Be:Mo target stoichiometry of 42:58 for BE1 and 63:37 for BE3 by mass. This indicates that our targets were much purer than those used in any other experiment to date.

Our analysis ignores straggling in the conversion from dE_α/dx to dE_p/dx. Straggling could be significant in the high energy tail of the energy loss profile, but our analysis indicates that our measured profiles fall off too slowly, by a factor of ten, to be due to straggling. The slow fall off of our resonance profiles is thus due primarily to target nonuniformity.

Knowing the energy thickness of the target, an energy averaged quantity $\langle f(E_p)\rangle$ is computed using the relation:

$$\langle f(E_p)\rangle = \frac{\int f(E_p)P(E_p)dE_p}{\int P(E_p)dE_p}. \tag{3.10}$$

where $f(E_p)$ is either E_p or $\sigma(E_p)$ and $P(E_p)$ is the target energy loss profile. Energy-averaging calculations are discussed further in Sec. 4.2.

3.5 Accelerator Energy Calibration

The energy, or more properly the momentum, of the beam used in these experiments was determined by a 90 degree horizontal analyzing magnet, in conjunction with horizontal slits in the beam line. In this set up, or any setup using a magnetic field to determine beam energy, the relativistic relation for beam energy, E_i, of an accelerated ion allowed through the magnet becomes:

$$E_i = \frac{kq^2f^2}{1 + E_i/2m_ic^2}, \tag{3.11}$$

where f is the magnet nuclear magnetic resonance frequency, m_i is the mass of the ion, c is the speed of light, q is the ion charge, and k is the magnet calibration constant which depends on factors such as geometry and accelerator construction. To know

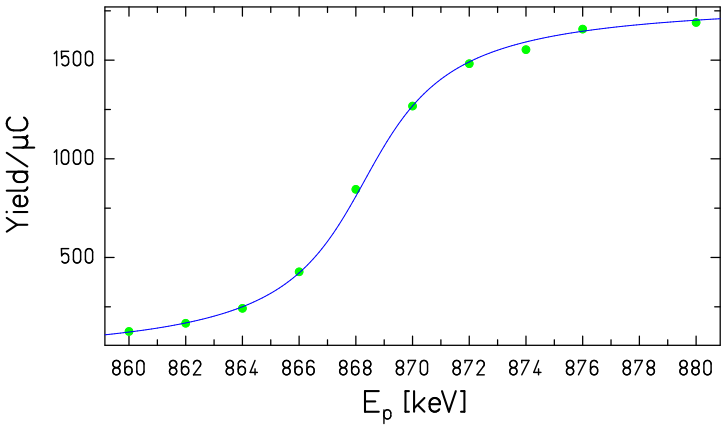

Figure 3.11: A thick target ^{19}F(p,$\alpha\gamma$)^{16}O resonance curve used in the accelerator energy calibration. The points are experimental data, and the curve is the fit used to determine the energy calibration.

precisely the energy at which any measurements were made, k must be determined precisely.

The accelerator energy calibration for the BE1 experiment was determined by measuring resonances in ^{19}F(p,$\alpha\gamma$)^{16}O located at 340.46 $\pm$ 0.04, 483.91 $\pm$ 0.10, and 872.11 $\pm$ 0.20 keV [61]. They were measured using a thick LiF target. Each resonance curve was measured three times. Twice the conditions were replicated carefully in the same manner as was used during the ^{7}Be(p,γ)^{8}B measurements, and the last time the beam transport parameters of the accelerator were purposefully changed drastically to determine what effect different beam "tunes" could have on the energy calibration.

In the BE3 experiment we remeasured these same resonances. In addition we measured the ^{19}F(p,$\alpha\gamma$)^{16}O at E$_p$=223.99$\pm$0.07 keV and utilized the information from our measurement of the ^{7}Be$(\alpha,\gamma)^{11}$C to provide a data point at high momentum. Taking the ^{7}Be$(\alpha,\gamma)^{11}$C resonance to be located at E=1377$\pm$2 keV, from the mean

of our resonance energy determination in the BE1 experiment and the determination give in Ref. [34] provided a data point at an equivalent proton energy of 5471 keV by comparing the magnetic rigidity of a singly charged alpha particle with a proton.

The thick target resonance curves were fitted with the integral of a Lorentzian resonance shape folded with a Gaussian beam energy resolution using the PAW software package. The magnet constant, k, was determined from each resonance profile using the fitted resonance location to determine the magnet NMR frequency at the known resonance energy. No systematic effect was found for the runs in which the beam tune had been purposefully varied from that used in cross-section measurements.

This series of k values was then fit to determine the overall accelerator calibration. For the BE1 experiment, with the spiral-inclined field tube in the accelerator (see Section 2.2.1), the k values were fit by a constant, and the value was determined to be 25.681±0.038. For the BE3 experiment the accelerator configuration had been changed significantly. For this experiment the k value determined at low energies from the ^{19}F(p,$\alpha\gamma$)^{16}O showed a small slope, while the value at large energies extrapolated from the ^{7}Be$(\alpha,\gamma)^{11}$C measurement indicated a more constant value at large energies.

We fit the data several ways to check for consistency between methods. Fitting the low energy data separately with a straight line and the highest three points with a constant yielded the same result as fitting with a smooth spline except in a narrow region around E_p ∼750 keV where no measurements where taken in the BE3 experiment. The accelerator calibration constant, k, is show in Figure 3.12.

3.6 Activity Determination

The ^{7}Be activity provides a direct method of determining the number of target atoms, N, provided the half-life of ^{7}Be is also known. The ^{7}Be activity was measured *in situ* with a collimated 50% efficient Ge detector located 27 cm from the target by detecting

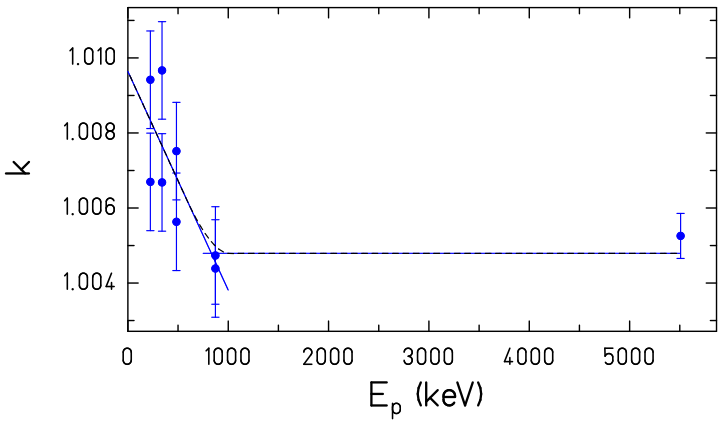

Figure 3.12: Points: data points taken from resonance measurements. Dashed curve: spline fit to all data points. Solid lines: piece-wise fit with straight lines, as detailed in this section.

the 478 keV γ-rays from the decay of ^{7}Be. The collimator shielded the detector from ^{7}Be sputtered from the target and located anywhere except on the target end of the rotating arm. Measurements to quantify the effectiveness of the collimator showed that sputtered ^{7}Be which deposited elsewhere in the target chamber contributed less than 0.2% of the total counting rate when the ^{7}Be target activity was being measured. An absorber was placed in the opening of the collimator and between the ^{7}Be target and the detector to limit the counting rate to 1.5 kHz or less.

In both the BE1 and BE3 experiments an absolute calibration of the efficiency, ϵ_{478}, was made with NIST traceable calibration γ-sources. In the BE1 experiment we fit 14 lines in the range of 276-835 keV from ^{125}Sb, ^{134}Cs, ^{133}Ba, ^{137}Cs, and ^{54}Mn sources. In each case we used the SATAN analysis package from GSI [56] to determine the area of the photopeak of each gamma line. These Isotope Products sources were calibrated to a typical precision of $\sigma = \pm 0.8\%$.

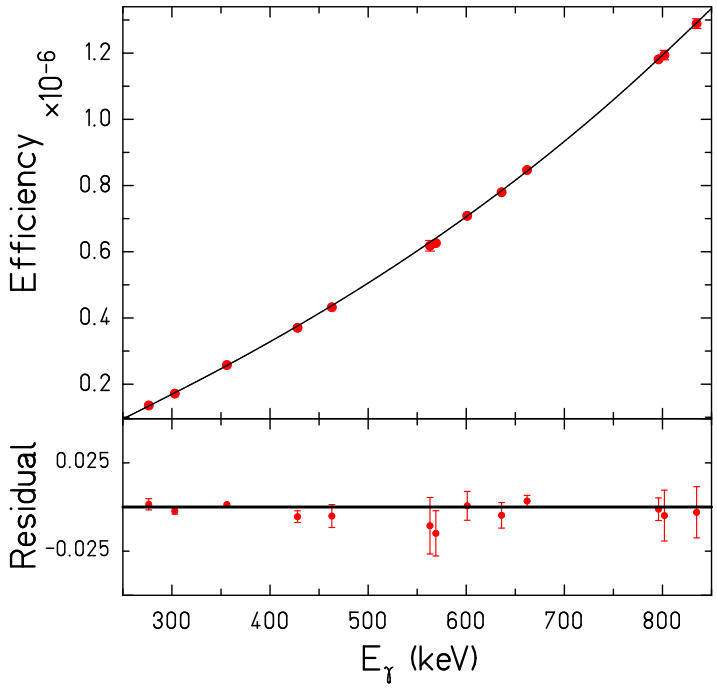

Figure 3.13: Top panel: *in situ* calibration of the Ge detector for the BE3 experiment. The curve is a third order polynomial fit to the points. The efficiency increases with energy due to the presence of the absorber. Bottom panel: residuals of the fit.

We acquired a second ^{137}Cs source with an independent calibration from CEA [16] and an accuracy of $\pm 0.4\%$. These two sources agreed to $\sigma = 0.4 \pm 0.8\%$, providing an independent check on source metrology.

For the BE3 experiment we excluded the 662 keV calibration line from ^{137}Cs, which we used in BE1, due to the fact that it was systematically high in all fits by 0.8%. This led us to question the calibration of this particular source. Excluding the source from the detector efficiency calculations made a negligible change in the calibration, so this discrepancy was not a significant source of uncertainty to the BE1 experiment.

We measured the activity *in situ* frequently during the course of the experiment. As can be seen in Figure 3.14 there were losses due to sputtering at the level of ≈15 mCi, which is 7% of our mean target activity. This level of sputtering must be properly accounted for to make a precision measurement. Otherwise both the absolute cross section normalization and energy dependence would be incorrect.

For both the BE1 and BE3 measurements we also measured, at a later date, the target activity in a "far" geometry without an absorber. These measurements were made using the same Ge detector, a Pb collimator with a 1.6 cm diameter aperture, and a source distance of about 200 cm. The efficiency of the detector was calibrated using the same sources as previously. For the BE3 target this occured about two months after the end of cross-section measurements. Using the 53.12 day half-life, this measurement indicated a 1.5±1.5% higher activity than that determined *in situ*. Since these two measurements agreed to within errors we used the average of the two calibrations for our absolute target activity determination. We also measured the BE1 target activity in this setup, approximately 20 months after the cross section measurements. Assuming a 53.12 day half-life resulted in an activity which differed from the earlier activity determination (corrected for decay time and for sputtering losses) by (0.3±1.9)%.

There has been some evidence that the half-life of ^{7}Be might depend upon host material [46, 49, 53, 54]. We compared target activity measurements with a projection based on initial activity and a 53.31 day half-life (see entry for Au in Table 1. of [49]). Measured activity differed from the activity predicted by (2.7±1.6)%. This is suggestive that the 53.12 day half-life is correct for our use, but not completely conclusive, and so we assigned a 0.4% uncertainty to our determination of $N_{Be}(t)$ for BE3 to cover the current disparity in ^{7}Be half-life measurements.

We determined $N_{Be}(t)$ from:

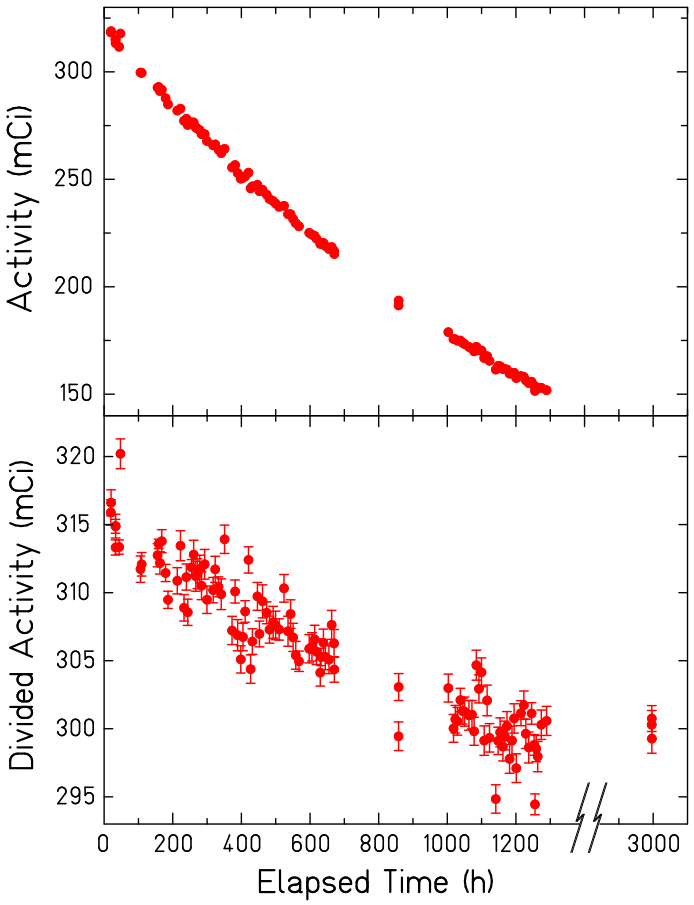

Figure 3.14: Top panel: BE3 target activity vs. time from the beginning of ^{7}Be(p,γ)^{8}B measurements. Bottom panel: The same data with the natural decay factor $e^{-\lambda t}$ divided out, where λ is the mean life determined from the 53.12 day half-life of ^{7}Be. Note that activity at large times ($\sim$3000 hrs) no longer shows any deviation from natural decay, indicating that once the experiment was finished (at $\sim$1700 hrs) there was no further loss of target material due to other processes. It also indicates that the 53.12 day half-life is correct within the accuracy of these measurements.

$$N_{Be}(t) = (3.7 * 10^{10})\mathcal{A}t_{1/2}/ln2 \tag{3.12}$$

where the activity $\mathcal{A} = N_\gamma/(3.7\text{x}10^{10}\epsilon_{478}\mathcal{BR})$ is given in Curies, and $\mathcal{BR}$ is the branching ratio for the 478 keV γ-decay (see Section 1.3).

3.7 Analysis of α spectra from $^7B(p,\gamma)^8B$

As discussed in Section 1.3, the first excited state of ^{8}Be is broad, and gives rise to a continuum of α-particle break up energies. As can be seen in Figure 3.7, the α-spectrum is obscured by background at low energies due to electronic noise at the lowest energies, and pileup of Compton electrons produced in the detector by the intense flux of 478 keV γ-rays from the target at somewhat higher energies. Reducing the Compton background motivated the additional measurements we made using the thinner S-detector for the BE3 measurement.

The gain and zero must be determined accurately when integrating a spectrum with an experimental cut off. A ^{148}Gd α source was used to monitor the gain of the detector at frequent intervals, and a precision pulser was used to monitor the zero offset of the energy scale. In the BE3 experiment the gain was found to be stable to $\pm$0.2% and the zero to $\pm$3 keV. In the BE1 experiment the gain and zero were stable to 0.2% and $\pm$2 keV, respectively.

A software threshold was set for each measurement that was above the experimental threshold and the α spectra was summed above that energy. The threshold had to be raised to be unambiguously above the noise for the lowest two energies for the BE3 (L) measurements because of the larger background, shown in Table 3.3.

Long measurements (>20 hours) were made to determine the beam-off background counting rate in the Si-detectors. In the BE1 experiment this rate was 1.2$\pm$0.1 counts/hour. A large fraction of this rate was due to naturally occurring

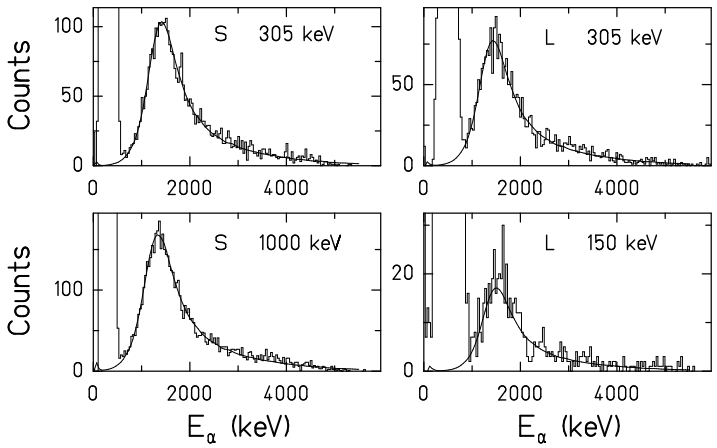

Figure 3.15: Representative alpha spectra measured with the BE3 target and the S and L detectors at different proton energies, as indicated. The lower background in the thinner S-detector is apparent. The curves are fitted TRIM calculations as described in this section.

Table 3.3: A table of experimental thresholds for the different ^{7}Be(p,γ)^{8}B cross section measurements.

Experiment(detector)	$\bar{E}_{\mathrm{c.m.}}$ (keV)	Threshold (keV)
BE1	186-1203	895
BE3(L)	116-140	930
BE3(L)	187-871	900
BE3(S)	184-1754	650

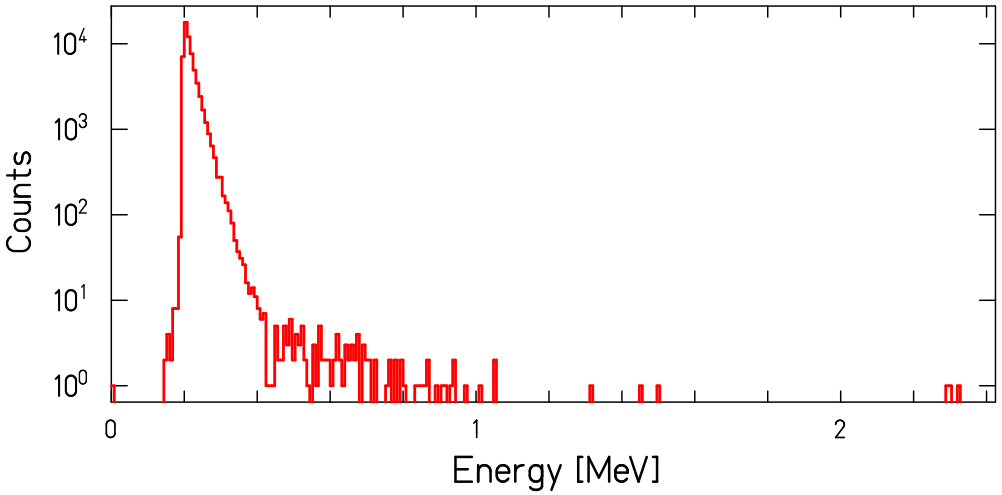

Figure 3.16: Beam off background for the BE3 measurement in the L detector.

α-radioactivity in the Al walls of the vacuum chamber and ^{210}Po, which is part of the ^{222}Ra decay chain, on the surface of the chamber walls. For the BE3 experiment we inserted a stainless steel shield between the detector and the chamber wall. This reduced the background to 0.6±0.1 counts/hour, averaged between the S and L detectors. A significant fraction of these background counts were concentrated in a peak around 5.3 MeV, due to α-decay of

We performed several tests to determine the beam-on background rate at several beam energies and found it to be negligible. This was due in part to the Al shields on the arm and in the chamber which prevented beam particles from multiply-scattering into the α-detectors.

The ^{7}Li(d,p)^{8}Li reaction has a much larger cross section than the ^{7}Be(p,γ)^{8}B and ^{8}Li β-decays to the same ^{8}Be excited state as ^{8}B. Because ^{7}Be decays naturally to ^{7}Li there is always ^{7}Li in the target. This means that even a small contamination of

deuterons can create a significant background with a similar spectral shape as that of ^{7}Be(p,γ)^{8}B. We made separate measurements with a LiF target to ensure that there was no appreciable deuteron contamination in the beam. After subtracting beam-off background, a 770 keV proton beam produced 1 count in 3.3 hours on the LiF target. Irradiating the BE1 target for 1.2 hours yielded 1565 counts. The LiF target had a much greater ^{7}Li areal density than any of the ^{7}Be targets used. This puts an upper limit of 0.03% background due to deuteron contamination of the beam at 770 keV. Because 770 keV is on a resonance for ^{7}Li(d,p)^{8}Li this limit is stronger for lower energies.

The total yield was computed by integrating the data above threshold, as described above, and multiplying by the factor $F_\alpha(E_p)$ which corrects for the fraction of the spectrum which lies below the experimental threshold. We computed $F_\alpha(E_p)$ using the TRIM Monte Carlo code [66] to calculate 'theoretical' α-spectra. This was a multi-step process in which TRIM was used to calculate a distribution of implantation depths in the target for the ^{8}B ions produced in the ^{7}Be(p,γ)^{8}B reaction. We then used the thin-target α-particle energy spectrum from [12] corrected (using TRIM) for the energy loss of the α-particles emerging from the target.

$$F_\alpha(E_p) = \frac{\Omega/2\pi}{\int_{th}^{\infty} N_\alpha(E_\alpha) dE_\alpha / N_{tot}}, \tag{3.13}$$

where Ω is the geometrical detector solid angle, $\int_{th}^{\infty} N_\alpha(E_\alpha) dE_\alpha$ is the integral of all MC events above the detector threshold, and N_{tot} is the total number of MC events.

We compared calculations for two different cases: 1) the opening angle of the emitted α-particles was restricted to the geometrical acceptance of the detector, and 2) the α-particles were emitted into 2π. In the second case large-angle multiple scattering sometimes produced α-particles within the acceptance of the detector; however these events were found only at low energies, $E_\alpha \leq$200 keV, below our experimental

threshold. The $F_\alpha(E_p)$ calculated by these two methods agreed to within the Monte Carlo precision of $\pm 0.2\%$.

The S-detector spectra were fit with a fixed energy calibration, excepting the highest point at $\bar{E}_{\mathrm{c.m.}} = 1754$ keV. The normalization of the calculated α-spectra was fit to the data to yield the total number of counts. For the $\bar{E}_{\mathrm{c.m.}} = 1754$ keV point and for most of the L-detector data we had to vary the zero offset to fit the spectra. The resulting offsets were as large as 88 keV and were typically 20-30 keV. These values are larger than what we expected from β-α summing; 1-2 keV. We were unable to reproduce the spectral shapes without this fitted offset, suggesting a limitation in the TRIM calculation.

We encountered similar difficulties when fitting ^{7}Li(d,p)^{8}Li α-spectra in the BE1 experiment. As a result, we conservatively assigned a larger uncertainty of $\pm 30\%$ to the correction $F_\alpha(E_p)$-1. The values of $F_\alpha(E_p)$ are listed in Table 3.4.

3.8 Backscattering Measurements

If ^{8}B scattered out of the target its loss would result in a systematic error in the absolute cross section determination. We determined from TRIM calculations that proton backscattering followed by ^{8}B production is unimportant. Large angle ^{8}B scattering is much more likely to occur from high-Z atoms. Substantial backscattering losses can occur when a high-Z target backing is used or if there are high-Z contaminants in the target.

We measured ^{8}B backscattering in ^{7}Be(p,γ)^{8}B reaction by modifying our apparatus as shown in Figure 2.5. During the measurement the beam passed through the aperture in one of the catcher plates and struck the ^{7}Be target. Backscattered ^{8}Bs were caught on the catcher plate. The rotating arm then placed that catcher plate in front of the Si-detector for counting. The arm was constructed symmetrically.

Table 3.4: A table of $F_\alpha(E_p)$ by $\bar{E}_{\text{c.m.}}$ for the different ^{7}Be(p,γ)^{8}B cross section measurements.

$\bar{E}_{\text{c.m.}}$	$F_\alpha(E_p)$	$\bar{E}_{\text{c.m.}}$	$F_\alpha(E_p)$	$\bar{E}_{\text{c.m.}}$	$F_\alpha(E_p)$	$\bar{E}_{\text{c.m.}}$	$F_\alpha(E_p)$	$\bar{E}_{\text{c.m.}}$	$F_\alpha(E_p)$
BE3 S		BE3 L		BE1		BE1		BE1	
184.3	1.005	115.6	1.023	257.0	1.042	599.7	1.055	876.3	1.063
219.8	1.004	139.8	1.031	293.5	1.046	609.4	1.056	876.3	1.065
255.4	1.005	187.0	1.025	294.4	1.047	619.6	1.058	1002.3	1.069
277.5	1.006	255.3	1.032	328.2	1.049	633.3	1.058	1102.8	1.071
326.4	1.006	277.5	1.036	363.8	1.041	639.4	1.059	1203.2	1.044
361.9	1.006	326.4	1.035	408.1	1.039	649.2	1.059		
871.2	1.012	361.9	1.037	461.3	1.052	658.7	1.060		
999.5	1.013	871.4	1.054	496.7	1.053	679.1	1.060		
1099.8	1.014	BE 1		528.6	1.077	699.4	1.061		
1200.1	1.015	185.6	1.071	558.8	1.082	750.7	1.061		
1754.1	1.019	221.3	1.044	589.0	1.086	820.7	1.062		

While one catcher plate was in front of the detector the other was in front of the ^{7}Be target. The same arm rotation cycle was used as in the ^{7}Be(p,γ)^{8}B cross section measurements.

The efficiency for catching ^{8}B on the Cu catcher plates and counting the subsequent β-delayed α-particules in the Si detector was calculated using TRIM to estimate the angular distribution of the backscattered ^{8}B.

We made backscattering measurements at $\bar{E}_{\mathrm{c.m.}} = 626$ and 1200 keV. Figure 3.17 shows the measured backscattering probabilities for the BE1 and BE3 targets, along with TRIM calculations for several different assumed target compositions. For each case we assumed a uniform target made up of differing fractions of ^{7}Be, C, and Mo. The amount of ^{7}Be in the target was known from target activity measurements. The total energy thickness of the target is fixed by the ^{7}Be$(\alpha,\gamma)^{11}$C resonance profiles (see Section 3.4). We determined the amount of contaminants by determining the energy thickness for pure ^{7}Be from the target activity and assigning the remainder of the target energy thickness to C and Mo in varying ratios for the different test cases. We used C to represent low-Z contaminants and Mo as representative of high-Z contaminants. Because of the target manufacturing process (see Section 2.1) we didn't expect significant contaminants heavier than Mo.

The calculated curves are shown in Figure 3.17. For C contaminants the ^{8}B backscattering takes place primarily from the Mo backing. Although the backscattering cross section is highest at low energy, the backscattered ions do not have enough energy to emerge from the target after backscattering off the backing and so the backscattering probability rises with bombarding energy, as shown in Figure 3.17 for the BE1 target.

Mo contaminants allow the ^{8}B ions to backscatter in the target layer itself, raising the backscattering probability and extending it to lower energies since the bombarding

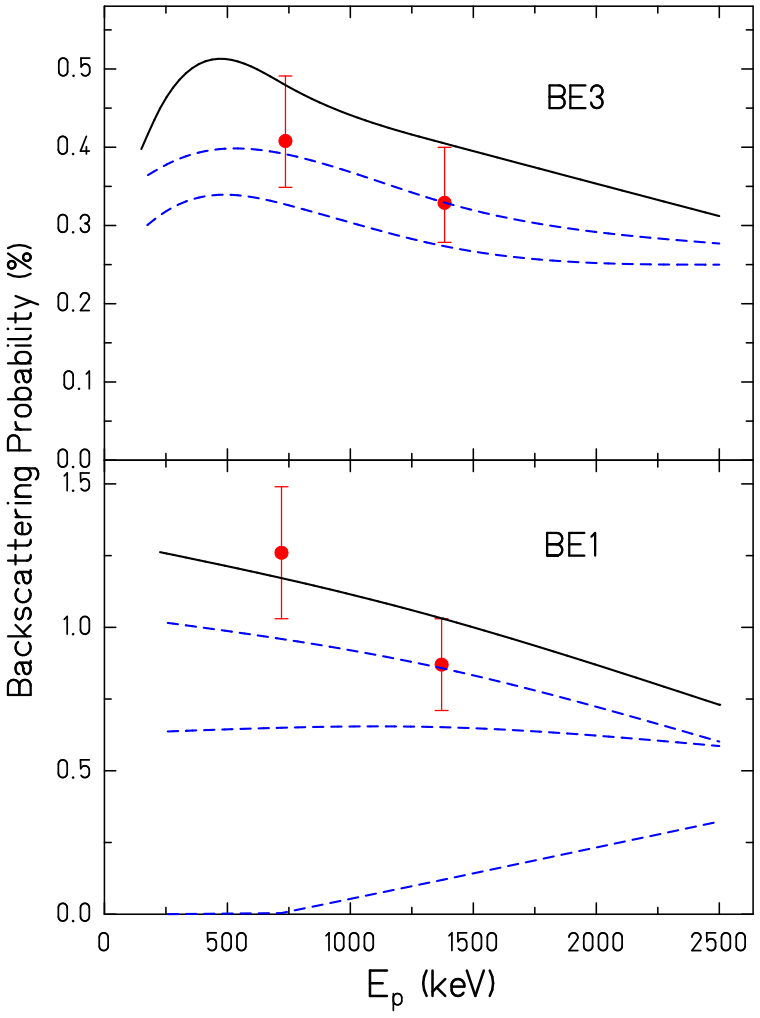

Figure 3.17: Measured backscatting probabilites (errors include statistics and systematics) and TRIM calculations. The ^{7}Be:C:Mo atom-number ratios assumed in the TRIM calculations are, in descending order: top panel - 63:0:37, 58:8:34, 57:13:30; bottom panel - 42:0:58, 38:19:43, 36:31:33 and 19:81:0. The backscattering curve for pure C contaminants for BE3 is not distinguishable from the horizontal axis.

ions need not penetrate as deeply. The backscattering probabilities for the BE3 target are lower than for the BE1 target because this target was thicker, which suppresses backscattering, particularly at low energies.

The best fit curves indicate approximate relative concentrations of ^{7}Be:C:Mo = 38:19:43 for BE1, and ^{7}Be:C:Mo = 58:8:34 for BE3. It is expected that these concentrations would be similar since the same process was used in the manufacture of both targets. It is also not surprising that BE3 is somewhat purer due to the larger amount of ^{7}Be used in the fabrication process. Examining Figure 3.17 it is apparent that the results are consistent with a pure Mo target, within errors.

Aside from composition, nonuniformity of the target can also affect backscattering probabilities. The lack of a flat "plateau" in the $^{7}\mathrm{Be}(\alpha,\gamma)^{11}\mathrm{C}$ resonance profiles of BE1 shows it to be significantly less uniform than BE3. The agreement between measured backscattering probabilities and the calculation shown in Figure 3.17, in which the targets were assumed to be uniform, suggests that nonuniformity did not play an important role.

Based on the small backscattering probabilities shown in Figure 3.17, we assigned constant backscattering corrections to our measured cross sections of 0.4±0.1% for BE3 and 1.0±0.5% for BE1.

Chapter 4

DATA AND ANALYSIS

4.1 History of the Experiment

The BE1 target was used to collect cross section data in January and February of 2001. Because this experiment has a large number of data points over a wide energy range, and because the target activity was monitored and corrected for sputtering losses during the measurement, as described in Section 3.6, this data set provides the most precise information on the energy dependence of the cross section from $\bar{E}_{\mathrm{c.m.}} = 185$ to 1203 keV. Progress and ideas which came about during our later (BE2 and BE3) experiments led to improvements in our overall systematics and procedure. Even so the BE1 measurement is invaluable as a complete and separate experiment, useful in cross-checking systematics. Results for the BE1 experiment were first reported in Ref [41] and updated in more detail together with the results of the BE3 experiment in Ref. [42].

The BE2 target was never used in a full experiment. Instead, during measurements with this target we realized the disadvantages of depending upon ^{7}Li in the target for determination of solid angles and the ^{7}Be spatial distribution in the target. This prompted us to use alternate methods for determining solid angle and target distribution in the following BE3 experiment.

A ^{148}Gd α-source was used to measure the solid angle as described in Section 3.3. We also created an apparatus which used a Ge detector and a collimated slit to scan the ^{7}Be activity and determine the ^{7}Be density profile of our targets, as described in Section 3.1.3 and in Ref. [68, 67].

The α-spectrum cutoff correction factors $F_\alpha(E_p)$ (see Table 3.4 and Section 3.7) for both ^{7}Be(p,γ)^{8}B and ^{7}Li(d,p)^{8}Li were large for the BE1 and BE2 measurements. This correction could not be measured, only calculated. A thinner Si-detector was procured which would have a smaller corrections (i.e. $F_\alpha(E_p)$ closer to unity) for the ^{7}Be(p,γ)^{8}B measurements in the BE3 experiment.

Accelerator measurements with the BE3 target were completed over nine weeks during the summer of 2002. Because of improvements, the most important noted above, together with the overall precision of this experiment our best result for $S_{17}(0)$ comes from the BE3 measurements, superseding the values reported previously in Ref. [41].

Cross sections were converted into S factors using the relation:

$$S_{17}(\bar{E}_{\rm c.m.}) = \sigma(\bar{E}_{\rm c.m.})\bar{E}_{\rm c.m.}e^{(E_G/\bar{E}_{\rm c.m.})^{1/2}} \tag{4.1}$$

which differs from Equation 1.1 by the replacement of $E_{c.m.}$ with $\bar{E}_{\rm c.m.}$ values, which were computed as described below. This procedure adjusts for energy averaging, so that fitting experimental $S_{17}(\bar{E}_{\rm c.m.})$ values without explicitly including energy averaging is equivalent to fitting the measured cross sections including energy averaging. In this way reported data can be used by others without requiring a detailed knowledge of the energy loss properties of the target used to make the measurements. The method of including this energy averaging is described below in Section 4.2. A slightly more involved technique was required for measurements near the $\bar{E}_{\rm c.m.}$=630 keV M1 resonance in ^{7}Be(p,γ)^{8}B, as described in Section 4.5.1.

4.2 $\bar{E}_{\rm c.m.}$ determination

Even in the idealized situation of an accelerator that produces a monoenergetic beam, reactions happen in a target at energies other than the incident beam energy. As the

beam passes through the target it loses energy causing reactions to happen at reduced energies. In order to account properly for this energy averaging the energy dependence for the cross section $\sigma(E_{c.m.})$ must be known. Specifically, it must be known at each bombardment energy at which the cross section measurements were made and over a range of the target's energy thickness to the projectile at each bombardment energy.

Knowing the energy dependence of the ^{7}Be(p,γ)^{8}B cross section over the target thickness, $\langle\sigma(E_{c.m.})\rangle$ may be computed using Equation 3.10, the ^{7}Be(α,γ)^{11}C target energy thickness profile (see Section 3.4), and a relation between dE_p/dx and dE_α/dx. Solving the equation $\langle\sigma(E_{c.m.})\rangle=\sigma(\bar{E}_{c.m.})$ for $\bar{E}_{c.m.}$ gives the effective energy, $\bar{E}_{c.m.}$, which would return the same cross section as the measured energy averaged cross section. Expressing the measured cross sections as functions of $\bar{E}_{c.m.}$ removes the effect of energy averaging so that the data may be examined and compared to theory and to other data without the need to refer to the target energy thickness profile. To convert from the E_α energy loss profile measured with ^{7}Be(α,γ)^{11}C to the energy loss profile relevant to ^{7}Be(p,γ)^{8}B cross section measurements we related the proton and alpha energy loss functions dE_p/dx and dE_α/dx using SRIM tables, assuming pure Mo contaminants in the ^{7}Be target, consistent with the backscattering data (see Section 3.8).

Because the S-factor changes very little over the energy thickness of the target for most of our measured data points it sufffices to use the above procedure with the energy dependence taken from Equation 4.1 with $S_{17}(E_{c.m.})$ set equal to a constant. Near the 1^+ resonance the cross section changes quickly enough that we used a more detailed procedure as described in Section 4.5.1.

It should be noted that $\bar{E}_{c.m.}$ and $\langle E_{c.m.}\rangle$, where $\langle E_{c.m.}\rangle$ is computed from Equation 3.10 and $\bar{E}_{c.m.}$ is computed as described above, differ significantly at the lowest energies measured in this experiment. For example, for the BE3 target at E_p=149.9

keV the corresponding energies $\langle E_{c.m.} \rangle$=113.9 keV and $\bar{E}_{c.m.}$=115.6 keV yield an S_{17} which differs by 6%.

4.3 BE1 and BE2 Results

Results for the BE1 experiment were reported in Reference [41]. Figure 4.1 and Table 4.2 show these results normalized to our best value for $S_{17}(0)$, as given by Equation 4.2, using data below $\bar{E}_{c.m.}$=400 keV from the BE3 measurement. The error bars on the BE1 data have been increased relative to those reported in [41] because of an increase in the uncertainty of $F_\alpha(E_p)$ as discussed in Section 3.7. Even with these changes it is important to note that our published values for $S_{17}(0)$, 22.3±0.7 (exp) [41] and Equation 4.2 [42], are all in excellent agreement.

In the BE2 experiment data were taken in a close geometry with the L detector, over the range $\bar{E}_{\mathrm{c.m.}}$=876-2459 keV. The BE2 data have relatively large systematic errors due to the large threshold correction factors $F_\alpha(E_p)$ for these data, which ranged from 1.091 to 1.287, and the corresponding ±30% uncertainty on $F_\alpha(E_p)$ - 1 (see Section 3.7).

4.4 BE3 Results

Data taken at low $\bar{E}_{\mathrm{c.m.}}$ is the most useful for extrapolating to zero energy, so most of the data points from the BE3 measurement were measured below the M1 resonance at $\bar{E}_{\mathrm{c.m.}}$=630 keV. Data was also taken above the resonance. It allowed us to normalize the BE2 data, and provided a check of the absolute normalization in comparison with the BE1 data in a region where energy averaging and other systematics are small. Figure 4.2 shows the data from the BE3 experiment, with experimental uncertainties in our determination of $S_{17}(\bar{E}_{\mathrm{c.m.}})$, as listed in Table 4.1. Nineteen data points taken with two detectors, along with a theoretical extrapolation described in

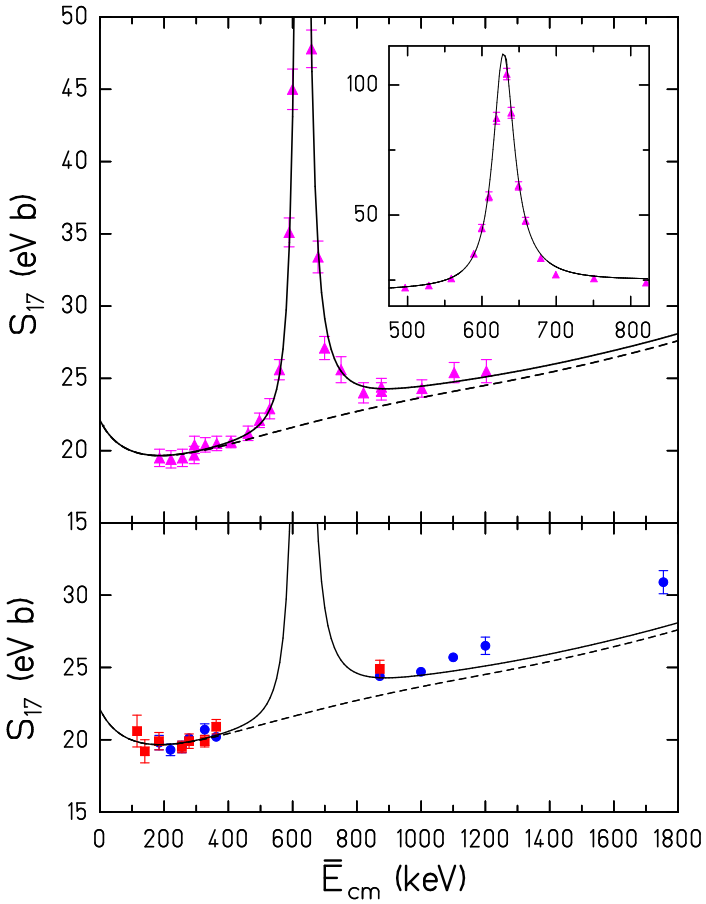

Figure 4.1: Top panel: BE1 data normalized to $S_{17}(0) = 22.2$ eV b. Solid curve: best-fit DB plus a fitted 1^+ resonance; dashed curve - DB only (see text). Inset: resonance region. Bottom panel: solid circles - BE3 S data; solid squares - BE3 L data. The solid curve was calculated with 1^+ resonance parameters determined from fits to the BE1 data, and the normalization was determined by fitting the BE3 data with $\bar{E}_{\rm c.m.} \leq 362$ keV.

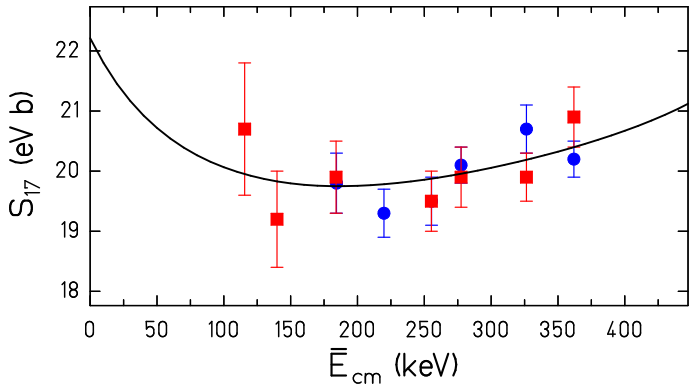

Figure 4.2: BE3 S-factor data measured below the resonance. Circles: BE3 S; Squares: BE3 L; Curve: best DB fit. Error bars include statistical and varying systematic errors.

the next section, provide our best determination of $S_{17}(0)$. Note that the data in Table 4.2 differs slightly from Table III of [42]. A revisiting of that data shows that two errors relating the energy thickness and carbon build up on the target were added in quadrature. Because these two errors are correlated a more careful approach is to add them linearly. This causes little change in the final $S_{17}(0)$.

4.4.1 Determination of $S_{17}(0)$

It is not possible to make direct measurements of S_{17} at the energies relevant to solar fusion. The cross section is so small at these energies that only in a massive body, such as the sun itself, is there an appreciable event rate. Experimental measurements must be made at higher energies where the cross section is significantly higher and then extrapolated downwards to the energies in question.

To minimize extrapolation error it is best to fit data as low in energy as possible, consistent with good experimental precision. Above the M1 resonance, at $\bar{E}_{c.m.}$=630

Table 4.1: Percent uncertainties in $S_{17}(\bar{E}_{\text{c.m.}})$ from the BE3 S and L data.

Statistical errors	1.3-4.0
Varying systematic errors:	
proton energy calibration	0.0-0.7
target thickness	0.0-2.2
target composition	0.0-0.7
α-spectrum cutoff	0.1-0.7 (S)
	1.0-1.8 (L)
Scale factor errors:	
beam-target inhomogeneity	1.0
integrated beam flux	0.9
^{7}Be target atom number	1.1
solid angle	1.5
backscattering	0.1
timing cycle	0.2
Total scale factor error	2.3

keV, different calculations of the ^{7}Be(p,γ)^{8}B cross section deviate from each other in substantial ways. Below the resonance the physics involved becomes easier to calculate as the reaction takes place predominantly through direct capture. As the energy becomes lower this capture becomes increasingly extra-nuclear and insensitive to nuclear structure making the calculation of the cross section less model dependent. For this reason our best determination of $S_{17}(0)$ is a fit to our data below the M1 resonance.

The ^{7}Be(p,γ)^{8}B calculation that fits experimental data the best over a wide energy range is the cluster model of Descouvemont [21] (DB). The curve in Figure 4.2 is a scaled DB theory fit to all of our BE3 data with $\bar{E}_{c.m.}$=116-362 keV. The DB theory shown there does not include contributions from either the 1^+ resonance near $\bar{E}_{c.m.}$=630 keV or the 3^+ resonance near $\bar{E}_{c.m.}$=2200 keV. At these low energies the 1^+ resonance contributes less than 0.4% to S_{17} at the highest energy we measured, and less at lower energies. The contributions from the 3^+ resonance are completely negligible. These resonance contributions are determined from our resonance fits discussed below in Sections 4.5.1 and 4.5.2.

From these fits we determine $S_{17}(0)$ to be 22.1±0.2 eV barns and 22.4±0.2 eV barns for the S and L detector data, respectively. These values agree well within the quoted errors, which include only statistical and relative systematic contributions. Our best value for $S_{17}(0)$ comes from a weighted average of these two results, including a common-mode scale factor uncertainty of 2.3%. From this we obtain:

$$S_{17}(0) = 22.2 \pm 0.6(\text{expt}) \text{ eV barns} , \tag{4.2}$$

where the error includes all contributions except the theoretical extrapolation error which will be discussed in Section 5.1.3. The BE3 data are given in Table 4.2, normalized to our best value for $S_{17}(0)$ as given by Equation 4.2.

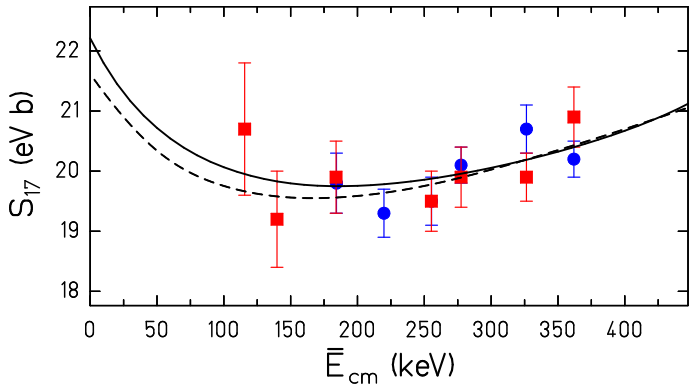

Figure 4.3: BE3 S-factor data measured below the resonance. Circles: BE3 S; Squares: BE3 L; Solid curve: best DB fit. Dashed curve: best D04 fit. Error bars include statistical and varying systematic errors.

4.4.2 Descouvement 2004

Descouvement published an updated version of the DB cluster model in 2004 (D04)[20], which is discussed in more detail in Chapter 5. Fitting our low energy data with this model yields an S-factor of:

$$S_{17}(0) = 21.6 \pm 0.6(\text{expt}) \text{ eV barns} , \tag{4.3}$$

which is commensurate with the theoretical error indicated in Section 5.1.3 and Equation 5.1. This value is not used outside of this section.

4.5 Resonance parameters

4.5.1 1^+ resonance

In the BE1 experiment data was taken over the range $\bar{E}_{\text{c.m.}}$=186-1200 keV. Detailed data over the $\bar{E}_{\text{c.m.}}$=630 keV M1 resonance were fit by adding an incoherent Breit-

Table 4.2: Our S_{17} data normalized to the best-fit BE3 results, and 1σ errors. $\sigma_{\rm stat}$ - statistical error, $\sigma_{\rm vary}$ - varying systematic error, all in eV b. Additional non common-mode uncertainties of 0.37% and 0.28% apply to each BE3 S and BE3 L data point, respectively. An additional common-mode error of 2.3% applies to all points.

$\bar{E}_{\rm c.m.}$	S_{17}	$\sigma_{\rm stat}$	$\sigma_{\rm vary}$	$\bar{E}_{\rm c.m.}$	S_{17}	$\sigma_{\rm stat}$	$\sigma_{\rm vary}$	$\bar{E}_{\rm c.m.}$	S_{17}	$\sigma_{\rm stat}$	$\sigma_{\rm vary}$
BE1				BE1				BE3 S			
185.6	19.5	0.5	0.4	679.1	33.4	0.9	0.6	184.3	19.8	0.4	0.3
221.3	19.4	0.5	0.3	699.4	27.1	0.6	0.5	219.8	19.3	0.4	0.2
257.0	19.5	0.5	0.3	750.7	25.6	0.7	0.5	255.4	19.5	0.3	0.2
293.5	19.7	0.5	0.3	820.7	24.0	0.5	0.5	277.5	20.1	0.3	0.1
294.4	20.4	0.5	0.3	876.3	24.4	0.2	0.5	326.4	20.7	0.4	0.1
328.2	20.4	0.4	0.3	876.3	24.1	0.4	0.5	361.9	20.2	0.3	0.1
363.8	20.5	0.4	0.3	1002.3	24.3	0.2	0.6	871.2	24.4	0.3	0.1
408.1	20.6	0.3	0.3	1102.8	25.4	0.3	0.6	999.5	24.7	0.3	0.1
461.3	21.2	0.4	0.3	1203.2	25.5	0.3	0.7	1099.8	25.7	0.3	0.1
496.7	22.1	0.3	0.4	BE 2				1200.1	26.5	0.6	0.1
528.6	22.9	0.6	0.4	875.7	24.5	0.2	0.5	1754.1	30.9	0.8	0.2
558.8	25.6	0.6	0.4	1001.6	24.5	0.2	0.5	BE3 L			
589.0	35.1	0.8	0.6	1403.6	27.4	0.4	0.6	115.6	20.7	0.8	0.7
599.7	45.0	1.1	0.8	1579.4	29.3	0.5	0.6	139.8	19.2	0.6	0.5
609.4	57.2	1.4	1.0	1931.0	34.8	0.6	0.8	184.0	19.9	0.5	0.3
619.6	87.2	1.6	1.6	2194.7	43.3	0.8	0.9	255.3	19.5	0.4	0.3
633.3	104.2	1.1	1.9	2458.5	40.6	0.7	0.9	277.5	19.9	0.4	0.3
639.4	89.3	1.3	1.6					326.4	19.9	0.3	0.2
649.2	61.2	1.2	1.1					361.9	20.9	0.4	0.3
658.7	47.8	0.9	0.9					871.4	24.9	0.4	0.4

Wigner resonance term to the nonresonant DB cross section used to fit data below the resonance:

$$\sigma(E_{\rm c.m.}) = C_1\sigma_{DB}(E_{\rm c.m.}) + \frac{C_2}{E_{\rm c.m.}}\frac{\Gamma_p(E_{\rm c.m.})\Gamma_\gamma(E_{\rm c.m.})}{(E_{\rm c.m.}-E_0)^2+\Gamma_p(E_{\rm c.m.})^2/4} \quad (4.4)$$

where $C_1 \approx 0.7$ is a fitted scaling factor, $\sigma_{DB}(E_{\rm c.m.})$ is the DB cross section (with the 1^+ resonance removed), $C_2 = 3\pi\lambda\!\!\!^{-2}E_{\rm c.m.}/8$, $\Gamma_p(E_{\rm c.m.}) = \Gamma_p(E_0)P_1(E_{\rm c.m.})/P_1(E_0)$, $P_1(E_{\rm c.m.})$ is the ℓ=1 Coulomb penetrability evaluated at R = 3.65 fm, $\Gamma_\gamma(E_{\rm c.m.}) = \Gamma_\gamma(E_0)(E_{\rm c.m.}+Q)^3/(E_0+Q)^3$ and $Q = 0.137$ MeV.

Energy averaged cross sections $\langle\sigma(\mathrm{E}_{c.m.})\rangle$ were computed at each bombarding energy using Equation 3.10 along with energy loss profiles taken from the ^{7}Be$(\alpha,\gamma)^{11}$C measurements. We computed $\bar{E}_{\rm c.m.}$ values for each bombarding energy as before (see Section 4.2) by solving the equation $\langle\sigma(\mathrm{E}_{c.m.})\rangle$=$\sigma(\bar{E}_{c.m.})$ for $\bar{E}_{c.m.}$. As with the low energy S_{17} data discussed in Section 4.2, $\bar{E}_{\rm c.m.}$ differs significantly from $\langle \mathrm{E}_{c.m.}\rangle$ near the resonance as it will wherever the cross section has a significant energy dependence over a range equal to the energy thickness of the target.

Measured cross sections were converted to $S_{17}(\bar{E}_{c.m.})$ using Equation 4.1. We checked that fitting our $S_{17}(\bar{E}_{c.m.})$ data (without explicit energy averaging) gives the same values and uncertainties for the S factor and for the resonance parameters as does the original fit to the cross section data including energy averaging.

Table 4.3 shows our center-of-mass 1^+ resonance fit parameters together with those of refs. [26, 10] and the elastic scattering results of ref. [7]. Descouvemont and Baye [21] predict the lowest 1^+ resonance at $\mathrm{E_{c.m.}} \sim 0.2$ MeV. Scaling by the experimentally measured energy, they calculate $\Gamma_p(E_0) \approx 59$ keV and $\Gamma_\gamma(E_0) = 33$ meV (assuming pure M1), in reasonable agreement with experiment.

Table 4.3: 1^+ resonance parameters

Parameter	Present work	Ref. [26]	Ref. [10]	Ref. [7]
E_0 (keV)	630 ± 3	632 ± 10	633	634 ± 4
$\Gamma_p(E_0)$ (keV)	35.7 ± 0.6	37 ± 5	35 ± 3	31 ± 4
$\Gamma_\gamma(E_0)$ (meV)	25.3 ± 1.2	25 ± 4	25 ± 2	-

4.5.2 3^+ resonance

Our data shows clear evidence for the lowest 3^+ at $\bar{E}_{c.m.}$ ∼2200 keV. The DB curve shown in Figure 4.1 does not include a contribution from this resonance, and deviations of the data from the plotted curve can be seen at the highest energies as a consequence. We fit our BE2 and BE3 data together, both normalized to Equation 4.2, with the nonresonant DB calculation plus contributions for the 1^+ and 3^+ resonances. The parameters for the 1^+ resonance were fixed to our results quoted in Table 4.3, and the 3^+ resonance was fitted with a form similar to that in Equation 4.5 with a few modifications. The constant C_2 was multiplied by the factor 7/3 to account for the angular momentum factor, 2J+1, in the resonance strength. This formula neglects f-wave capture, E2 decay, proton inelastic scattering to the first excited state of ^{7}Be, and the ^{4}He + ^{3}He + p channel.

The fit results are reported in Table 4.4. An unconstrained fit does a poor job of determining the resonance parameters because of the large error bars due to the uncertainty in $F_\alpha(E_p)$. The unconstrained values of E_0=2100±60, $\Gamma_p(E_0)$=510±270 kev, and $\Gamma_\gamma(E_0)$=180±70 meV agree well with the more precise values of E_0=2183±30 keV and $\Gamma_p(E_0)$=350±40 keV of [4].

We performed a second fit with the resonance energy and width constrained to the values of [4]. This fit yields a $\Gamma_\gamma(E_0)$=150±30 meV and is displayed in Figure

Table 4.4: 3^+ resonance parameters

Parameter	Constrained fit	Unconstrained fit
E_0 (keV)	2183[1]	2100 ± 60
$\Gamma_p(E_0)$ (keV)	350[1]	510 ± 270
$\Gamma_\gamma(E_0)$ (meV)	150 ± 30	180 ± 70

4.4. Descouvement and Baye [21] also calculated the properties of this 3^+ resonance, finding E_0 ∼2800 keV. After adjusting their resonance energy to agree with experiment and scaling the other parameters likewise their calculation yields $\Gamma_p(E_0)$=530 keV and $\Gamma_\gamma(E_0)$=45 meV.

From this analysis we find that the combination of fitted 1^+ and 3^+ resonances with the nonresonant contribution from the DB calculation describes the data reasonably well up to $\bar{E}_{c.m.}$ ∼2500 keV. Even so, the constrained fit indicates that the nonresonant DB contribution "underneath" the 3^+ resonance is not quite correct. Because the 3^+ resonance contributes ≤1% below 1500 keV we do not include it in calculations, figures, or discussion outside of this section.

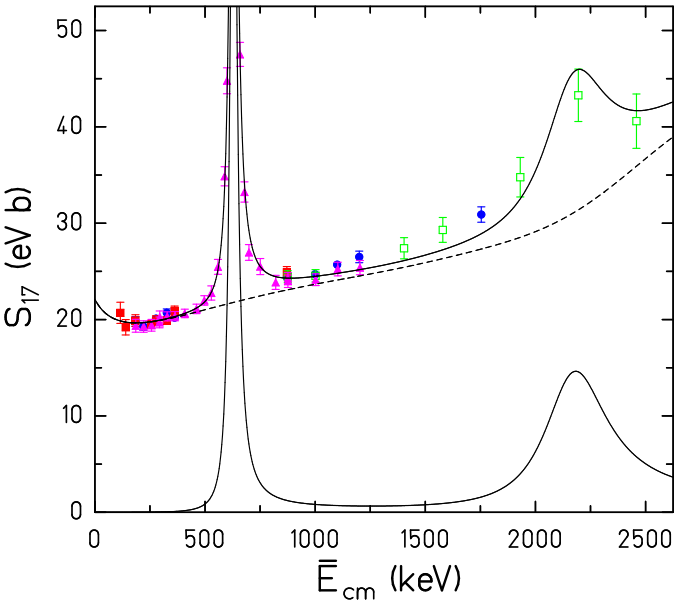

Figure 4.4: The BE2 data are shown as open squares, and the BE1 and BE3 data are shown with the same symbols as in Fig. 4.1 Solid curve: best-fit DB plus fitted 1^+ and 3^+ resonances; dashed curve: DB only; lower solid curve: 1^+ and 3^+ resonance contributions.

Chapter 5
DISCUSSION

5.1 Examination of Theory

Direct cross section measurements such as those presented in Chapter 4 require extrapolation from the region where data is taken to the energies of importance in the solar environment. This requires theoretical knowledge. Indirect measurements such as those discussed below often require even more involved theoretical knowledge. In all cases it is important to understand how certain the various features of different models are, to attempt to come up with a means of distinguishing between them, and choose the most reliable.

5.1.1 Prediction of Observables

In total, thirteen theories have been examined in the data analysis of this work. If all theories predicted known physical quantities equally well then there would be no reason to prefer one over another in the prediction of other unknown quantities, such as $S_{17}(0)$. There are many predictions which might be tested against experiment, including the energy dependence of $S_{17}(E)$, and the quadrupole moment of ^{7}Be.

In practice evaluating different theoretical models of ^{7}Be, in particular predictions of $S_{17}(E)$ and $S_{17}(0)$, is more difficult. Most theoretical models provide little if any information about experimentally observable values, other than the S(E). Jennings et. al. used a simple hard sphere model to set reasonable limits on other, more complicated, models [40]. From this analysis it becomes apparent that there are

certain features that are nearly model independent, including the upturn in the S-factor at low energies due to the pole in E_γ at -138 keV. Jennings et. al. note that, at the time of their publication, the reasonable range of radius for their hard sphere model corresponds to a 5% error in extrapolating $S_{17}(0)$, even when using low energy data below the M1 resonance. Other uncertainties in his model lead to an additional 5% estimated uncertainty.

We have chosen to use the cluster model originally created by Descouvemont and Baye (DB)[21] and updated by Descouvemont[20] in the determination of our mean values. We have attached significant weight to the energy dependence of $S_{17}(E)$ since there is no other testable parameter for all relevant theories. This cluster model calculation, along with a fitted 1^+ resonance, fits the energy dependence of our ^{7}Be(p,γ)^{8}B data best for all energies below 1200 keV.

There is no reason to assume, a priori, that scaling a calculated theory by an overall normalization is the proper way to fit theory to experiment. For instance, changing the normalization could interact with other features of the model to change the energy dependence. The continued work on the D04 theory shows that the energy dependence is essentially determined, and changes in the theory which affect the normalization have small effects on the slope of the theory [20, 21].

In addition, there is significantly more comparison of the DB and D04 theories to physically known quantities than is available for other models. See, for example, Section III of [20]. Because of these factors we use these calculations exclusively in determining a mean value for $S_{17}(0)$.

5.1.2 Cluster Models

Cluster models calculate reaction cross sections by determining the bound state parentage in terms of a limited number of clusters, and then comparing the over-

lap of this bound state with the channel by which the reaction of interest occurs. As new clusters are added to the calculation which do not contribute to the reaction of interest, they reduce the calculated overlap between the states, thereby reducing the calculated S-factor. Hence, a cluster model gives an approximate upper bound on the cross section since it does not incorporate all possible clusters which could make up a nuclear state.

For instance, DB [21] utilizes only the 3+4+1 clusters, i.e. (α + ^{3}He) + p and (α + p) + ^{3}He. The updated theory D04 ([20]) also incorporates the 7+1 clusters, i.e. ^{7}Be + p.

As new clusters are added to the model the theoretical S-factor may be expected ideally to converge on the experimentally measured values. It is important to note also that the shape of S_{17}(E) changed very little in D04 compared to DB. This lends support to the commonly used technique of fitting theoretical S_{17}(E) curves to experimental data using a 1-parameter scaling factor to adjust normalization.

5.1.3 Extrapolation Uncertainty

We used all available published calculations at the time of our BE3 measurement to determine the uncertainty in $S_{17}(0)$. These theories represented the the spread in microscopic and potential models, and the variance among them served as a measure of the theoretical uncertainty of S_{17}(E).

We fit each calculation to our BE3 data with $\bar{E}_{\text{c.m.}} \leq$362 keV. The results, shown in Figure 5.1, show a spread of 2 eV b at zero energy, with an rms deviation of $\pm$0.6 eV b. We adopt this as the standard deviation for our theoretical extrapolation uncertainty. Combined with Equation 4.2, we report:

$$S_{17}(0) = 22.2 \pm 0.6(\text{expt}) \pm 0.6(\text{theory}) \text{ eV b} , \tag{5.1}$$

Table 5.1: $S_{17}(20)$ and $S_{17}(0)$ (in eV b) from fitting our data as published in [42] with $\bar{E}_{\rm c.m.} \leq 362$ keV with different models, as in Fig. 5.1 and ref. [5].

Model	$S_{17}(20)$	$S_{17}(0)$
Nunes	20.8	21.4
Johnson	20.5	21.2
Bennaceur	21.5	22.2
Barker B80	20.7	21.2
Barker B1	21.8	22.6
Barker B2	21.1	21.8
Csoto C2B	21.7	22.0
Csoto C8B	21.8	22.1
Jennings $r_c = 2.4$ fm	22.0	22.8
Jennings $r_c = 1.0$ fm	21.1	21.8
Typel	20.3	20.8
Descouvemont DB	21.4	22.2

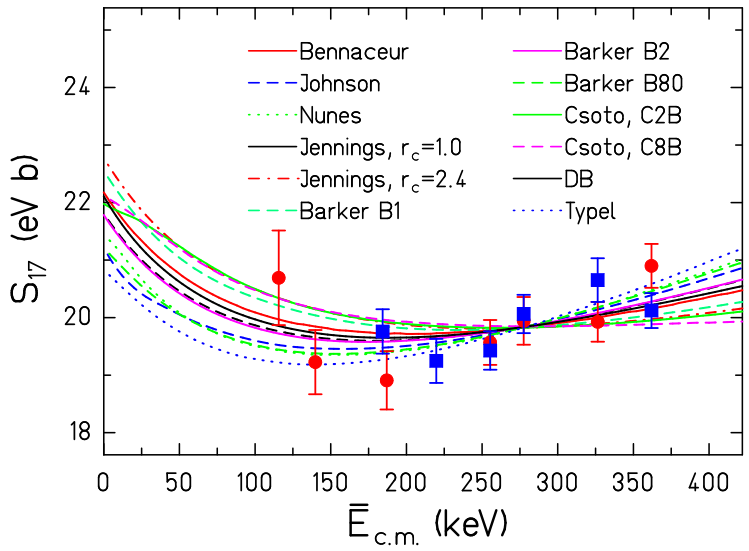

Figure 5.1: Fits of 12 different theories [5] to the BE3 data of [42] below the resonance. BE3 S – circles. BE3 L – squares.

5.2 Modern Experiments

Following the work of Filippone (see Section 1.5), many measurements were made to determine $S_{17}(0)$. As mentioned previously, these measurements fall in to two main categories. Direct measurements measure the cross section of ^{7}Be(p,γ)^{8}B and use this to calculate $S_{17}(0)$. Indirect methods measure the yield of a different reaction and use fundamental symmetries and theoretical calculations to derive $S_{17}(0)$.

5.3 Comparison of Direct Experiments

In 1998 Weissman et. al. [65] addressed the uncertainty in ^{7}Be(p,γ)^{8}B by remeasuring the ^{7}Li(d,p)^{8}B cross section. They cite a value of 155 $\pm$ 8 mb, in agreement with the value used by Filippone. Weissman et. al. also address the issue of ^{8}B backscattering. They calculated energy dependent corrections to Filippone's S_{17}(E) which varied

between 2-10% (see Figure 4. of [65]). We were not able to reproduce these results. These corrections are a factor of two larger than those we calculated using the target composition information of [25] (see Section 5.3.1). Following the Weissman paper nearly all experiments used low Z backings or other methods to reduce or remove the impact of backscattering on their measurements.

Hammache et. al. made the only modern direct measurement of $S_{17}(0)$ which did not use a rotating arm. Instead, they used a fixed, water-cooled target irradiated with high beam currents. The target was irradiated for a short period, then the beam was deflected away electromagnetically and the α-counters were turned on. To detect the β-delayed αs in this scheme required two mechanical shutters. One shutter was in front of the α-detectors to protect them during the irradiation phase, and the second set closed during the counting phase to prevent any neutral particles in the beam from entering the chamber. They report $S_{17}(0) = 18.5 \pm 1.7$ eV b utilizing a ^{7}Li(d,p)^{8}Li normalization, and $S_{17}(0) = 18.5 \pm 1.0$ eV b when the S-factor is determined utilizing the ^{7}Be activity.

The measurement of Hass et. al. [36] in 1999 used an implanted target to avoid issues with backscattering raised by Weissman et. al., and roughly verified by Strieder et. al. [65, 60]. The target was produced at ISOLDE, and implanted ^{7}Be in a copper substrate. This experiment utilized a rotating arm and beam sweep techniques similar to that used by Filippone. This measurement was made at high energies, and was meant to serve as a benchmark for previous experiments as well as experiments to come. Measurements at E_{cm}=1.09 MeV and 1.29 MeV yielded $S_{17}(E_{c.m.}) = 22.7 \pm 1.2$ eV b and 23.8 ± 1.5 eV b, respectively. This corresponds to $S_{17}(0) \approx 20.3$ eV b.

Strieder et. al. [59] published a report in 2001 of their measurement which utilized a rastered beam and a rotating target arm similar to [26, 36]. The ^{7}Be target in this experiment was placed on a copper backing in order to eliminate backscattering of ^{8}B

from the target after bombardment. Strieder reported $S_{17}(0) = 18.4 \pm 1.4$ eV b.

Hammache et. al. published a second measurement [32] in 2001 of a measurement made at lower energies than in their first experiment. They utilized a large solenoidal field to enable them to detect the positrons in coincidence with the delayed αs, thereby reducing backgrounds drastically. Utilizing only the three low energy data points of this measurement, Hammache et. al report $S_{17}(0) = 18.5 \pm 2.4$ eV b.

Following the work laid down in [36], Baby et. al. published a more extensive experiment with an implanted target in 2003 [10]. The experiment again utilized an implanted target. They estimate negligible backscattering losses, <0.2%. The experiment made use of an apparatus similar to [26, 36, 59, 41], using a rotating arm to carry the target from an irradiation position to a counting position removed from the incident beam. The target utilized in this measurement was used for a separate experiment in the middle of data taking, during which it suffered significant damage due to overheating. Baby et. al. made corrections to the data for this change in target characteristics, but it is notable that the lowest energy data of Baby et. al. come from this compromised target. Rather than utilize a Monte Carlo or other simulation to describe and fit their α spectra, Baby et. al. simply fitted with a Gaussian distribution around the peak of each spectrum. Because the shape of the distribution is dependent on bombarding energy this method may bias the value and slope of S_{17}(E) by counting relatively fewer low energy events in the α spectra at low proton bombardment energy.

Later that same year we published an extensive article [42] which discussed in detail the measurements of BE1, as well as new measurements with two more targets, which we label BE2 and BE3. The details of these three experiments form the body of this work.

In order to compare direct measurements we fit published data with the DB theory.

This was done to compare all data using the same theoretical extrapolation. We did this over two energy ranges: $\bar{E}_{c.m.} \leq 425$ keV and $\bar{E}_{c.m.} \leq 1200$ keV. A substantial effort was put forth to avoid error in doing this by obtaining data from the primary sources whenever possible and by fitting the data ourselves. We thereby avoided mistakes and omissions in data that are present in the database compilations as well as errors of fitting that can occur when theoretical models are obtained from other than the primary source.

The fit over the low energy range is motivated by many factors. Some systematic uncertainties improve in the low energy region (see Sections 3.7, 3.8 and 4.5.1). Most significantly, the variation among theories is much smaller over the low energy range.

The fit over the higher energy range was performed because not all data sets have good precision over the lower energy range. In the wide range fits it is important to include the 1^+ resonance, since the high-energy tail of this resonance contributes significantly at energies above the resonance. For these fits to other data we used the 1^+ resonance parameters fixed from the fit to our data and we excluded the data of others closest to the resonance.

5.3.1 Normalization of data sets

For data which were normalized to the ^{7}Li(d,p)^{8}Li cross-section we renormalized the published data using $\sigma[^7\text{Li(d,p)}^8\text{Li}]$=152±6 mb, which is the average of the results quoted in Refs. [2, 65], at the peak of the broad 780 keV resonance. There may be additional error in the results of [51, 43, 64, 26] due to backscattering of ^{8}B and ^{8}Li, as discussed in Section 3.8. We did not make calculations for Ref. [51, 43, 64]. Using the target composition data from [25] we estimated backscattering losses for the data of Ref. [26] using TRIM. We calculated the ^{8}B backscattering loss which directly affects the measured ^{7}Be(p,γ)^{8}B cross-section as well as the loss of ^{8}Li in the

Table 5.2: Experimental $S_{17}(0)$ values and uncertainties in eV b determined by our DB fits to published data, except where indicated.

Fit Range	$\leq$ 425 keV		$\leq$ 1200 keV	
Experiment	Value	Error	Value	Error
Filippone	20.7	2.5	19.4	2.2
Hammache	20.1	1.3	19.4	1.1
Hass			20.4	1.1
Strieder	18.8	1.8	18.1	1.6
Baby	20.8	1.3[1]	21.9	0.7[1]
Junghans	22.2	0.6	22.3	0.6
$\leq$425 keV best fit	21.5	0.5		
$\leq$1200 keV best fit			21.3	0.4

^{7}Li(d,p)^{8}Li reaction which was used in Ref. [26] in one of their two absolute cross-section determinations. We found corrections which varied with proton energy from -2% to -4%, which is smaller than the determination of Ref. [65]. These results are small compared to the full errors on the data so we ignored them. Hammache et. al. [33] applied calculated backscattering corrections to their data. Strieder et. al. [59] used a low-Z backing and Baby et. al. [10] used an implanted target, both of which should have negligible backscattering losses. We did not make corrections to any of these published data for backscattering effects.

Care was taken to properly separate common mode errors from other errors. The data was then fit with only the non-common mode errors, and the common mode errors where folded with the errors resulting from the fit. The results for both fitting ranges are shown in Fig. 5.2 and Table 5.2.

Our fitted results for $S_{17}(0)$ differ from the published results in Ref. [33]. Our fits

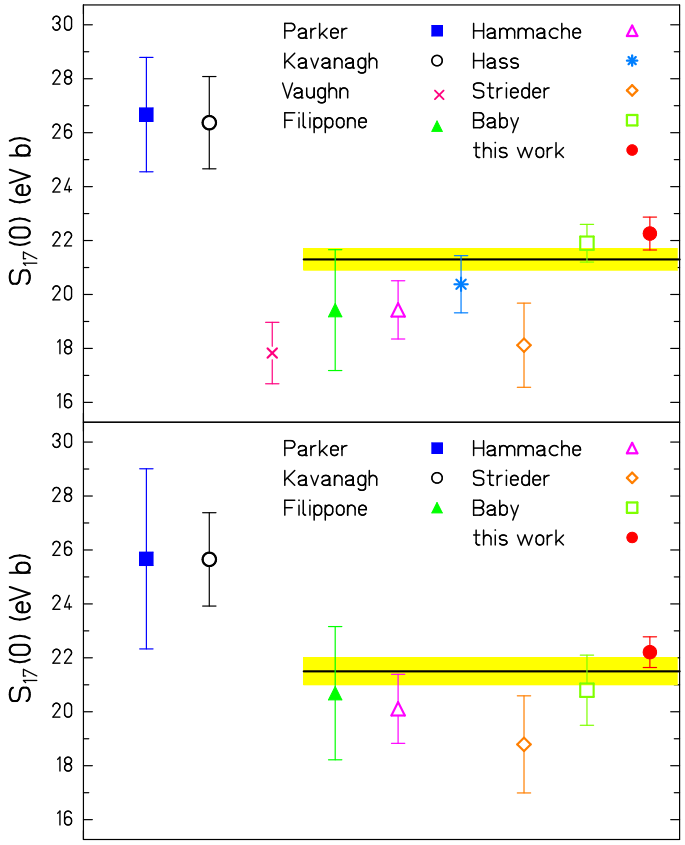

Figure 5.2: $S_{17}(0)$ values determined from our DB fits to published data from direct experiments. Bottom panel (top panel): fits to data with $\bar{E}_{\rm c.m.} \leq 425$ keV (1200 keV). The horizontal solid lines and shaded bands indicate the mean values and uncertainties determined from fitting the data of Filippone and more recent experiments.

with the theory of Descouvemont and Baye are 6% and 4% lower over the low and high fit regions, respectively. This is due in part to the use of an incorrect fit function for the theory of Descouvemont and Baye in the 2001 paper of [33]. The values from [10] and the 1998 paper of [33] are also somewhat lower than our fitted results.

5.3.2 Combined results of direct experiments

Excepting the earlier experiments of Parker [51], Kavanagh [43], and Vaughn [64] the data presented in Figure 5.2 were fit to determine a mean value, as indicated by the shaded bar. For $\bar{E}_{\rm c.m.} \leq 425$ keV $S_{17}(0) = 21.5 \pm 0.5$ eV with a χ^2/ν=1.2 ($\nu = 4$). For $\bar{E}_{\rm c.m.} \leq 1200$ keV $S_{17}(0) = 21.3 \pm 0.4$ eV with a χ^2/ν=2.4 ($\nu = 5$). For the reasons stated earlier, we believe the low energy ($\bar{E}_{\rm c.m.} \leq 425$ keV) fit to be the more reliable determination of $\rm S_{17}(0)$, and so report a best value of $S_{17}(0)$ from direct experiments of:

$$\rm S_{17}(0)_{\mathit{direct}} = 21.5 \pm 0.5(expt) \pm 0.6(theor)\ \ eV\ b, \tag{5.2}$$

The good agreement of the result from the two different fit ranges demonstrates that the energy dependence of S_{17} is well understood over the range fit, e.g. at least up to 1200 keV, and that this energy dependence is well determined by direct experiments. In Figure 5.3 we compare the energy dependence of the direct experiments used in our calculation of Equation 5.2. For comparision, all data were normalized to $S_{17}(0) = 21.3$ eV b based on our best fit value over the energy range of $\bar{E}_{\rm c.m.} \leq$ 1200 keV. There is good agreement of the energy dependence between the various direct experiments, along with the agreement between $S_{17}(0)$ values determined with fits over different energy ranges. These features are important in the examination of indirect experiments.

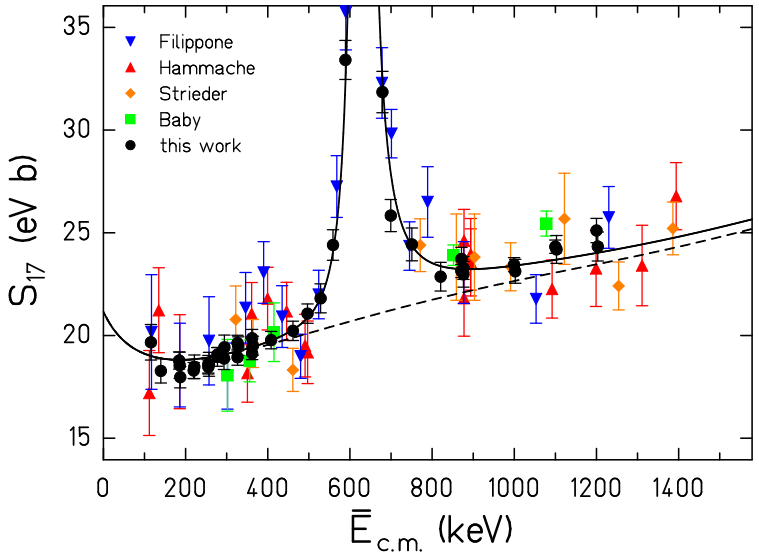

Figure 5.3: S-factor data from direct experiments, all normalized to a common value of $S_{17}(0)$ (the mean DB best-fit value of 21.3 eV b - see Table 5.2). The error bars shown are relative, and do not include scale-factor uncertainties. Solid curve: DB plus a 1^+ resonance with parameters determined from fitting our BE1 data. Dashed curve: DB only. Calculations and data were normalized from fits in the energy range $\bar{E}_{\rm c.m.} \leq 1200$ keV.

5.4 Comparison of Indirect Experiments

There are ways to determine $S_{17}(0)$ other than directly measuring the cross section of ^{7}Be(p,γ)^{8}B. Called "indirect" techniques because they work on principles other than directly measuring the quantity of interest, they make use of physical symmetries and extensive theoretical calculations to extract $S_{17}(0)$ from other reactions. These measurements fall into two categories.

Coulomb dissociation experiments use a beam of ^{8}B nuclei targeted on a heavy nucleus such as Pb or Au. The ^{8}B nucleus breaks up by interacting with one of the virtual γ's in the coulomb field of the heavy nucleus, or perhaps with the tail of the nuclear interaction. By using momentum selection to look at only the reactions which break up into ^{7}Be + p they are able to measure a cross section which is related theoretically to the ^{7}Be(p,γ)^{8}B reaction.

The break-up and transfer of heavy ions also provides a way to look at quantities related to the ^{7}Be(p,γ)^{8}B cross-section. For this technique peripheral transfer reactions of the form ^{n}A(^{7}Be,^{8}B)$^{n-1}$(A-1) yield information about the overlap between the ^{7}Be + p and ^{8}B wave functions.

These techniques involve significantly more of modeling, theoretical work, and the understanding of different systematics, than do direct measurements. Perhaps of greatest importance is that many of the systematic uncertainties come from theoretical calculations and can not be checked directly by experiment.

Motobayashi et. al. published such a measurement in 1994 [48], after Filippone had reopened the door on S_{17}, but before the many measurements which were to come in the late 90s and following years. The experiment was done at RIKEN, where a radioactive beam of 46.5 MeV/nucleon ^{8}B interacted with the virtual photon field of a heavy nucleus (^{208}Pb) and was photodissociated. The measurement used δE and E detectors, along with time of flight (ToF) information to identify particles, allowing

the separation of the ^{208}Pb(^{8}B,^{7}Be + p)^{208}Pb events. The measurement included relative ^{7}Be + p energies, E_{rel}, corresponding to $E_{c.m.}$ in direct measurements of ^{7}Be(p,γ)^{8}B, such that 600 keV $\leq E_{rel} \leq$1.7 MeV.

This first application of the Coulomb dissociation (CD) technique to ^{7}Be(p,γ)^{8}B acknowledges the possibility of Coulomb post-acceleration, as well as a contribution from an E2 channel which is weighted differently than in direct measurements, but did not include corrections for these effects.

The RIKEN group published again in 1998 [45]. This measurement was made with a 51.2 MeV/nucleon beam, and an increased acceptance of $0.4 \leq E_{rel} \leq 3$ MeV. The result of this measurement was $S_{17}(0) = 18.9 \pm 1.8$ eV b.

Shortly thereafter a measurement which much higher beam energies (254 MeV/nucleon) was made at GSI [39], in Darmstadt. The much higher incident beam energy focuses the reaction products in the forward direction. This allowed Iwasa et. al. to use a large acceptance spectrometer to separate out the ^{208}Pb(^{8}B,^{7}Be + p)^{208}Pb events from other dissociation events. They also state that it improves the ratios of various channels which contribute to the cross section, e.g. E1 vs. E2, and increased the size of the M1 resonance, allowing it to be used for calibration purposes. From measurements with $E_{c.m.}$ = 0.25 to 2.78 MeV, they report $S_{17}(0) = 20.6 \pm 1.2$ (expt) $\pm$ 1.0 (theor) eV b.

In addition to Coulomb dissociation, transfer reactions have been used to make indirect measurements of $S_{17}(0)$. In such a transfer reaction a ^{7}Be beam interacts with the target nucleus and picks up a proton, becoming ^{8}B. From this reaction it is possible to extract the asymptotic normalization coefficient (ANC) using a distorted wave Born approximation (DWBA), which characterizes the asymptotic, as r $\rightarrow \infty$, overlap of the ^{8}B and ^{7}Be + p wave functions. At the low energies of interest in the stellar environment the stellar reactions are almost completely extra-nuclear.

Therefore, a measurement of the ANC and a theoretical understanding of the system should be enough to calculate the S-factor at zero energy. Azhari et. al. [9] report the first measurement of $S_{17}(0)$ using this technique in 2001. They measured the ^{10}B(^{7}Be,^{8}B)^{9}Be and ^{14}N(^{7}Be,^{8}B)^{13}C transfer reactions and report $S_{17}(0) = 17.3 \pm 1.8$ eV b.

Trache et. al. [63] published a measurement that same year which used a different method to arrive at the ANC for ^{8}B and ^{7}Be + p. They utilized breakup reactions (one proton removal), rather than transfer reactions. In a breakup reaction the incident beam breaks apart under interaction with a target nucleus. The measurements were made at many beam energies, between 30 and 300 MeV/nucleon, and with a variety of targets, such as ^{12}C, Sn, and ^{208}Pb. Trache et. al. claim good agreement between all measurements, and an ANC that corresponds to $S_{17}(0) = 17.4 \pm 1.5$ eV b.

The ANC technique does not yield S_{17}(E), but rather only an essential ingrediaent in calculating $S_{17}(0)$. This makes it much harder to compare to other measurements, especially since it provides no information regarding the slope of S_{17}(E). It also requires significant theoretical modeling to extract the ANC, and then a second (albeit less complicated) model to compute $S_{17}(0)$ from the ANC.

Davids et. al. published a Coulomb dissociation measurement made at the NCSL at MSU in 2003 with an 83 MeV/nucleon ^{8}B beam. They incorporated an analysis which included E1, E2, and M1 transitions. They report on data with $E_{c.m.}$ from 130 keV to 400 keV and fit this low energy data to, yielding $S_{17}(0) = 17.8\ ^{+1.4}_{-1.2}$ eV b. They were able to take data below 100 keV, but did not use it in the analysis because of a stated strong E2 contribution at those energies.

The disagreement between [48, 45, 39, 17] on the contribution of E2 transitions in the CD reaction rate led the group at GSI to make another measurement in 2003. The work of Schümann et. al. reports an improved apparatus from [39]. The new

experimental apparatus allowed them to measure quantities which would be sensitive to the E2 transition, namely the angular correlations between the ^{7}Be and protons. Using first order perturbation theory, they find a contribution from E2 transitions to be significantly less than the error bars on the data, and therefore of negligible importance for $S_{17}(0)$. With this analysis they report $S_{17}(0) = 18.6 \pm 1.2$ (expt) $\pm$ 1.0 (theor) eV b.

Ogata et. al. [50], motivated by [24], used the method of continuum-discretized coupled channels (CDCC) to reanalyze the work of [48, 45], taking into account post-acceleration, E2 contributions, and higher order Coulomb breakup processes. Ogata et. al. report a new value for $S_{17}(0)$ from these experiments of $S_{17}(0) = 20.9 \pm 1.8$ (expt) $^{+1.0}_{-0.6}$ (theor) eV b.

The CD group at GSI also published a new result in 2006 [58]. In this paper Schumann et. al. made a new CD measurement, including careful controls of their systematics and examination of potential and dynamic models to determine the best fit to their data. Their result is a data set with a slope distinctly smaller than the 2003 publication, more in line with the DB and D04 cluster models [21, 20], rather than Typel's model, which they used previously (see [5]). They report a value of $S_{17}(0) = 20.6 \pm 0.8$ (stat) $\pm$ 1.2 (sys), not including errors from the theoretical extrapolation to zero energy, where they quote Descouvement's figure of 5%.

These publications place the CD measurements of [48, 45, 58] and direct measurements of [36, 42, 10] in much better agreement. It also makes clear the importance and effect of theoretical modeling in indirect methods.

5.4.1 Coulomb Dissociation

Aside from the technical difficulties of using a radioactive beam (^{8}B) Coulomb dissociation experiments require an accurate theoretical understanding of the virtual

photon field of the target nucleus. The various multipolarities contribute differently to the break-up reaction than they do in the photon emission spectrum of direct experiments. Therefore, detailed knowledge of the multipole decomposition is required of both the virtual photon field of the target nucleus as well as the photon emission spectrum of ^{7}Be(p,γ)^{8}B to convert a measured Coulomb dissociation cross section into a direct cross section.

This conversion is made by assuming that the direct cross section, with the exception of resonances, is purely electric dipole (E1) in nature. This is not true of the virtual photon spectrum, as the electric quadrapole (E2) is enhanced by several orders of magnitude. Theory does not predict this enhancement well, and cannot say if it remains negligible in the Coulomb dissociation process. The work of Schümann et. al. [57] found this countribution to be negligible, while that of Davids et. al [17] found it to be small, but significant. Esbensen et. al. [24] utilize a two body model to examine the effect of utilizing this far field approximation on the energy dependence of S_{17}, as well as the value of $S_{17}(0)$. This analysis extracts a lower slope for all experiments analyzed ([17, 45, 57]), as well as modified values for $S_{17}(0)$ for Davids et. al. and Kikuchi et. al.

All of the experiments reviewed here included the 1^{+} M1 resonance at 630 keV, but make no corrections for other M1 resonances in the system, such as the 3^{+} resonance discussed in Section 4.5.2. Higher electric and magnetic multipoles are negligible and are not included in calculations.

An additional correction enters because of three body effects which can happen after the decay. Post decay effects happen when the charge to mass ratio of the collision products are different, so they are accelerated differently by the Coulomb field of the target nucleus after break up. This is increasingly important as the collision products spend more time in close proximity of the target nucleus. This

happens for small impact parameters, and therefore large scattering angles. It also occurs when the bombarding energy is low. Estimations of Alt et. al. [6] cite that this effect may cause a correction to $S_{17}(0)$ as large as 4% in some experiments.

5.4.2 Heavy Ion Transfer and Breakup Reactions

Transfer and breakup reactions are used to determine the asymptotic normalization coefficient (ANC) for the ^{7}Be + p component of the ^{8}B groundstate. Because ^{7}Be(p,γ)^{8}B happens at very low energies in the Sun, the capture is almost completely extra-nuclear. Because of this a capture model and an assumed $p_{3/2}$ to $p_{1/2}$ ratio in ^{7}B + p, can be used with the ANC to calculate $S_{17}(0)$. This technique depends upon theoretical uncertainties in the capture model, the relative $p_{3/2}$ and $p_{1/2}$ contributions, and uncertainties in the initial extraction of the ANC. One of the major disadvantages of this technique is that it does not yield S_{17}(E), but only a value at zero energy. It is not possible to compare energy dependence or other features to observables determined with other techniques.

For a technique dominated by theoretical uncertainty it is important to verify it against well known directly measured experimental results. In addition to ^{7}Be(p,γ)^{8}B, this comparison has been made for ^{16}O(^{3}He,d)^{17}F [31]. The transfer measurement results of [31] are compared to two direct measurements [14, 47]. The systematics in these papers are not clearly reported, or not reported at all, which makes the level of agreement hard to determine to better than 10% or 20%.

The work of Trache et. al. [63] uses heavy ion transfer, stripping, and breakup reactions to find the ANC for ^{7}Be + p $\leftrightarrow$ ^{8}B finds $S_{17}(0) = 17.4 \pm 1.5$ eV b. Other analyses [13, 23] have cited the larger value for $S_{17}(0) = 21.2 \pm 1.3$ eV b.

5.5 Recommended Values

There is continued discussion of direct, indirect, and theoretical methods relevant to determining $S_{17}(0)$. The references listed above are a collection of much of that discussion. At this time the discrepencies indirect methods have internally and with direct measurements make it difficult to accomodate them into a recommended value for $S_{17}(0)$. Because of this only direct measurements are included in the determination of $S_{17}(0)$ for this work. It should be noted that there is continued progress in this field, and direct and indirect measurements are slowly coming in to agreement on the two notable observables, i.e. $S_{17}(0)$ and the slope of $S_{17}(E)$.

As stated previously, this method leads to a recommended value, with quoted 1σ errors, of:

$$S_{17}(0) = 21.5 \pm 0.5(\text{expt}) \pm 0.6(\text{theor}).\ \text{eV b}, \tag{5.3}$$

Chapter 6
CONCLUSION AND SUMMARY

6.1 Summary

This work details a precision measurement of the astrophysical ^{7}Be(p,γ)^{8}B S-factor, S_{17}. The measurement was accomplished utilizing new experimental methods, as well as improving upon some previously utilized techniques. We measured most systematic effects in the experiment rather than relying on calculated corrections, whenever possible, to generate a result as unbiased by assumption as possible. In the few cases where corrections were calculated and not measured conservative uncertainties were applied.

6.2 Impact and Outlook

6.2.1 Experimental Technique

Chapter 2 presents a thorough description of the apparatus and the manner in which we made precision nuclear physics measurements. The use of a ferro-fluidic seal to allow a rotating arm to pass through the wall of a vacuum chamber, measurement of backscattering (Section 2.2.4), and fabrication of uniform radioactive targets using a target backing with a post and washer design (Section 2.1), are significant improvements to the state of the art.

Many other important techniques are described in detail, including the use of a large-area, uniform beam (see Section 3.1), solid angle calibration via multiple techniques (Section 3.3), and an oil free vacuum system (Section 2.2.2).

6.2.2 Effect on Solar Models

The primary importance of the ^{7}Be(p,γ)^{8}B reaction rate is as an input to solar models. Previous to this work the ^{7}Be(p,γ)^{8}B reaction rate at astrophysical energies, typically reported as S_{17}, had the largest uncertainty of the nuclear physics parameters used to predict ^{8}B neutrino production in the sun. Reducing the uncertainty in S_{17} leaves S_{34} as the dominant nuclear physics uncertainty [11].

6.2.3 Application to Neutrino Physics

The measurement of S_{17} does not have a large effect on most analyses of the solar neutrino spectrum and neutrino mixing parameters. The different solar neutrino experiments, particularly their differing energy threshholds, allows analyses independent of solar models, and therefore independent of nuclear physics inputs to those models.

It is in exploring non-standard model physics, including possible sterile neutrinos, that the solar model becomes important as a constraint on theoretical neutrino models.

6.2.4 Calibration of Indirect Measurements

The value of using direct measurements of ^{7}Be(p,γ)^{8}B as a calibration for indirect measurement methods should not be underestimated. There are many reactions which are impractical to measure with direct methods for various reasons. Because it is not possible to check these measurements against direct measurements it is important to fully understand the systematics of the indirect techniques by comparison to directly measured reactions, such as ^{7}Be(p,γ)^{8}B.

BIBLIOGRAPHY

[1] Figure created by A. R. Junghans.

[2] E. G. Adelberger, S. M. Austin, J. N. Bahcall, A. B. Balantekin, G. Bogaert, L. S. Brown, L. Buchmann, F. E. Cecil, A. E. Champagne, L. de Braeckeleer, C. A. Duba, S. R. Elliot, S. J. Freedman, M. Gai, G. Goldring, C. R. Gould, A. Gruzinov, W. C. Haxton, K. M. Heeger, E. Henley, C. W. Johnson, M. Kamionkowski, R. W. Kavanagh, S. E. Koonin, K. Kubodera, K. Langanke, T. Motobayashi, V. Pandharipande, P. Parker, R. G. H. Robertson, C. Rolfs, R. F. Sawyer, N. Shaviv, T. D. Shoppa, K. A. Snover, E. Swanson, R. E. Tribble, S. Turck-Chièze, and J. F. Wilkerson. Solar fusion cross sections. *Review of Modern Physics*, 70:1265, 1998.

[3] Q. R. Ahmad, R. C. Allen, T. C. Andersen, J. D.Anglin, J. C. Barton, E. W. Beier, M. Bercovitch, J. Bigu, S. D. Biller, R. A. Black, I. Blevis, R. J. Boardman, J. Boger, E. Bonvin, M. G. Boulay, M. G. Bowler, T. J. Bowles, S. J. Brice, M. C. Browne, T. V. Bullard, G. Bhler, J. Cameron, Y. D. Chan, H. H. Chen, M. Chen, X. Chen, B. T. Cleveland, E. T. H. Clifford, J. H. M. Cowan, D. F. Cowen, G. A. Cox, X. Dai, F. Dalnoki-Veress, W. F. Davidson, P. J. Doe, G. Doucas, M. R. Dragowsky, C. A. Duba, F. A. Duncan, M. Dunford, J. A. Dunmore, E. D. Earle, S. R. Elliott, H. C. Evans, G. T. Ewan, J. Farine, H. Fergani, A. P. Ferraris, R. J. Ford, J. A. Formaggio, M. M. Fowler, K. Frame, E. D. Frank, W. Frati, N. Gagnon, J. V. Germani, S. Gil, K. Graham, D. R. Grant, R. L. Hahn, A. L. Hallin, E. D. Hallman, A. S. Hamer, A. A. Hamian, W. B. Handler, R. U. Haq, C. K. Hargrove, P. J. Harvey, R. Hazama, K. M. Heeger, W. J. Heintzelman, J. Heise, R. L. Helmer, J. D. Hepburn, H. Heron, J. Hewett, A. Hime, M. Howe, J. G. Hykawy, M. C. P. Isaac, P. Jagam, N. A. Jelley, C. Jillings, G. Jonkmans, K. Kazkaz, P. T. Keener, J. R. Klein, A. B. Knox, R. J. Komar, R. Kouzes, T. Kutter, C. C. M. Kyba, J. Law, I. T. Lawson, M. Lay, H. W. Lee, K. T. Lesko, J. R. Leslie, I. Levine, W. Locke, S. Luoma, J. Lyon, S. Majerus, H. B. Mak, J. Maneira, J. Manor, A. D. Marino, N. McCauley, A. B. McDonald, D. S. McDonald, K. McFarlane, G. McGregor, R. Meijer Drees, C. Mifflin, G. G. Miller, G. Milton, B. A. Moffat, M. Moorhead, C. W. Nally, M. S. Neubauer, F. M. Newcomer, H. S. Ng, A. J. Noble, E. B. Norman, V. M. Novikov, M. O'Neill, C. E. Okada, R. W. Ollerhead, M. Omori, J. L. Orrell, S. M.

Oser, A. W. P. Poon, T. J. Radcliffe, A. Roberge, B. C. Robertson, R. G. H. Robertson, S. S. E. Rosendahl, J. K. Rowley, V. L. Rusu, E. Saettler, K. K. Schaffer, M. H. Schwendener, A. Schlke, H. Seifert, M. Shatkay, J. J. Simpson, C. J. Sims, D. Sinclair, P. Skensved, A. R. Smith, M. W. E. Smith, T. Spreitzer, N. Starinsky, T. D. Steiger, R. G. Stokstad, L. C. Stonehill, R. S. Storey, B. Sur, R. Tafirout, N. Tagg, N. W. Tanner, R. K. Taplin, M. Thorman, P. M. Thornewell, P. T. Trent, Y. I. Tserkovnyak, R. Van Berg, R. G. Van de Water, C. J. Virtue, C. E. Waltham, J.-X. Wang, D. L. Wark, N. West, J. B. Wilhelmy, J. F. Wilkerson, J. R. Wilson, P. Wittich, J. M. Wouters, and M. Yeh. Direct evidence for neutrino flavor transformation from neutral-current interactions in the Sudbury Neutrino Observatory. *Physical Review Letters*, 89(1):011301, Jun 2002.

[4] F. Ajzenberg-Selove. Energy levels of light nuclei A = 5-10. *Nuclear Physics A*, 490:1, 1988.

[5] DB, B1, B2, C2B, C8B, 1.0 and 2.4 as defined in [40], plus: F. C. Barker, Aust. J. Phys. **33**, 177, 1980; C. W. Johnson, E. Kolbe, S. E. Koonin and K. Langanke, Astrophys. Jour. **392**, 320 (1992); F. M. Nunes, R. Crespo and I. J. Thompson, Nucl. Phys. A **634**, 527 (1998); K. Bennaceur, F. Nowacki, J. Okołowicz and M. Płoszajczak, Nucl. Phys. A **651**, 289 (1999); S. Typel, H. H. Wolter and G. Baur, Nucl. Phys. A **613**, 147 (1997); P. Descouvemont, Phys. Rev. C **70**, 065802 (2004), and private comms.

[6] E.O. Alt, B.F. Irgaziev, and A.M. Mukhamedzhanov. Final state three-body Coulomb effects in the ^{208}Pb(^{8}B,^{7}Be p)^{208}Pb Coulomb breakup reaction. *Physical Review Letters*, 90:122701, 2003.

[7] C. Angulo, P. Descouvemont, M. Cogneau, M. Couder, M. Gaelens, P. Leleux, M. Loiselet, G. Ryckewaert, G. Tabacaru, F. Vanderbist, T. Davinson, M. Azzouz, D. Baye, A. Di Pietro, P. Figuera, R. G. Pizzone, F. de Oliveira Santos, and N. de Séréville. The elastic scattering ^{7}Be + p at low energies: implications on the ^{7}Be(p,γ)^{8}B S-factor. *Nuclear Physics A*, 719:300, 2003.

[8] Martin Asplund, Nocolas Grevesse, and A. Jacques Sauval. The solar chemical composition. *Nuclear Physics A*, 777:1, 2006.

[9] A. Azhari, V. Burjan, F. Carstoiu, C. A. Gagliardi, V. Kroha, A. M. Mukhamedzhanov, F. M. Nunes, X. Tang, L. Trache, and R. E. Tribble. Asymp-

totic normalization coefficients and the ^{7}Be(p,γ)^{8}B astrophysical S factor. *Physical Review C*, 63(5):055803, Apr 2001.

[10] L.T. Baby, C. Bordeanu, G. Goldring, M. Hass, L. E. Weissman, V.N. Fedoseyev, U. Köster, Y. Nir-El, G. Haquin, H.W. Gäggeler, R. Weinreich, and ISOLDE Collaboration. New measurement of the proton capture rate on ^{7}Be and the $S_{17}(0)$ factor. *Physical Review Letters*, 90:022501, 2003.

[11] John N. Bahcall and M. H. Pinsonneault. What do we (not) know theoretically about solar neutrino fluxes? *Phys. Rev. Lett.*, 92(12):121301, Mar 2004.

[12] F. Barker. Delayed alpha spectra from the beta decay of ^{8}Li and ^{8}B. *Australian Journal of Physics*, 42:25, 1989.

[13] B.A. Brown, P.G. Hansen, B.M. Sherrill, and J.A. Tostevin. Absolute spectroscopic factors from nuclear knockout reactions. *Physical Review C*, 65:061601, 2002.

[14] H.C. Chow, G. M. Griffiths, and T.H. Hall. The ^{16}O(p, γ)^{17}F direct capture cross section with an extrapolation to astrophysical energies. *Canadian Journal of Physics*, 53:1672, 1975.

[15] S.Y.F. Chu, L.P. Ekström, and R.B. Firestone. The Lund/LBNL nuclear data search version 2.0, February 1999.

[16] Commissariat lEnergie Atomique. http://www.cea.fr/.

[17] B. Davids, D. W. Anthony, T. Aumann, Sam M. Austin, T. Baumann, D. Bazin, R. R. C. Clement, C. N. Davids, H. Esbensen, P. A. Lofy, T. Nakamura, B. M. Sherrill, and J. Yurkon. $S_{17}(0)$ determined from the coulomb breakup of 83 MeV /nucleon ^8B. *Physical Review Letters*, 86(13):2750–2753, Mar 2001.

[18] R. Davis, Jr. Solar neutrinos. II. experimental. *Physical Review Letters*, 12:303, 1964.

[19] Raymond Davis, Don S. Harmer, and Kenneth C. Hoffman. Search for neutrinos from the sun. *Physical Review Letters*, 20(21):1205–1209, May 1968.

[20] P. Descouvemont. Reanalysis of the ^{7}Be(p,γ)^{8}B S factor in a microscopic model. *Physical Review C*, 70:065802–1, 2004.

[21] P. Descouvemont and D. Baye. Microscopic study of the ^{7}Li(n, γ)^{8}Li and ^{7}Be(p, γ)^{8}B reactions in a multiconfiguration three-cluster model. *Nuclear Physics A*, 567:341, 1994.

[22] A. J. Elwyn, R. E. Holland, C. N. Davids, and W. Ray. $^7Li(d,p)^8Li$ reaction cross section near 0.78 MeV. *Physical Review C*, 25(5):2168–2173, May 1982.

[23] J. Enders, T. Baumann, B.A. Brown, N.H. Frank, P.G. Hansen, P.R. Heckman, B.M. Sherrill, A. Stolz, M. Thoennessen, J.A. Tostevin, E. J. Tryggestad, S. Typel, and M.S. Wallace. Spectroscopic factors measured in inclusive proton-knockout reactions on ^{8}B and ^{9}C at intermediate energies. *Physical Review C*, 67:064301, 2003.

[24] H. Esbensen, G.F. Bertsch, and K.A. Snover. Reconciling Coulomb dissociation and radiative capture measurements. *Physical Review Letters*, 94:042502, 2005.

[25] B. W. Filippone. Preparation of a ^{7}Be target via the molecular plating method. *Nuclear Instruments and Methods in Physics Research*, A240:41, 1986.

[26] B. W. Filippone, A.J. Elwyn, and C.N. Davids. Measurement of the ^{7}Be(p,γ)^{8}B reaction cross section at low energies. *Physical Review Letters*, 50:412, 1983.

[27] B. W. Filippone, A.J. Elwyn, C.N. Davids, and D.D. Koetke. Proton capture cross section of ^{7}Be and the flux of high energy solar neutrinos. *Physical Review C*, 28:2222, 1983.

[28] B. W. Filippone, A.J. Elwyn, Jr. W. Ray, and D.D. Koetke. Absolute cross section for ^{7}Li(d,p)^{8}Li and solar neutrino capture rates. *Physical Review C*, 25:2174, 1982.

[29] S. Fukuda, Y. Fukuda, M. Ishitsuka, Y. Itow, T. Kajita, J. Kameda, K. Kaneyuki, K. Kobayashi, Y. Koshio, M. Miur, S. Moriyama, M. Nakahata, S. Nakayama, T. Namba, A. Okada, N. Sakurai, M. Shiozawa, Y. Suzuki, H. Takeuchi, Y. Takeuchi, Y. Totsuka, S. Yamada, M. Earl S. Desa and, E. Kearns, M. D. Messier, J. L. Stone, L. R. Sulak, C. W. Walter, M. Goldhaber, T. Barszczak, D. Casper, W. Gajewski, W. R. Kropp, S. Mined, D. W. Liu, M. B. Smy, H. W. Sobel, M. R. Vagins, A. Gago, K. S. Ganezer, W. E. Keig, R. W. Ellsworth, S. Tasakag, A. Kibayashi, J. G. Learned, S. Matsuno, D. Takemori, Y. Hayato, T. Ishii, T. Kobayashi, T. Maruyama, K. Nakamura, Y. Obayashi, Y. Oyama, M. Sakuda, M. Yoshida, M. Kohama, T. Iwashita, A. T. Suzuki,

A. Ichikawa, T. Inagaki, I. Kato, T. Nakaya, K. Nishikawa, T. J. Haines, S. Dazeley, S. Hatakeyama, R. Svoboda, E. Blaufuss, M. L. Chen, J. A. Goodman, G. Guillian, G. W. Sullivan, D. Turc, K. Scholberg, A. Habig, M. Ackermann, J. Hill, C. K. Jung, M. Malek, K. Martens, C. Mauger, C. McGrew, E. Sharkey, B. Viren, C. Yanagisawa, T. Toshito, C. Mitsuda, K. Miyano, C. Saji, T. Shibata, Y. Kajiyama, Y. Nagashima, K. Nitta, M. Takita, H. I. Kim, S. B. Kim, J. Yoo, H. Okazawa, T. Ishizuka, M. Etoh, Y. Gando, T. Hasegawa, K. Inoue, K. Ishihara, J. Shirai, A. Suzuki, M. Koshiba, Y. Hatakeyama, Y. Ichikawa, M. Koike, K. Nishijima, H. Ishino, M. Morii, R. Nishimura, Y. Watanabe, D. Kielczewska, H. G. Berns, S. C. Boyd, A. L. Stachyra, and R. J. Wilkes. Determination of solar neutrino oscillation parameters using 1496 days of Super-Kamiokande-i data. *Physics Letters B*, 539:179, 2002.

[30] Figure created by G. Harper.

[31] C.A. Gagliardi, R.E. Tribble, A. Azhari, H.L. Clark, Y.-W. Lui, A.M. Mukhamedzhanov, A. Sattarov, L. Trache, V. Burjan, J. Cejpek, V. Kroha, S. Piskor, and J. Vincour. Tests of transfer reaction determinations of astrophysical S factors. *Physical Review C*, 59:1149, 1999.

[32] F. Hammache, G. Bogaert, P. Aguer, C. Angulo, S. Barhoumi, L. Brillard, J. F. Chemin, G. Claverie, A. Coc, M. Hussonnois, M. Jacotin, J. Kiener, A. Lefebvre, C. Le Naour, S. Ouichaoui, J. N. Scheurer, V. Tatischeff, J. P. Thibaud, and E. Virassamynaïken. Low-energy measurement of the $^7Be(p,\gamma)^8B$ cross section. *Physical Review Letters*, 86(18):3985–3988, Apr 2001.

[33] F. Hammache, G. Gogaert, P. Aguer, C. Angulo, S. Barhoumi, L. Brillard, J.F. Chemin, G. Claverie, A. Coc, M. Hussonnois, M. Jacotin, J. Kiener, A. Lefebvre, J.N. Scheurer, J.P. Thibaud, and E. Virassamynaiken. New measurement and analysis of the ^{7}Be(p,γ)^{8}B cross section. *Physical Review Letters*, 80:928, 1998.

[34] G. Hardie, B. W. Filippone, A. J. Elwyn, M. Wiescher, and R. E. Segel. Resonant alpha capture by ^{7}Be and ^{7}Li. *Physical Review C*, 29:1199, 1984.

[35] G. Harper. Annual Report: Center for Experimental Nuclear Physics and Astrophysics. Technical report, University of Washington, 2000. Section 8.3 Tandem terminal ion source.

[36] M. Hass, C. Broude, V. Fedoseev, G. Goldring, G. Huber, J. Lettry, V. Mishin, H. J. Ravn, V. Sebastian, L. Weissman, and ISOLDE Collaboration. A new mea-

surement of the ^{7}Be(p,γ)^{8}B cross-section with an implanted ^{7}Be target. *Physics Letters B*, 462:237, 1999.

[37] heavy-met is 95% tungsten, 1.5% copper and 3.5% nickel by mass.

[38] H. D. Holmgren and R. L. Johnston. $H^3(\alpha,\gamma)Li^7$ and $He^3(\alpha,\gamma)Be^7$ reactions. *Phys. Rev.*, 113(6):1556–1559, Mar 1959.

[39] N. Iwasa, F. Boué, G. Surówka, K. Sümmerer, T. Baumann, B. Blank, S. Czajkowski, A. Förster, M. Gai, H. Geissel, E. Grosse, M. Hellström, P. Koczon, B. Kohlmeyer, R. Kulessa, F. Laue, C. Marchand, T. Motobayashi, H. Oeschler, A. Ozawa, M. S. Pravikoff, E. Schwab, W. Schwab, P. Senger, J. Speer, C. Sturm, and A. Surowiec. Measurement of the Coulomb dissociation of ^{8}B at 254 MeV/nucleon and the ^8B solar neutrino flux. *Physical Review Letters*, 83(15):2910–2913, Oct 1999.

[40] B. K. Jennings, S. Karataglidis, and T.D. Shoppa. Extrapolation of the astrophysical S factor for ^{7}Be(p,γ)^{8}B to solar energies. *Physical Review C*, 58:3711, 1998.

[41] A. R. Junghans, E. C. Mohrmann, K. A. Snover, T. D. Steiger, E. G. Adelberger, J. M. Casandjian, H. E. Swanson, L. Buchmann, S. H. Park, and A. Zyuzin. ^{7}Be(p,γ)^{8}B astrophysical S factor from precision cross section measurements. *Physical Review Letters*, 88:041101, 2002.

[42] A. R. Junghans, E. C. Mohrmann, K. A. Snover, T. D. Steiger, E. G. Adelberger, J. M. Casandjian, H. E. Swanson, L. Buchmann, S. H. Park, A. Zyuzin, and A. M. Laird. Precise measurement of the ^{7}Be(p,γ)^{8}B S factor. *Physical Review C*, 68:065803, 2003.

[43] R. W. Kavanagh. Proton capture in ^{7}Be. *Nuclear Physics*, 15:411, 1960.

[44] R. W. Kavanagh. 7Be(p,gamma)8B cross section. *Bulletin of the American Physical Society*, 14:1209, 1969.

[45] T. Kikuchi, T. Motobayashi, N. Iwasa, Y. Ando, M. Kurokawa, S. Moriya, H. Murakami, T. Nishio, J. Ruan, S. Shirato, S. Shimoura, T. Uchibori, Y. Yanagisawa, T. Kubo, H. Sakurai, T. Teranishi, Y. Watanabe, M. Ishihara, M. Hirai, T. Nakamura, S. Kubono, M. Gai, R.H. France III, K. I. Hahn, Th. Delbar, P. Lipnik, and C. Michotte. Further measurement of the ^{7}Be(p,γ)^{8}B cross section at low

energies with the Coulomb dissociation of ^{8}B. *European Journal of Physics A*, 3:213, 1998.

[46] Z. Liu, C. Li, S. Wang, J. Zhou, Q. Meng, S. Lu, and S. Zhou. Measurement of change of ^{7}Be decay rate in Be and Au. *Chinese Physical Letters*, 30, 2003.

[47] R. Morlock, R. Kunz, A. Mayer, M. Jaeger, A. Müller, J. W. Hammer, P. Mohr, H. Oberhummer, G. Staudt, and V. Kölle. Halo properties of the first $1/2^{+}$ state in ^{17}F from the ^{16}O(p,γ)^{17}F reaction. *Physical Review Letters*, 79:3837, 1997.

[48] T. Motobayashi, N. Iwasa, Y. Ando, M. Kurokawa, H. Murakami, J. Ruan (Gen), S. Shimoura, S. Shirato, N. Inabe, M. Ishihara, T. Kubo, Y. Watanabe, M. Gai, R. H. France, K. I. Hahn, Z. Zhao, T. Nakamura, T. Teranishi, Y. Futami, K. Furutaka, and Th. Delbar. Coulomb dissociation of ^{8}B and the $^{7}Be(p,\gamma)^{8}B$ reaction at low energies. *Physical Review Letters*, 73(20):2680–2683, Nov 1994.

[49] E. B. Norman, G. A. Rech, E. Browne, R. M. Larimer, M. R. Dragowsky, Y. D. Chan, M. C. P. Isaac, R. J. McDonald, and A. R. Smith. Influence of physical and chemical environments on the decay rates of ^{7}Be and ^{40}K. *Physics Letters B*, 519:15, 2001.

[50] K. Ogata, S. Hashimoto, Y. Iseri, M. Kamimura, and M. Yahiro. Determination of S_{17} from ^{8}B breakup by means of the method of continuum-discretized coupled channels. *Physical Review C (Nuclear Physics)*, 73(2):024605, 2006.

[51] P. D. Parker. ^{7}Be(p,γ)^{8}B Reaction. *Physical Review*, 150:851, 1966.

[52] P. D. Parker. Reanalysis of the ^{7}Be(p,γ)^{8}B Cross-section Data. *The Astrophysical Journal*, 153:L85, 1968.

[53] A. Ray, P. Das, S. K. Saha, and S. K. Das. The effect of host medium on the half-life of ^{7}Be. *Physics Letters B*, 531:187, 2002.

[54] A. Ray, P. Das, S. K. Saha, S. K. Das, B. Sethi, A. Mookerjee, C. Basu Chaudhuri, and G. Pari. Observation of large change of ^{7}Be decay rate in Au and Al_2O_3 and its implications. *Physics Letters B*, 455:69, 1999.

[55] A.E. Schilling, N.F. Mangelson, K.L. Nielson, D.R. Dixon, M.W. Hill, G.L. Jensen, and V.C. Rogers. An accurate measurement of the ^{7}li(d,p)^{8}li excitation function from E_d = 0.6 MeV to 2.0 MeV. *Nuclear Physics A*, 263, 1976.

[56] Karl-Heinz Schmidt. Graf. http://www-wnt.gsi.de/CHARMS/SATAN/graf.htm.

[57] F. Schümann, F. Hammache, S. Typel, F. Uhlig, K. Sümmerer, I. Böttcher, D. Cortina, A. Förster, M. Gai, H. Geissel, U. Greife, N. Iwasa, P. Koczoń, B. Kohlmeyer, R. Kulessa, H. Kumagai, N. Kurz, M. Menzel, T. Motobayashi, H. Oeschler, A. Ozawa, M. Płoskoń, W. Prokopowicz, E. Schwab, P. Senger, F. Strieder, and C. Sturm. Coulomb dissociation of ^8B and the low-energy cross section of the $^7Be(p,\gamma)^8B$ solar fusion reaction. *Physical Review Letters*, 90(23):232501, Jun 2003.

[58] F. Schumann, S. Typel, F. Hammache, K. Summerer, F. Uhlig, I. Bottcher, D. Cortina, A. Forster, M. Gai, H. Geissel, U. Greife, E. Grosse, N. Iwasa, P. Koczon, B. Kohlmeyer, R. Kulessa, H. Kumagai, N. Kurz, M. Menzel, T. Motobayashi, H. Oeschler, A. Ozawa, M. Ploskon, W. Prokopowicz, E. Schwab, P. Senger, F. Strieder, C. Sturm, Zhi-Yu Sun, G. Surowka, A. Wagner, and W. Walus. Low-energy cross section of the $^7Be(p,\gamma)^8B$ solar fusion reaction from the Coulomb dissociation of ^{8}B. *Physical Review C (Nuclear Physics)*, 73(1):015806, 2006.

[59] F. Strieder, L. Gialanella, G. Gyürky, F. Schümann, R. Bonetti, C. Broggini, L. Campajola, P. Vorvisiero, H. Constantini, A. D'Onofrio, A. Formicola, Z. Fülöp, G. Gervino, U. Greife, A. Guglielmetti, C. Gustavino, G. Imbriani, M. Junker, P.G.P. Moroni, A. Ordine, P. Prati, V. Rova, D. Rogalla, C. Rolfs, M. Romano, E. Somorjai, O. Straniero, F. ETerrasi, H.P. Trautvetter, and S. Zavatarelli. Absolute cross section of ^{7}Be(p, γ)^{8}B. *Nuclear Physics A*, 696:219, 2001.

[60] F. Strieder, F. Schümann, L. Gialanella, U. Greife, D. Rogalla, C. Rolfs, H.P. Trautvetter, Zs. Fülöp, G. Gyürky, E. Somorjai, R.W. Kavanagh, L. Campajola, A. D'Onofrio, A. Ordine, V. Roca, M. Romano, F. ETerrasi, C. Arpesella, A. D'Alessandro, C. Gustavino, M. Junker, O. Straniero, P. Corvisiero, M. Dessalvi, P. Prati, S. Zavatarelli, C. broggini, G. Gervino, A. Fubini, E. Bellotti, R. Bonetti, and A. Guglielmetti. Loss of ^{8}Li recoil nuclei in ^{7}Li(d,p)^{8}Li and implications on the ^{7}Be(p,γ)^{8}B cross section. *European Physical Journal A*, 3:1, 1998.

[61] D.R. Tilley, C.M. Cheves, J.H. Kelley, S. Raman, and H.R. Weller. Energy levels of light nuclei, A = 20*. *Nuclear Physics A*, 636:249, 1998.

[62] T. A. Tombrello. The Capture of Protons by ^{7}Be. *Nuclear Physics*, 71:459, 1965.

[63] L. Trache, F. Carstoiu, C. A. Gagliardi, and R. E. Tribble. Asymptotic normalization coefficient of ^8B from breakup reactions and the S_{17} astrophysical factor. *Physical Review Letters*, 87(27):271102, Dec 2001.

[64] F. J. Vaughn, R. A. Chalmers, and L.F. Chase, Jr. Cross Sections for the ^{7}Be(p,γ)^{8}B Reaction. *Physical Review C*, 2:1657, 1970.

[65] L. Weissman, C. Broude, G. Goldring, R. Hadar, M. Hass, F. Schwamm, and M. Shaanan. A new measurement of the ^{7}Li(d,p)^{8}Li cross section and consequences for ^{7}Be(p,γ)^{8}B. *Nuclear Physics A*, 630:678, 1998.

[66] James Ziegler. Transport and ranging of ions in matter. http://www.srim.org.

[67] A. Zyuzin, S.H. Park, L. Buchmann, K.R. Buckley, A.R. Junghans, E.C. Mohrmann, K.A. Snover, T.D. Steiger, and J. Vincent. The fabrication of metallic ^{7}Be targets with a small diameter for ^{7}Be(p,γ)^{8}B measurements. *Nuclear Instruments and Methods in Physics Research B*, 187:264, 2002.

[68] Alexander Y. Zyuzin, Lothar R. Buchmann, John S. Vincent, Ken R. Buckley, Nicholas P. Bateman, K.A. Snover, J.M. Casandjian, T.D. Steiger, E.G. Adelberger, and H.E. Swanson. Metallic beryllium-7 target of small diameter. *Nuclear Instruments and Methods in Physics Research A*, 438:109, 1999.

VITA

Erik Mohrmann was born in Rochester, NY in 1975, son of Richard and Barbara Mohrmann. He attended Greece Athena High School, where he enjoyed academics, music, and varsity athletics.

He earned a B.S. in physics from Rensselaer Polytechnic Institute in 1997. While at RPI he started teaching and developing undergraduate physics courses and knew that he had found his future career. He also participated in various research opportunities and chose experimental nuclear physics as his field of choice.

From there he pursued his education at the University of Washington, earning an M.S. in 1998. He started as physics faculty at the DigiPen Institute of Technology in 2004 and keeps himself busy there as chair of the physics department and president of the faculty senate, among other things. Erik continued his research at the University of Washington under the careful advising of Dr. Kurt Snover, leading to a Ph.D. in 2008.